Cranfield University

Steven Ralph

Prediction of the Onset of
Detectable Multiple Site Damage in a
RAF VC10 Circumferential Butt Joint using Extended
Fatigue Specimen Testing of Retired Fuselage Structure

School of Engineering

MSc Thesis

ProQuest Number: 10820917

ProQuest 10820917

Cranfield University

School of Engineering
Department of Power Propulsion and Aerospace Engineering

MSc Thesis

Academic Year 2003/2004

Steven Ralph

Prediction of the Onset of
Detectable Multiple Site Damage in a
RAF VC10 Circumferential Butt Joint using Extended Fatigue
Specimen Testing of Retired Fuselage Structure

Supervisor: Professor P.Irving

Academic Year 2003 to 2004

This thesis is submitted in partial fulfilment of the
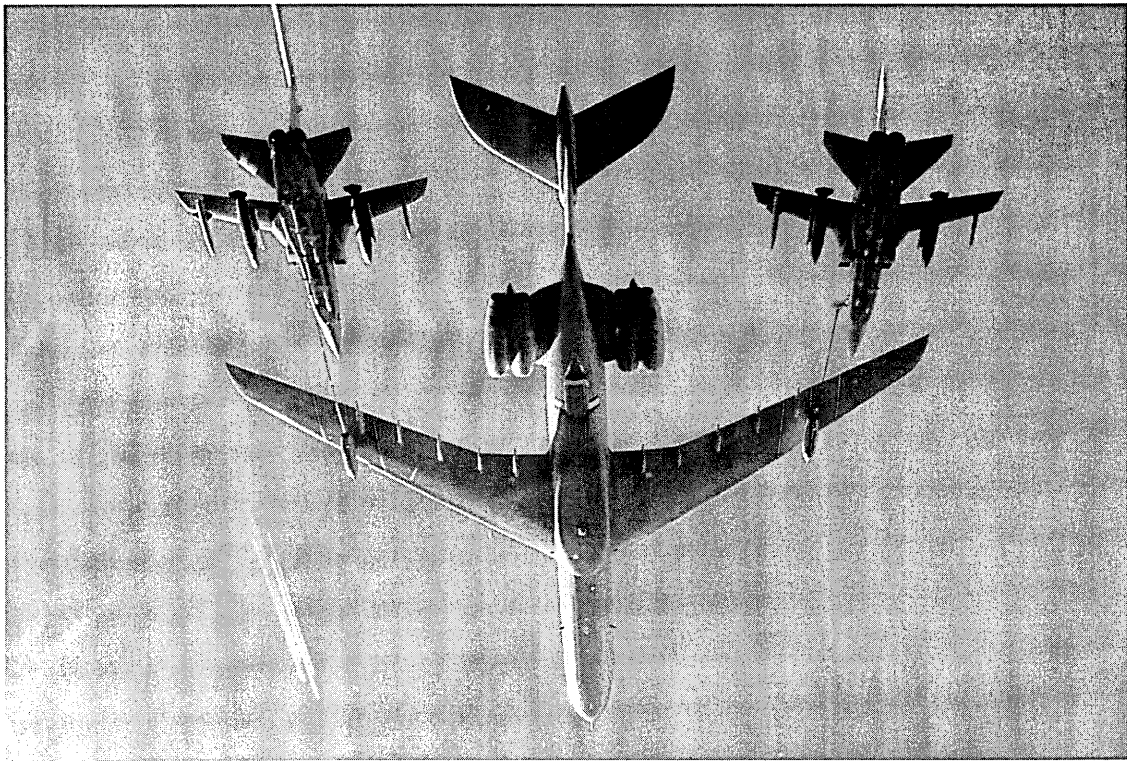requirements for the degree of Master of Science

ABSTRACT

The in-flight pressure fuselage failure of an Aloha Airlines Boeing 737 near Maui, Hawaii on 28 April 1988 brought the issue of Ageing Aircraft and in particular the dramatic destructive potential of Widespread Fatigue Damage (WFD) and Multiple Site Damage (MSD) to the attention of the World. The accident led to a substantial amount of research and development work into the WFD phenomenon and civil regulators mandating WFD assessments of ageing aircraft. Although military aircraft are not regulated by civil requirements, military airworthiness requirements require the completion of Ageing Aircraft Audits (AAA), which do require an evaluation of the potential of WFD.

This Thesis predicts the onset of detectable MSD in a, less researched and highly loaded, circumferential butt joint at the crown of a RAF VC10 aircraft fuselage. The onset of detectable cracking is determined using a theoretical Monte-Carlo probabilistic simulation, which incorporates the results of extended fatigue specimen testing, to failure, of retired RAF VC10 fuselage structure using stresses derived from an in-service stress spectrum of the Joint. A biaxial fatigue analysis of the longitudinal bending and circumferential hoop stresses at the Joint, identifies that the large longitudinal stress from this rear engine large T-tail aircraft are dominant in determining the fatigue endurance of the Joint. Fracture surface analysis, however, identifies that the applied test load is different to the stress state experienced in the fuselage. A possible cause for the discrepancy is identified as secondary bending due to the asymmetry of the butt joint and the unrestricted out-of-plane displacement of the specimens during testing. All the specimens exhibited small (50×10^{-6} m) pre-existing cracks and corrosion pits which, in comparison to 'similar' pristine specimens, suggests (not substantiated) that environmental and operational degradation contributes to reducing airframe joint rivet hole fatigue endurance and standard deviation.

Acknowledgements

RAF VCIO

CONTENTS

FIGURES

TABLES

1 Ageing Aircraft

1.1 Introduction

To try to predict the onset of Multiple Site Damage (MSD) in RAF VC10 aircraft it is first important to understand what type of aircraft are affected by MSD and secondly appreciate how MSD affects airframes and leads to Widespread Fatigue Damage (WFD). Although military aircraft are not regulated by the civil airworthiness requirements, military airworthiness requirements require the completion of Ageing Aircraft Audits (AAA), which do require an evaluation of the potential of WFD.

The in-flight pressure fuselage failure of an Aloha Airlines Boeing 737 near Maui, Hawaii on 28 April 1988 brought the issue of Ageing Aircraft and in particular the dramatic destructive potential of WFD and MSD to the attention of the World. The accident led to a substantial amount of research and development work into the WFD phenomenon. This Chapter briefly looks at the problem of ageing aircraft and the development of civil regulations to combat the WFD phenomenon. It is these regulations and their subsequent Ageing Aircraft Programmes, which are now driving the formulation of similar Military regulations and WFD assessments.

Chapter 2 then describes the WFD phenomenon and how MSD can lead to catastrophic failures. It then identifies areas of the airframe that are susceptible to MSD and briefly describes what is being done to ensure that MSD in these areas does not develop into WFD within the Design Service Goal (DSG) or Out of Service Date (OSD) of the aircraft. These findings are then used to determine the selection of the RAF VC10 FS1045 Circumferential Butt Joint to be evaluated for the onset of MSD. Chapter 3 provides a brief history on RAF VC10 aircraft and full details on the location and construction of the FS1045 Circumferential Butt Joint. The analysis used to predict the onset of MSD in this joint is then provided at Chapter 6 using the test results from an extended fatigue test of a retired RAF VC10 FS1045 butt joint (Chapter 4) and a biaxial fatigue evaluation (Chapter 5).

1.2 Ageing Aircraft

Over the past couple of decades, the commercial aviation industry has experienced a substantial growth in its ageing aircraft fleet due to increasing airlift demands coupled with the high cost of aircraft replacement. A review conducted in 2000, at Reference 1 and Reference 3, detailed the lives of large aircraft in current fleets, which fall into the ageing aircraft category of over 15

years old. The design life anticipated at service entry together with the average lives in the fleet along with the life attained by the fleet leaders of 4 of the more prominent aircraft types are given at Table 1-1.

Aircraft Type	Fleet Total	Number over 15 years old	Design Life (Flights)	Design Life (Hours)	Design Life (Years)
Airbus A300	490	213	36000	60000	20
Fleet Average			15200	27200	13
Fleet Leader			35405	55174	25
Airbus A310	255	74	35000	60000	20
Fleet Average			11600	29800	12
Fleet Leader			25681	58682	17
Boeing 747 (100,200,300)	934	480	20000	60000	20
Fleet Average			10000	46800	14
Fleet Leader			34531	114823	32
Boeing 737 (100,200)	1144	860	75000	51000	20
Fleet Average			42900	46900	22
Fleet Leader			96528	88457	33

Table1-1: Fleet Size & Life of Four Large Civil Airliners (June 2000)

For the majority of the large aircraft types, the fleet average is well under the design life however the fleet leaders are all either approaching or exceeding the original design life specifications. As new aircraft enter service the oldest aircraft are retired and the total size of the ageing fleet remains almost constant. Approximately 13% of Europe's large aircraft are over 15 years old whereas it is nearer to 60% for North America. Although figures are harder to come by, with the high cost of aircraft replacement and increased demands on military budgets, it is suspected that military passenger and transport aircraft are in a similar situation to their commercial counterparts with a high percentage of the fleets being over 15 years old.

Chronological age alone is not an effective measure of aircraft condition. The most important indicator is the number of flights while other factors include flight time, environmental exposure and usage patterns. It is clear, from the above, that a significant percentage of large aircraft are now considered to be ageing

and procedures need to be in place to qualify the structural integrity requirements of such aircraft beyond their original design life. The structural integrity of these aircraft is of concern since factors such as fatigue cracking and corrosion are flight cycle and time dependent.

1.3 Fatigue Requirements

Airframe fatigue is not a new problem in the life of aviation. The awareness of the potential of fatigue in aircraft structure increased during and after World War II. It soon became apparent that static ultimate design without any fatigue analysis was no longer considered to be sufficient for a safe aircraft. From the early 1950's and onwards aircraft structural design included fatigue analysis. Unfortunately, fatigue failures did still occur, due, in part, to an inadequate understanding of the complex fatigue behaviour but also due to the fact that the introduction of pressurised fuselages was making aviation more affordable and therefore increasing aircraft utilization. The most infamous in-service experience of fatigue cracks in the fuselage must be the 2 comet accidents of 1954. The reasons behind the cracks are well documented and important lessons about fatigue were learnt and implemented into future aircraft designs.

However, in accordance with Reference 4, the first formal requirements for fatigue, albeit the fatigue of pressure cabins, were only introduced into British Civil Airworthiness Requirements (BCAR) in July 1956. This was essentially the beginning of the failsafe or damage tolerant approach being given as a preferred option to declaring a safe fatigue life. Prior to this requirement the aircraft manufactures would agree a fatigue life with the Air Regulation Board, the predecessor of the Civil Aviation Authority – Safety Regulation Group. A similar approach to the fatigue of pressure cabins was extended to the rest of the aircraft structure in March 1959 and formed the basis of certification for fatigue and damage tolerance in the UK until the Joint Airworthiness Requirements (JAR) were created in Europe in 1974. Here both fatigue substantiation and failsafe were required along with consideration of tolerance of damage until detected. This requirement ran in parallel with the BCAR code as a certification option until July 1979 when the UK adopted the JAR code solely.

1.4 Ageing Aircraft Programmes

Throughout the 1970's there was a significant increase in the number of registered aircraft, Reference 1, and by the late 1970's there were growing numbers of aircraft in service for longer than their original design lives. The original design life provided a general indication of the period for which the aircraft might usefully and safely remain in service. In the late 1970's it became clear that the operational life of fail safe aircraft could be greater than that originally set at certification. This in turn raised questions about the continuing capability of the fail safe and damage tolerance concepts together with the inspection procedures to detect any growing cracks or other forms of damage.

These concerns were, unfortunately, realised in 1976 and 1977 with the in flight structural failure of 2 large aircraft. The 1976 accident was due to the failure of the wing caused by the interaction of cracks in the lower wing skin that had not been detected on previous inspections. Whereas the 1977 accident, was due to the separation of the tail plane attributable to the fail-safe design being unable to arrest the formation of a crack from pre-existing fatigue. These accidents emphasised the growing concerns of the fail-safe design philosophy and inspection procedures in place at that time. The aircraft regulators, manufacturers and operators had to act to the growing problem of ageing aircraft and in the late 1970's the first major steps in improving airframe long-term structural integrity was taken with the creation and implementation of Supplementary Structural Inspection Programmes (SSIP).

Fail-safe design requirements gave way to the damage tolerance approach. Damage tolerance requires that the structure be capable of sustaining small cracks without failure, and an inspection programme be implemented to detect such cracks before they grow to a critical length. Such an approach recognises the impossibility of establishing complete structural redundancy, the premise of the fail-safe philosophy, and places greater emphasis on inspection. The SSIP provided a means for aircraft maintenance and inspection procedures to meet damage tolerance criteria. It required the evaluation of structures using fracture mechanics analysis to develop supplemental structural inspections. Through the SSIP fail-safe designed aircraft were brought into conformance with the damage tolerance approach by means of an updated inspection programme

Developing SSIPs or conducting a structural audit, as it is known in the UK, is a demanding task involving a manufacturer in many thousands of personnel hours of work. In some cases, substantial analytical work has been supported by test programmes and or teardown inspections of high time aircraft retired from service. In accordance with Reference 5, SSIPs have been developed for all of the aircraft listed at Table 1-2. The analysis work involved, and the detailed inspection requirements derived from a structural audit, can vary considerably from each aircraft type. It can be relatively simple, with few modifications and inspections for all aircraft in the fleet when a life extension of only a few hours is concerned. It may be very complex indeed, with an analysis task involving risk assessment, state of the art fracture mechanics, and taking account of the world fleet age distribution, the reliability of inspection and different inspection methods. The typical number of damage sites that need to be investigated varies with the aircraft, depending on stress levels and detail design features, but is frequently in excess of a hundred. For the majority, of the aircraft types listed at Table 1-2, the SSIPs has proved to be an effective tool in allowing aircraft to continue to operate into old age and yet maintain an adequate safety level.

Aircraft Type
Airbus A300
Boeing 707, 727, 737, 747
Lockheed L1011
McDonnell Douglas DC-8, DC-9, DC-10
Fokker F27
BAC 1-11
Avro 748

Table 1-2: Some Aircraft with Supplemental Structural Inspection Programmes (SSIP)

Due to the accidents detailed above along with the implementation of the SSIP, there was an increased public awareness of ageing aircraft issues. The situation was exacerbated slightly throughout the 1980's predominantly due to the success of the SSIPs, reaching the public's attention, detecting cracks before they became catastrophic. The in flight pressure fuselage failure however, of an Aloha Airlines 737 near Maui, Hawaii on 28 April 1988 brought this awareness into the forefront with the dramatic pictures, similar to Figure 1-1, of the successful landing of the damaged aircraft. The most probable cause of the accident was a link up of multi-site-damage (MSD) in the fuselage a more detailed explanation of which is given at Chapter 2. The accident, however, emphasised that even the SSIPs could not be guaranteed to reveal all age and fatigue related damage, which was capable of causing in flight catastrophic failure.
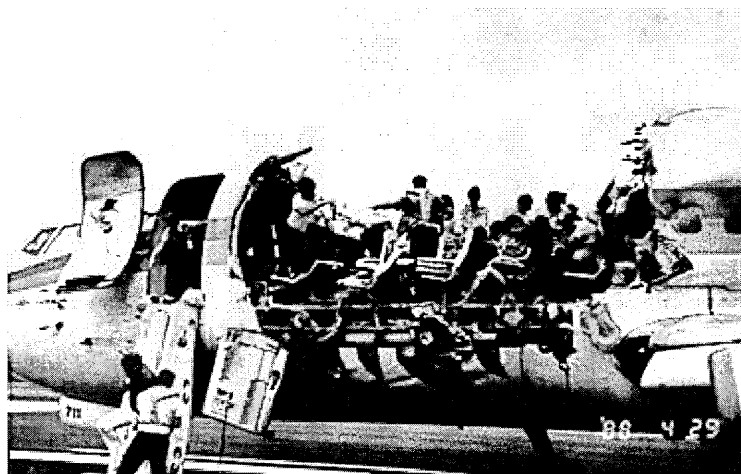
Figure 1-1: Flight 243 - Aloha Airlines 737 Accident 1988

5

The Aloha accident prompted considerable aviation community activity related to aging airframes as the SSIPs were seen to be wanting. Regulators, manufactures and operators got together to initiate changes to the system for safety improvement. A number of industry committees were formed and the first became known as Airworthiness Assurance Task Force (AATF). This later became known as the Airworthiness Assurance Working Group (AAWG) under the umbrella of the Aviation Regulatory Advisory Committee (ARAC). In Europe the JAA has set up a European version of this group, the European Ageing Aircraft Working Group (EAAWG), to adapt the various recommendations into the European regulatory framework. These Groups effectively have 2 main roles:

      a.   To oversee the incorporation and implementation of ageing aircraft programme on the various fleets and.

      b.   Respond to specific regulatory tasking.

The work of the Groups has focused on the following major issues:

      a.   Structural Service Bulletins with terminating action.

      b.   Corrosion Control Programmes.

      c.   Review of SSIPs.

      d.   Maintenance Programme Design.

      e.   Repair Assessment and Documentation.

      f.   Research and Development.

      g.   Widespread Fatigue Damage.

To date a significant amount of work has been conducted in each of the above activities however, the outstanding and long-standing concern is for the potential development and possible non-detection of multiple site and multi element damage in the fleet that could lead to Widespread Fatigue Damage (WFD). The definition and major issues relating to WFD are detailed at Chapter 2.

The AAWG developed airworthiness rules and supporting advisory material to address the issue of WFD. It also detailed a procedure to follow to continue operation of aircraft beyond their Design Service Goal (DSG). Typically, the DSG is a number of flight cycles or hours commensurate with a reasonable service period at a high utilisation rate. Consequently it varies for each aircraft type and will need to be clearly defined as a precursor to the evaluation

assessment of the airworthiness rule. The evaluation assessment to combat WFD in existing aircraft covers the following aspects:

a. Expected locations of WFD.

b. Aircraft age at which WFD is expected.

c. The criteria used to predict WFD.

d. Modification and/or inspection action that will prevent WFD.

e. Limits of the evaluation.

Since the Aloha accident there has been some extensive research into WFD, which has lead to the AAWG publishing technical recommendations on rulemaking, Reference 3, to prevent WFD in the commercial fleet. As a result of the AAWG recommendations, the FAA plans to issue a Notice of Proposed Rulemaking requiring operators to develop a plan and eventually a structured maintenance programme to preclude WFD in their fleets for baseline and repaired, altered or modified structure. Civil operators and manufacturers, with aging aircraft, have completed a considerable amount of research into WFD and have developed methods of predicting the onset of MSD to ensure the airworthiness of the their aircraft to the point of WFD as detailed at Chapter 2.

2 Widespread Fatigue Damage (WFD)

2.1 Introduction

As detailed at Chapter 1, the continued structural integrity and damage tolerance of ageing aircraft is of great concern to the aerospace community. The main issue now threatening aging airframe residual strength has been defined in terms of a Widespread Fatigue Damage (WFD) phenomenon. In accordance with Reference 3 the definition of WFD is as follows:

> *Widespread Fatigue Damage (WFD) in a structure is characterised by the simultaneous presence of cracks at multiple structural details that are of sufficient size and density whereby the structure will no longer meet its damage tolerance requirements.*

In order to fully appreciate the above definition and to ensure that there is no ambiguity it is important to define precisely what is meant by damage tolerance. Reference 3 provides the following definition:

> *Damage Tolerance is the attribute of the structure that permits it to retain its required residual strength without detrimental structural deformation for a period of use after the structure has sustained specific levels of fatigue, corrosion, accidental damage or discrete source damage.*

The 2 sources of WFD are Multiple Site Damage (MSD) and Multiple Element Damage (MED) and Reference 3 defines them both as follows:

> *Multiple Site Damage (MSD) is a source of WFD characterised by the simultaneous presence of fatigue cracks in the same structural element (i.e. fatigue cracks that may coalesce with or without other damage leading to a loss of the required residual strength).*

> *Multiple Element Damage (MED) is a source of WFD characterised by the simultaneous presence of fatigue cracks in similar adjacent structural elements.*

As implied by the above definition of damage tolerance, aircraft structures are designed to be crack free for a specific design life goal. Structural integrity is assured within this life through the implementation of an inspection programme derived from a damage tolerance evaluation. This evaluation is based on the growth of a single lead crack in each Principle Structural Element (PSE), which may occur within the design life goal as a consequence of initial manufacturing damage or in service accidental damage. As explained at Chapter 1, today's economic environment is dictating that transport aircraft remain in service

beyond their initial design life goals. This creates the potential for WFD, which can, along with undetected corrosion, have a drastic affect on lead crack residual strength.

2.2   Effect of Widespread Fatigue Damage

As mentioned at Chapter 1, the in flight pressure fuselage failure of an Aloha Airlines 737 near Maui, Hawaii on 28 April 1988 brought the issue of ageing aircraft and in particular the dramatic destructive potential of WFD and MSD to the attention of the World. In accordance with Reference 8, the potential for the formation of MSD in lap splice joints of Boeing 737 aircraft was known before the accident. An Airworthiness Directive (AD), detailing the problem and mandating inspections and rectification action as required, had been released in November 1987. The requirements of the AD had been conducted on the Aloha 737 and MSD was found and repaired in accordance with the AD but, unfortunately, the MSD responsible for the catastrophic failure had not been detected.

2.2.1 Probable Cause of Aloha 737 Accident

Aloha Flight 243 had departed Hilo Airport en route to Honolulu, Hawaii as part of a normal scheduled flight with a total of 95 passengers and crew on board. As the aircraft levelled at 24,000ft the upper part of a section of the fuselage came away from the remainder of the aircraft. Miraculously, the aircraft landed safely with only the loss of one person, a stewardess who had unfortunately not been seated at the time of the catastrophic failure of the fuselage.
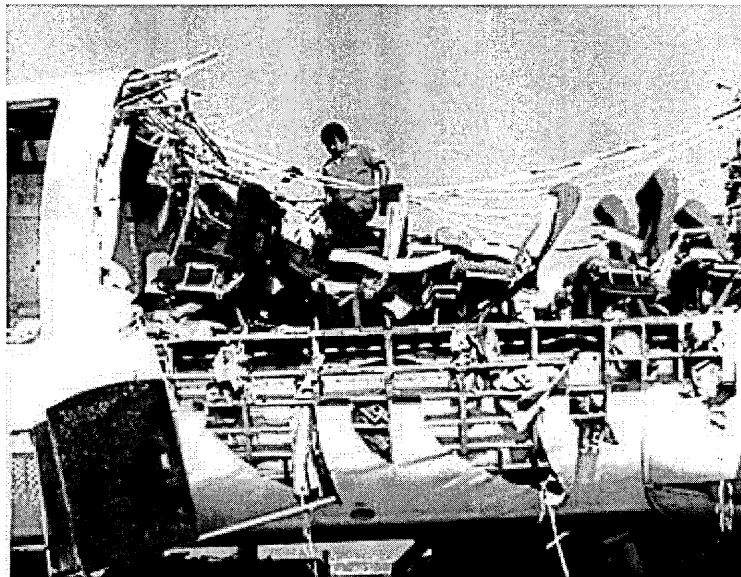
Figure 2-1: Aloha Boeing 737 Accident

The most probable cause of the accident was linked up MSD in the fuselage skin at the upper row of countersunk rivets of the lap splice joint at stringer 10

9

on the left hand side of the aircraft. The rivets had been installed in knifed edged countersink holes, which have a notoriously poor fatigue life. The skin panels had, however, been bonded together at the joint using a cold cure adhesive. The purpose of the adhesive in the design of the joint was to reduce the bearing load on the rivets. Unfortunately, the joint began to delaminate due to corrosion of the metal in the faying surface of the joint and the rivets then had to react the hoop tension loads due to cabin differential pressure. This accelerated the onset of MSD and the cracks eventually linked up into a critical crack leading the catastrophic failure of the fuselage as illustrated at Figure 2-2.

FUSELAGE SKIN SPLICE

- COLD CURED ADHESIVE DELAMINATED DUE TO CORROSION
- KNIFE EDGED RIVETS STARTED TAKING LOAD
- SUBSEQUENT MSD LINKED UP

MSD

DELAMINATED ADHESIVE

KNIFE EDGE REDUCES FATIGUE LIFE
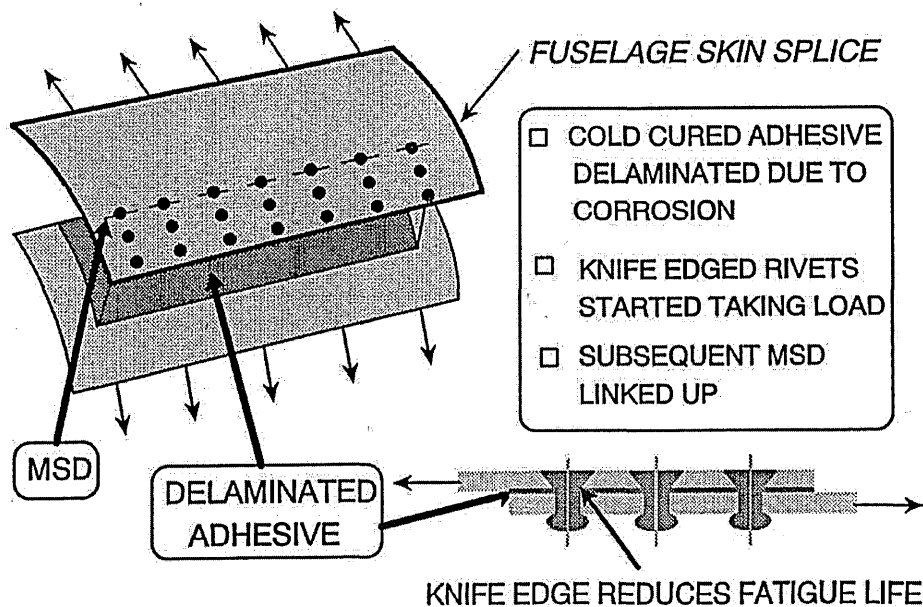
Figure 2-2: Probable Cause of Aloha 737 Accident (Reference 8)

As mentioned at Chapter 1, the accident led to the formation of the Airworthiness Assurance Working Group (AAWG) and the European Ageing Aircraft Working Group (EAAWG) and a substantial amount of research and development work into the WFD phenomenon. Early research concentrated on obtaining information on crack propagation by fatigue testing specimens containing a variety of MSD cracking scenarios. The intention was then to use this information to establish inspection programmes but it soon became apparent that even extremely small MSD has the potential to drastically reduce the residual strength capability of the originally certified aircraft. Consequently, as detailed at Reference 8, the Airworthiness Authorities will not allow MSD to be tolerated within the operational life of the aircraft if it will cause the originally certified residual strength capability to degrade below the design limit load.

2.2.2 Residual Strength Capability

The continued operation of aircraft beyond their service life goal exposes the airframe to the formation of WFD. The effect of MSD, in comparison to local damage single crack growth, is illustrated in Figure 2-3. The presence of MSD adjacent to a lead crack in a typical airframe detail drastically reduces the residual strength of the detail. The drop of the residual strength from the capability of the intact structure to the capability required to withstand the design loads occurs in a much shorter time compared with that of the single crack. This factor together with the reduced critical crack length ($a_{crit\,LD}$ in comparison to $a_{crit\,WFD}$) results in a significantly reduced crack growth period between the detectable and critical situation (L_{LD} in comparison to L_{WFD}).
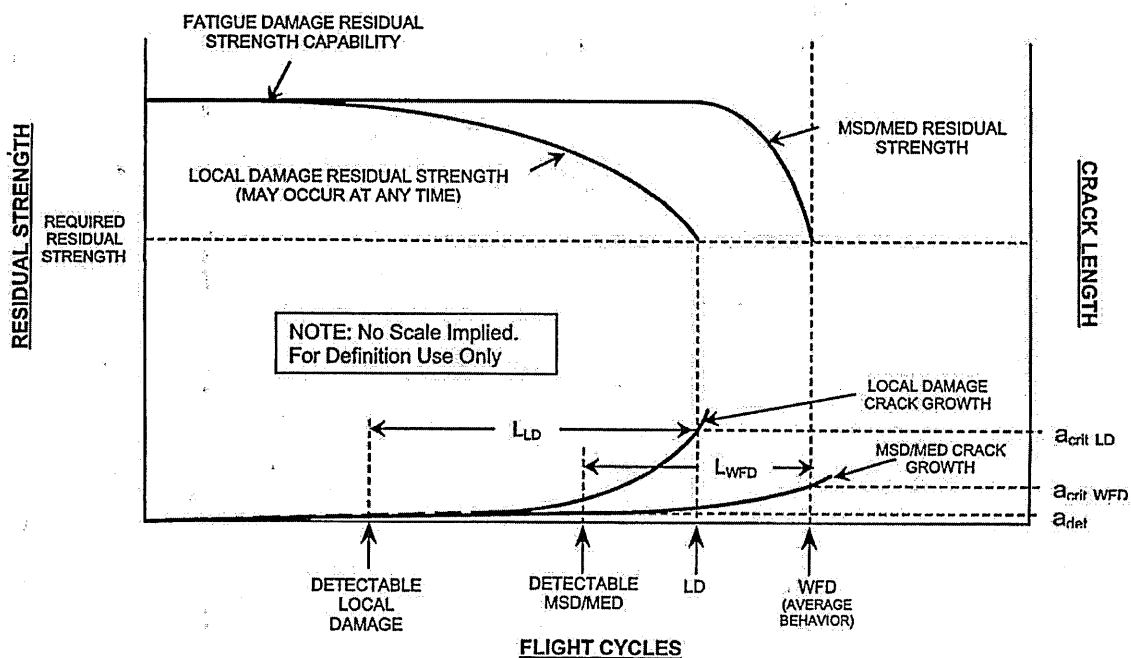
Figure 2-3: Difference Between Local Damage Behaviour and MSD/MED Behaviour for a Typical Detail (Reference 3)

For structure where the MSD/MED situation is reliably detectable before it becomes critical a monitoring period may be defined and applied before other means have to be taken, as illustrated at Figure 2-4. The monitoring period is the period of time when special inspections of the fleet are initiated due to the increased risk of MSD/MED and ending when the point of WFD is reached. The point of WFD is derived from the average expected behaviour. Beyond this point the aircraft may not be operated without further evaluation. The point of WFD is established so that operation up to that point provides the equivalent protection to that of a 2-lifetime fatigue test. Repeat inspection intervals are established based on the length of time from detectable fatigue cracks to the average WFD divided by a factor. Several opportunities must be provided to detect cracking between fatigue initiation and the Point of WFD (I_{WFD}).

11
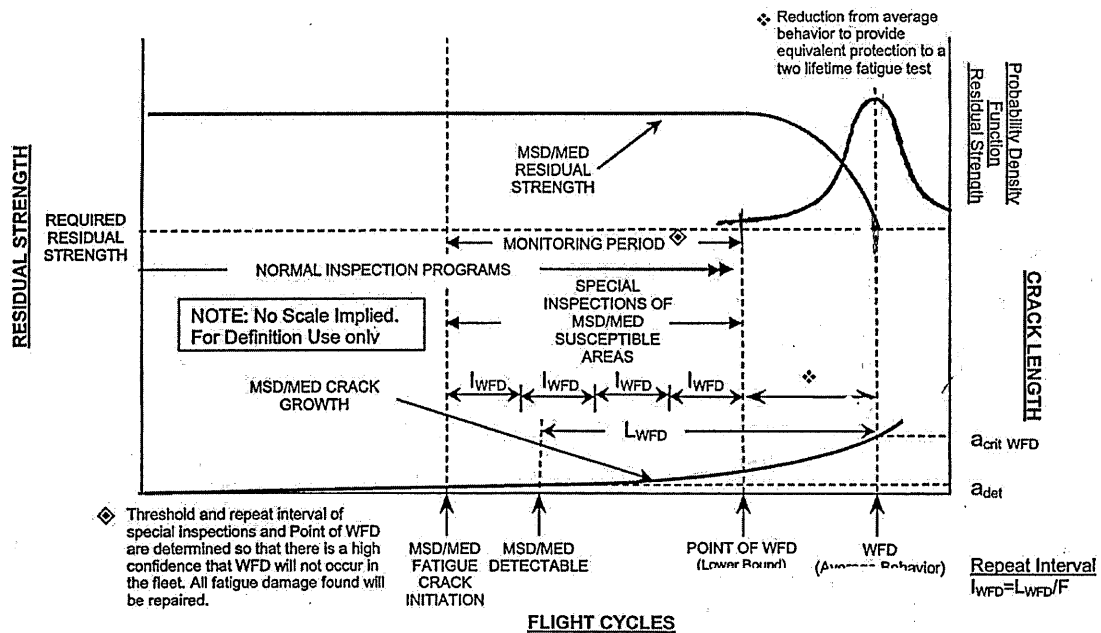
Figure 2-4: Determining the Monitoring Period (Reference 3)

For situations where it is not possible to reliably detect MSD/MED before it becomes critical, as detailed at Figure 2-5, the aircraft may not be operated beyond the point of WFD without significant modification or part replacement.
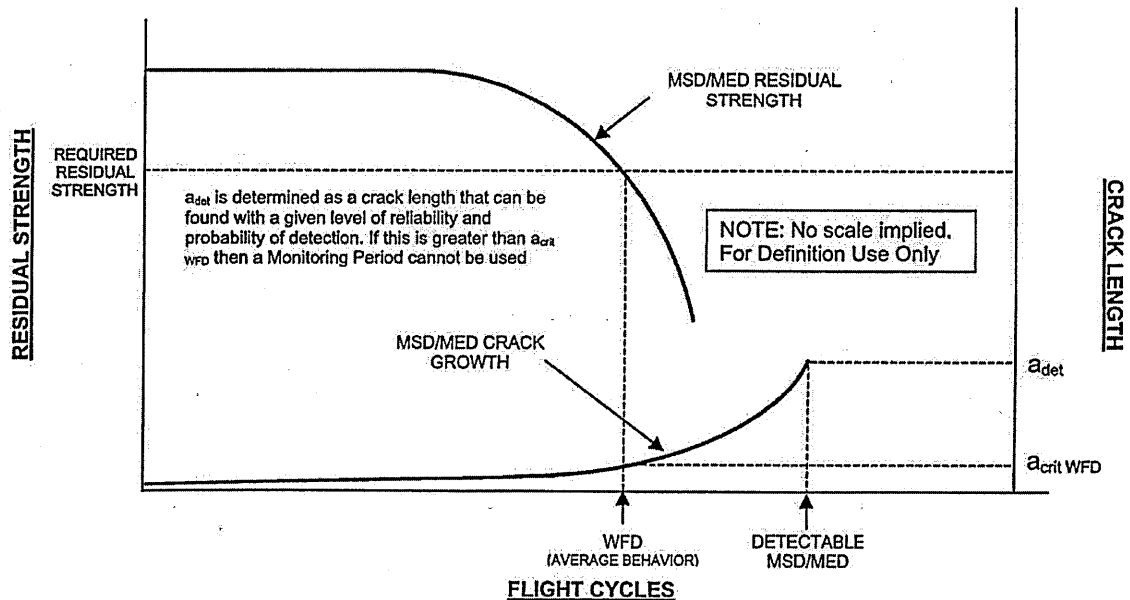
Figure 2-5: Condition Where Monitoring Period Cannot Be Used (Reference 3)

2.2.3 Lead Crack Link-up Criterion

A considerable amount of research, as detailed below, has been conducted to determine how MSD causes the residual strength of the structure to decrease as detailed above. For ductile alloys, such as those used in airframe construction, Reference 2 explains this phenomenon by assuming that the link-up of the lead crack with the MSD crack will occur when the intact ligament stress between the 2 crack tips reaches the typical yield strength of the material. This leads to the intuitive link-up criterion illustrated at Figure 2-6. As the loads increase the plastic zones R1 and R2 will increase until they touch. Reference 2 then postulates that the link-up of the 2 cracks will occur when the 2 plastic zones touch. This approach is not considered analytically perfect but appears to be accurate enough to be able to make some judgements of the effect of MSD on lead crack residual strength.

CRITERION FOR LINK-UP
WHEN PLASTIC ZONES
FROM LEAD CRACK AND
MSD CRACK TOUCH

$$R_1 + R_2 = [P\text{-}d/2\text{-}a_1]$$
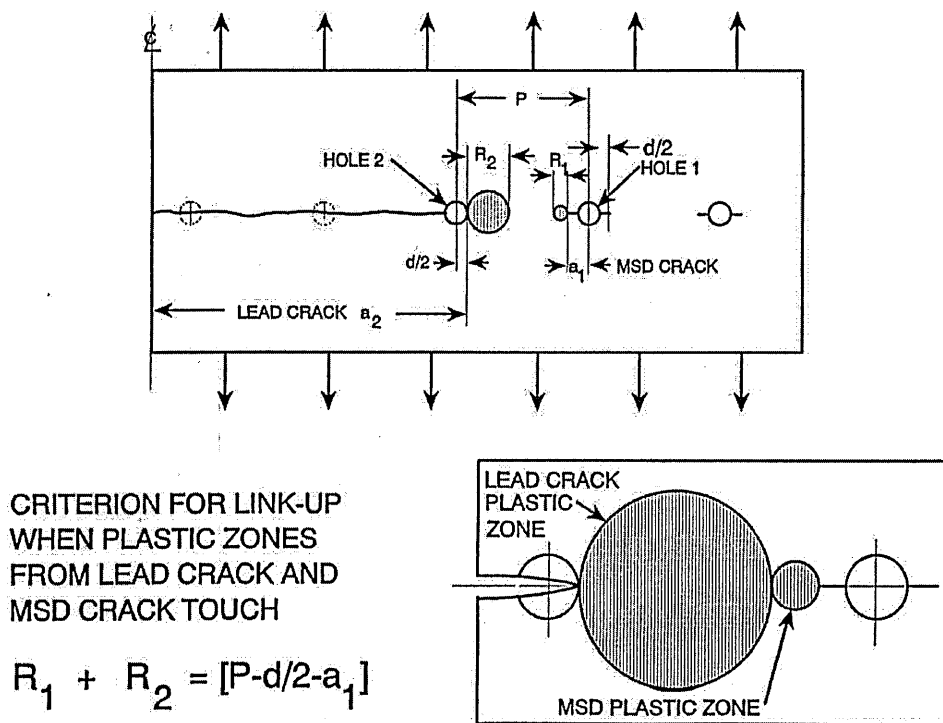
Figure 2-6: MSD & Lead Crack Link-up Criterion (Reference 2)

The above criterion can be used to give an appreciation of how many MSD cracks it takes to substantially reduce the residual strength of the lead crack. In the case shown at Figure 2-7, a single 0.05" (1.27mm) MSD crack either side of a Lead Crack) line ABEF would be the residual strength curve for a single lead crack based on linear elastic fracture mechanics. In this example the MSD crack is located 8 inches (203mm) from the centre of the lead crack and line HBJC is developed based on the above criterion at Figure 2-7. If a lead crack with a larger half-length existed at point J and the gross stress increased to

σ_{EX} then the lead crack and the MSD crack would link up to a new lead crack half-length of K. The residual strength of the new crack is, however, at point E and the load would need to be increased to point E before failure. This means that the residual strength for any lead crack of half-length greater than E would automatically be reduced to point E in the presence of a single MSD crack.
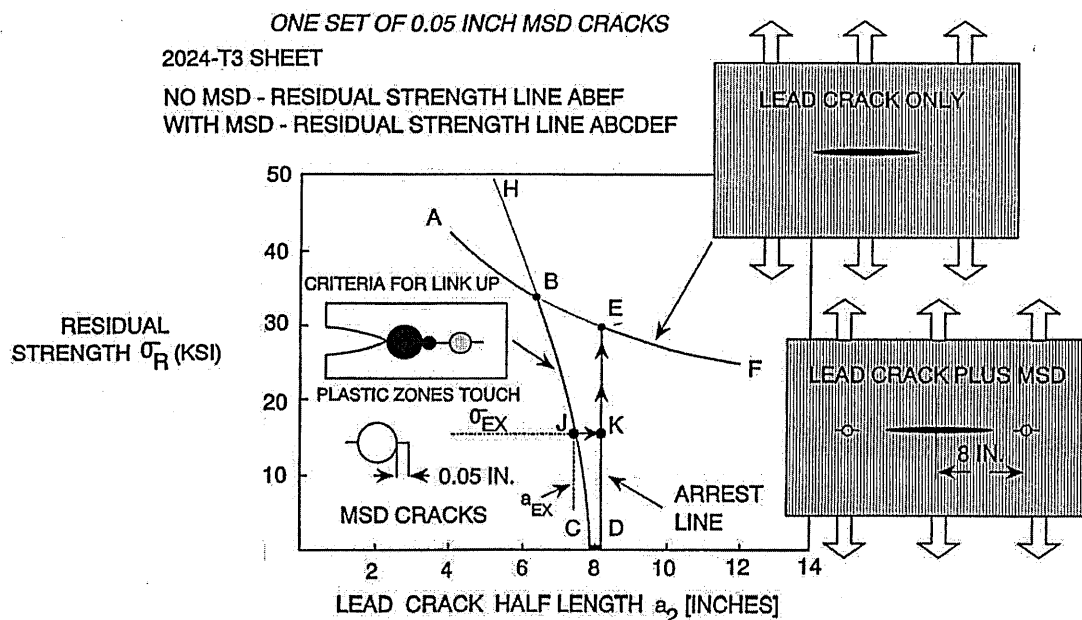
Figure 2-7: Effect of MSD on Lead Crack Residual Strength (single MSD crack either side of lead crack) (Reference 2)

Reference 2 then explains that if a second MSD crack is included there will be 2 link up lines as illustrated at Figure 2-8. Line LBJC for the first link-up and line MED for the second link –up. It can be seen again that the link-up between the lead crack and the first MSD crack would occur at a stress of σ_{EX}. Based on this hypothesis the panel would still be stable and load could be increased to point E on line MED and at this point link-up between the new lead crack and the second MSD crack would occur. The new lead crack length would now be F and load could be increased up to point G before failure would occur. It can therefore be seen that the residual strength of a lead crack of half-length greater than B would automatically be reduced to G in the presence of 2 MSD cracks.

NO MSD - RESIDUAL STRENGTH LINE ABGH

WITH MSD - RESIDUAL STRENGTH LINE ABCDEFGH

2024-T3 SHEET
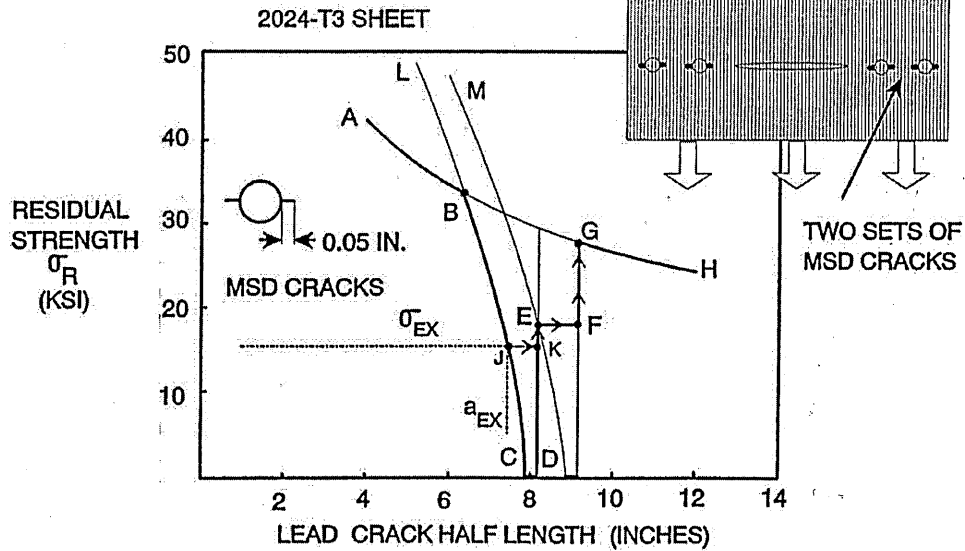
**Figure 2-8: Effect of MSD on Lead Crack Residual Strength
(two MSD cracks either side of lead crack)
(Reference 2)**

If the process in continued by adding MSD cracks, Reference 2 hypothesis that after 4 or 5 MSD cracks the residual strength does not recover after link-up of the first crack. Figure 2-9 illustrates the case for 5 MSD cracks ahead of the lead crack. It can be seem that the residual strength for any lead crack half-length beyond point B will be reduced to point E.
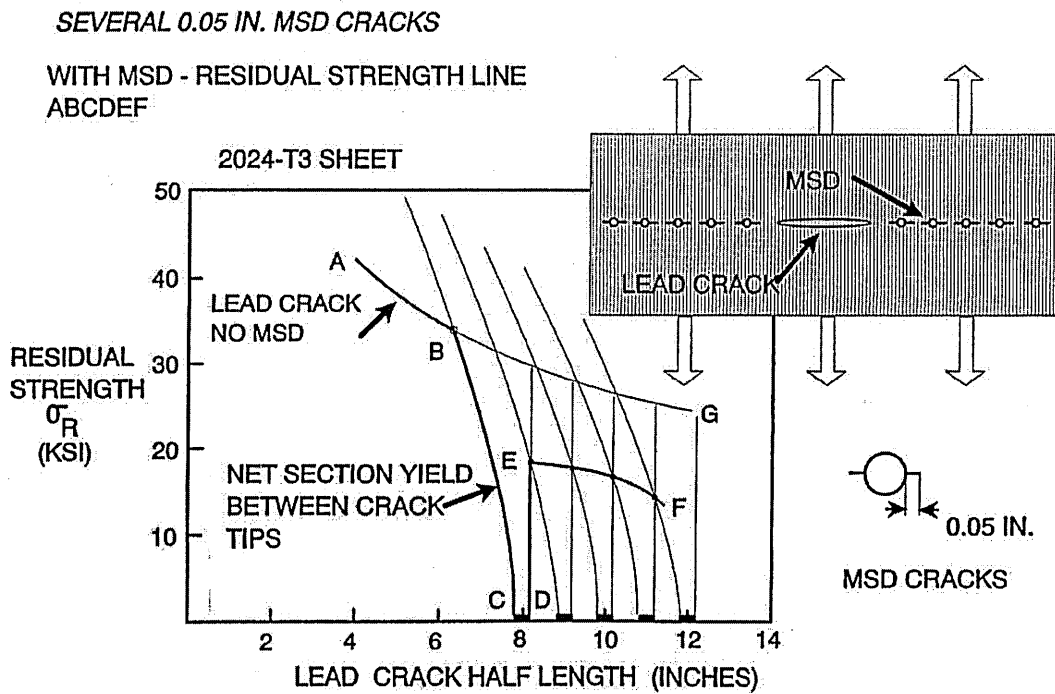
**Figure 2-9: Effect of MSD on Lead Crack Residual Strength
(several MSD cracks either side of lead crack)
(Reference 2)**

2.3 Areas Susceptible to MSD/MED

In accordance with Reference 3, Susceptible Structure is defined as that structure which has the potential to develop MSD/MED. Susceptible areas are characterised by similar structural details operating at uniform stress levels and by the fact that its structural capability could be significantly degraded by the presence of multiple cracks.

Since the formation of the AAWG and the increased awareness of the WFD phenomenon there has been significant increase in the exchange of technical data. Consequently, the AAWG (Reference 3) has been able to compile a list of the major sections of aircraft structure, and construction typical to those areas, which industry experience has shown to be susceptible to MSD/MED. The diagrams shown, Figure 2-10 to 2-25, are typical MSD/MED sites and do not show all types of construction or structural detail, which would be characteristic of a particular aircraft model. The diagrams shown cover the following major sites and identify where each site is more prone to MSD or MED or both, they also identify some of the service or test experience factors that influence MSD/MED at each particular site:

- Longitudinal Skin Joints, Frames and Tear Strips (MSD/MED).

- Circumferential Joints and Stringers (MSD/MED).

- Lap Joints with Milled, Chem-milled or Bonded Radius (MSD).

- Fuselage Frames (MED).

- Stringer to Frame Attachment (MED).

- Shear Clip End Fasteners on Shear Tied Fuselage Frames (MSD/MED).

- Aft Pressure Dome Outer Ring and Dome Web Splices (MSD/MED).

- Skin Splice at Aft Pressure Bulkhead (MSD).

- Abrupt Changes in Web or Skin Thickness Pressurised or Un-pressurised Structure (MSD/MED).

- Window Surround Structure (MSD/MED).

- Over Wing Fuselage Attachments (MED).

- Latches and Hinges of Non-plug Doors (MSD/MED).

- Skin at Run-out of Large Doubler on Fuselage, Wing or Empennage (MSD).

- Wing or Empennage Chordwise Splices (MSD/MED).

- Rib to Skin attachments (MSD/MED).

- Typical Wing and Empennage Construction (MSD/MED).
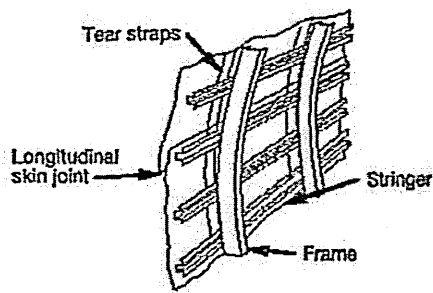
Type and possible location of MSD and MED
• MSD longitudinal skin joint
  • Lap joint
    - Outer skin upper rivet row
    - Inner skin lower rivet row
  • Butt joint
    - Skin outer rivet rows
    - Doubler inner rivet rows
  • Lap joint with radius
    - In radius
• MED—frame
  • Stress concentration areas
• MED—tear straps
  • Critical fastener rows in the skin at tear strap joint
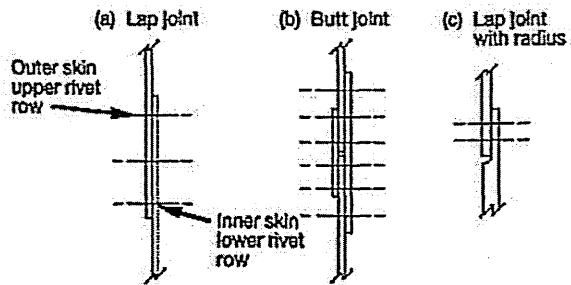
Service or test experience of factors that influence MSD and MED (examples)
• High stress—misuse of data from coupon test
• Corrosion
• Disbond
• Manufacturing defect
  • Surface preparation
  • Bond laminate too thin
  • Countersink, fastener fit
• Design defect—surface preparation process

Figure 2-10: Longitudinal Skin Joints, Frames and Tear Strips (MSD/MED) (Reference 3)
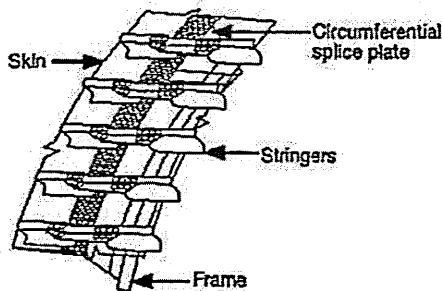
Type and possible location of MSD/MED
• MSD—circumferential joint
  • Without outer doubler
    - Splice plate—between and/or at the inner two rivet rows
    - Skin—forward and aft rivet row of splice plate
    - Skin—at first fastener of stringer coupling
  • With outer doubler
    - Skin—outer rivet rows
    - Splice plate/outer doubler—inner rivet rows
• MED—stringer/stringer couplings
    - Stringer—at first fastener of stringer coupling
    - Stringer coupling—in splice plate area
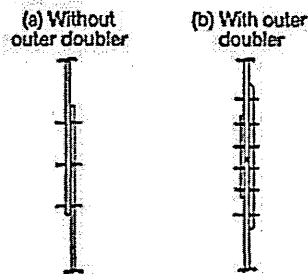
Service or test experience of factors that influence MSD and/or MED (examples)
• High secondary bending
• High stress level in splice plate and joining stringers (misuse of data from coupon test)
• Poor design (wrong material)
• Underdesign (over-estimation of interference fit fasteners)

Figure 2-11: Circumferential Joints and Stringers (MSD/MED) (Reference 3)

18

Outer skin at milled
or chem-milled step

Cracking

Bonded doubler

Bonded joint
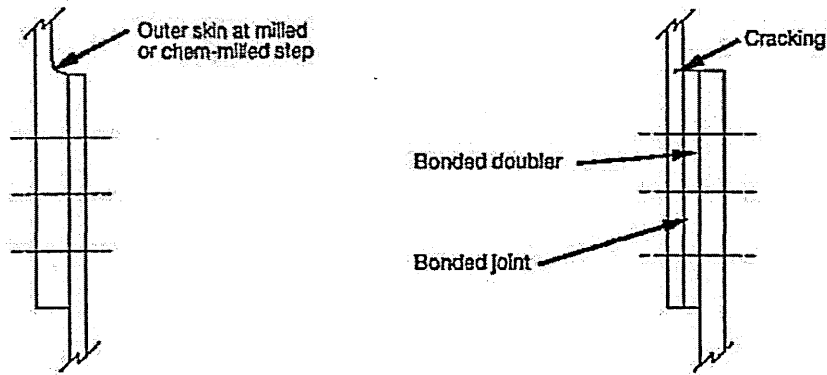
Type and possible location of MSD and MED

- MSD—abrupt cross section change
- Milled radius
- Chem-milled radius
- Bonded doubler runout

Service or test experience of factors that
influence MSD and MED (examples)

- High bending stresses due to
  eccentricity

**Figure 2-12: Lap Joints with Milled, Chem-milled or Bonded Radius (MSD)
(Reference 3)**

Fuselage
skin panel

Stringer

Frame

Typical fuselage
skin panel

Stringer

Skin

Frame

Tear strap

Typical cracking
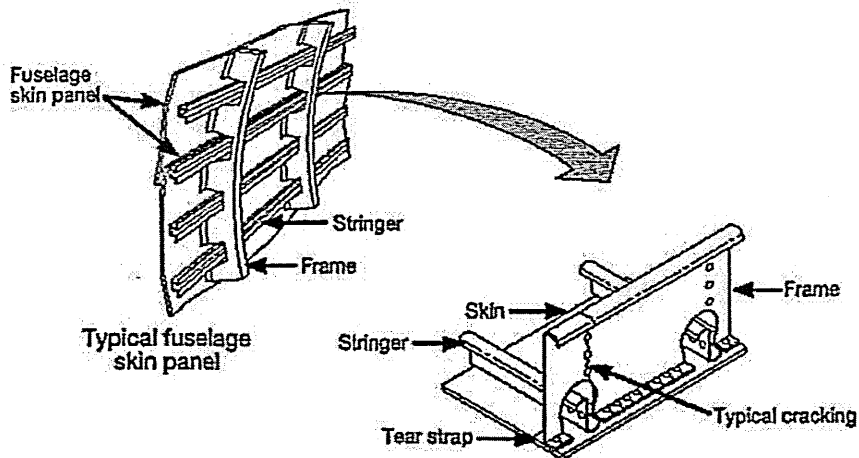
Type and possible location of MSD/MED

- MED—the cracking of frames at stringer cutouts
  at successive longitudinal locations in the
  fuselage. The primary concern is for those areas
  where noncircular frames exist in the fuselage
  structure. Fractures in those areas would result
  in panel instability.

Service or test experience of factors that influence
MSD and/or MED (examples)

- High bending—noncircular frames
- Local stress concentrations
  - Cutouts
  - Shear attachments

Figure 2-13: Fuselage Frames (MED) (Reference 3)

19
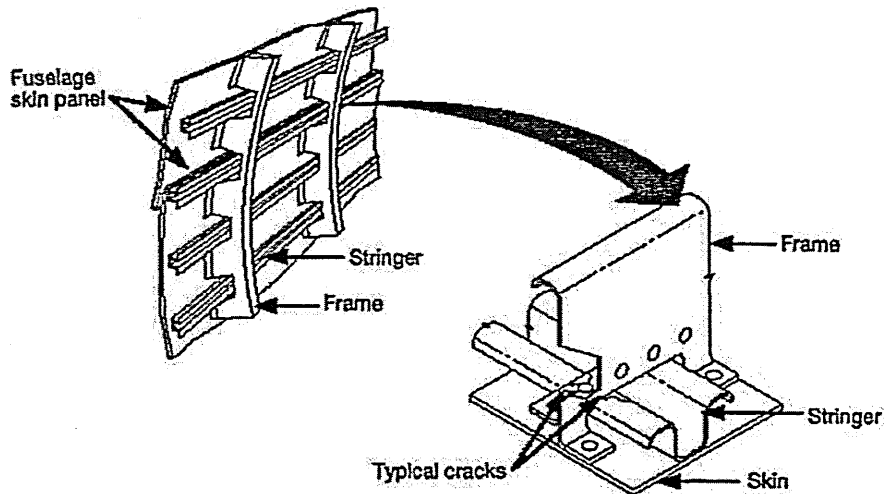
Type and possible location of MED

* MED—any combination of fracture of frames, clips, or stringers, including the attachments, resulting in the loss of the shear tie between the frame and stringer. This condition may occur at either circumferential or longitudinal locations at fuselage frame/stringer intersection.

Service or test experience of factors that influence MSD and/or MED (examples)

* Poor load path connection

Figure 2-14: Stringer to Frame Attachment (MED) (Reference 3)
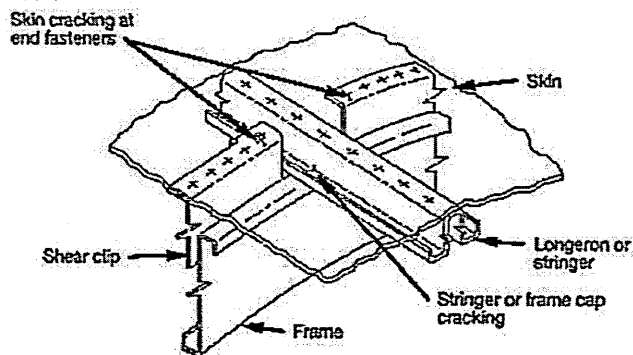
Type and possible location of MSD and MED

* MSD—skin at end fastener of shear clip
* MED—cracking in stringer or longeron at frame attachment
* MED—cracking in frame at stringer or longeron attachment

Service or test experience of factors that influence MSD and MED (examples)

* Preload
* Localized bending due to pressure
* Discontinuous load path

Figure 2-15: Shear Clip End Fasteners on Shear Tied Fuselage Frames (MSD/MED) (Reference 3)

Outer ring splice

Web splices

Typical outer ring splices

F fastener
R radius

Legend:
F fastener
R radius

Type and possible location of MSD/MED
- MSD/MED—outer ring splice
  - Attachment profiles—at fastener rows and/or in radius area
- MED—web splices
  - Bulkhead skin and/or splice plates—at critical fastener rows

Service or test experience of factors that influence MSD and/or MED (examples)
- Corrosion
- High stresses—combined tension and compression
- High induced bending in radius
- Inadequate finish in radius—surface roughness

Figure 2-16: Aft Pressure Dome Outer Ring and Dome Web Splices (MSD/MED) (Reference 3)

Pressurized skin

Unpressurized skin

Skin cracking

"T" frame

Bulkhead web

Type and possible location of MSD and MED
- MSD—skin at end fastener holes

Service or test experience of factors that influence MSD and MED (examples)
- Shell discontinuous induced bending stresses
- High load transfer at fastener
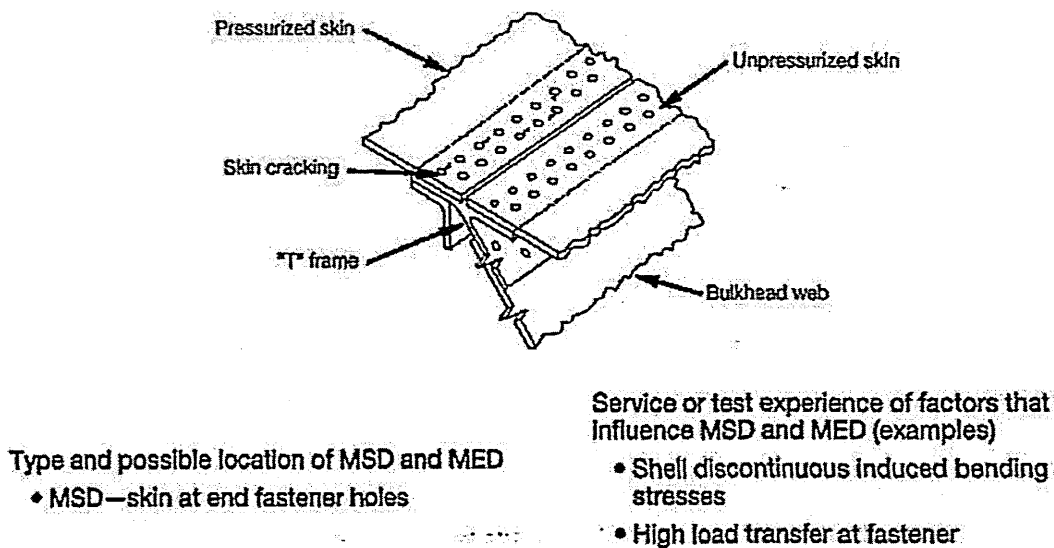
Figure 2-17: Skin Splice at Aft Pressure Bulkhead (MSD) (Reference 3)

21
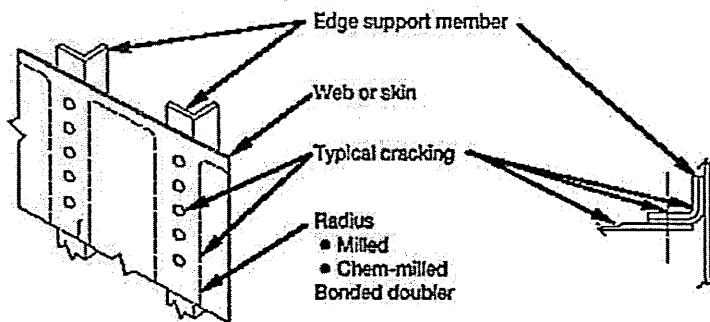
Type and possible location of MSD and MED

Abrupt change in stiffness*
  • Milled radius
  • Chem-milled radius
  • Bonded doubler
  • Fastener row at edge support members
Edge member support structure
  • Edge member – in radius areas

Service or test experience of factors that influence MSD and MED

Pressure structure
  • High bending stresses at edge support due to pressure
Non-pressure structure
  • Structural deflections cause high stresses at edge supports

* Often multiple origins along edge member

Figure 2-18: Abrupt Changes in Web or Skin Thickness Pressurised or Un-pressurised Structure (MSD/MED) (Reference 3)
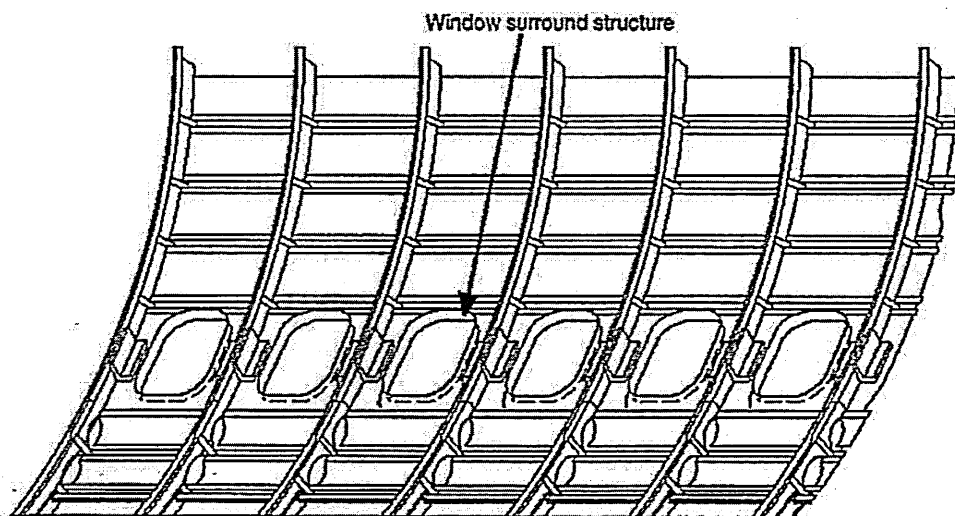
Type and possible location of MSD/MED
  • MSD—skin at attachment to window surround structure
  • MED—repeated details in reinforcement of window cutouts or in window corners

Service or test experience of factors that Influence MSD and/or MED (examples)
  • High load transfer

Figure 2-19: Window Surround Structure (MSD/MED) (Reference 3)

Upper wing surface

Typical fuselage attachments
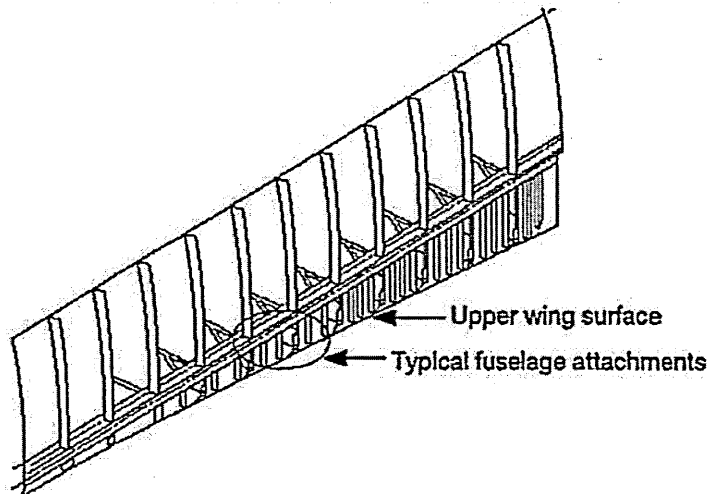
Type and possible location of MSD/MED	Service or test experience of factors that influence MSD and/or MED (examples)
• MED—repeated details in overwing fuselage attachments	• Manufacturing defect—prestress • Induced deflections

Figure 2-20: Over Wing Fuselage Attachments (MED) (Reference 3)

Door

A

B

Hinge lobe

Hinge pin

View A

Latch hook

Lubrication passage

Attach bolts

View B

Type and possible location of MSD/MED	Service or test experience of factors that influence MSD and/or MED (examples)
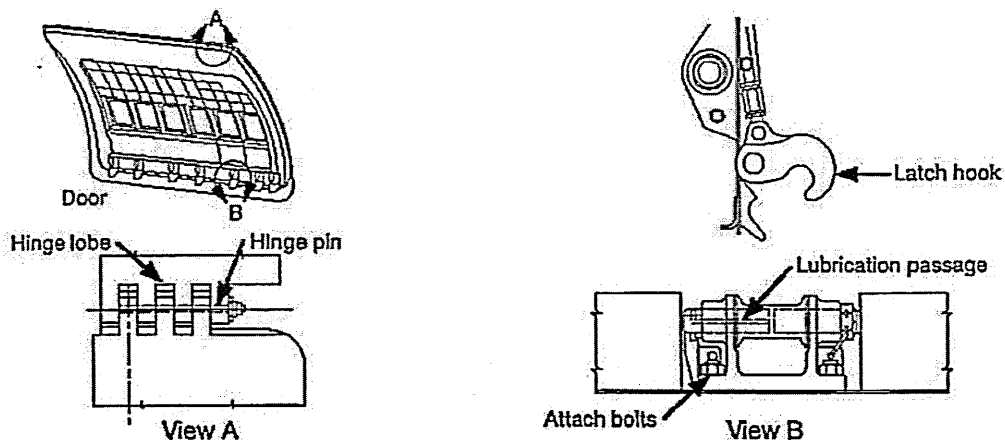
• MSD—plano hinge
  • At hinge fastener attachment row
  • In fillet radius
  • Emanating from hole in lobes
• MED—latches
  • In multiple latch hooks
  • At lube channel of latch spool
  • At spool bracket attach bolts (also corrosion)
	• Bending stresses due to fuselage elongation
	• High local stress
	• Fretting

**Figure 2-21: Latches and Hinges of Non-plug Doors (MSD/MED)
(Reference 3)**

23
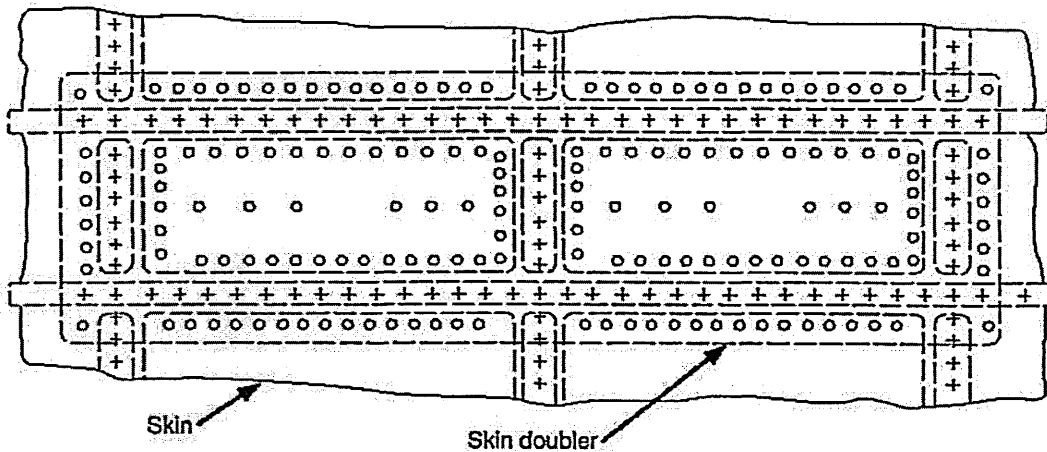
Skin

Skin doubler

Type and possible location of MSD/MED
• MSD—cracks initiated at multiple critical
fastener holes in skin at runout of doubler

Service or test experience of factors that influence
MSD and/or MED (examples)
• High load transfer—high local stress

Figure 2-22: Skin at Run-out of Large Doubler on Fuselage, Wing or Empennage (MSD) (Reference 3)

Front spar

Typical skin and stringer splice

Rib

Fitting

Skin panel

Splice plate

Stringer

Chordwise joints
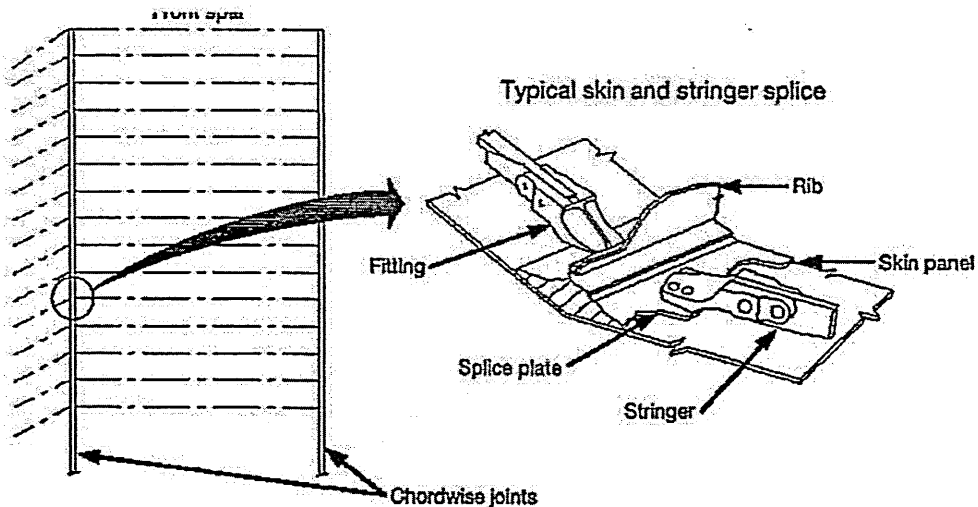
Type and possible location of MSD/MED
• MSD—skin and/or splice plate
   • Chordwise critical fastener rows
• MED—stringer runout of fitting
   • Fatigue-critical fastener holes at stringer and/or fitting

Service or test experience of factors that influence
MSD and/or MED (examples)
• High load transfer
• Local bending

Figure 2-23: Wing or Empennage Chordwise Splices (MSD/MED) (Reference 3)

24
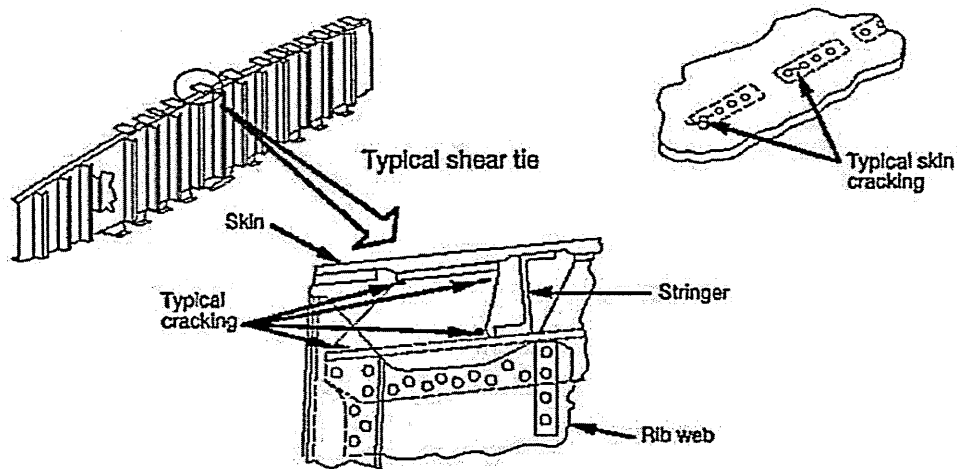
Type and possible location of MSD and MED
- MSD—critical fasteners in skin along rib attachments
- MED—critical rib feet in multiple stringer bays (particularly for empennage under sonic fatigue)

Service or test experience of factors that influence MSD and MED (examples)
- Manufacturing defect—prestress due to assembly sequence
- Sonic fatigue (empennage)

Figure 2-24: Rib to Skin attachments (MSD/MED) (Reference 3)

Riveted Skin and Stringer Construction (MSD & MED)

Integrally Stiffened Skins (MSD)

Inherent fail safe and crack stopper characteristics
- MSD—chordwise cracks link up at
  a) Rib attachment holes
- MED—
  b) Drain or vent holes
  c) Stiffener run-outs at root rib or tank end rib

Do not have inherent crack stopper characteristics of riveted skin and stringer construction
- MSD—Chordwise cracks link up at
  d) Rib attachment holes
  e) Drain or vent holes
  f) Stringer run-outs at root rib or tank end rib
- MED—becomes MSD

Figure 2-25: Typical Wing and Empennage Construction (MSD/MED) (Reference 3)

25

2.4   Research and Development

As a result of worldwide aging aircraft activities, research programmes were initiated in the United States and in Europe. As defined at Reference 3, the research goals covered 5 main areas as follows:

  a.   Initiation of MSD/MED.

  b.   Propagation of MSD/MED

  c.   Residual Strength.

  d.   Risk Analysis.

  e.   Discrete Source.

To date a considerable amount of research has been conducted in all of the above aspects of the WFD phenomenon. The majority of the research work into the initiation of MSD has concentrated on the coupon testing, at first, predominantly using pristine material and joints that simulated the susceptible structure on the airframe. As mentioned above, the presence of MSD adjacent to a lead crack has a significant influence on the residual strength capability of the structure. Former concepts for residual strength evaluation used for type certification only considered single damages. These concepts are not adequate for the residual strength evaluation in the presence of MSD. The research work onto the propagation of MSD/MED and residual strength has therefore demanded the development of more sophisticated approaches, as detailed at Reference 2 and 3, such as:

  a.   Crack Tip Opening Angle (CTOA).

  b.   Elastic/Plastic Energy Method or T* Integral.

  c.   Plastic Zone Link-up.

  d.   J Integral.

  e.   Elastic-plastic FE analysis.

To support these new approaches significant testing with flat and curved panels has been conducted to demonstrate the residual strength capability of aircraft structure potentially susceptible to WFD and to verify concepts, methods and analysis tools for residual strength evaluation. Additionally, probabilistic methodologies can predict the time-dependent probability of the point of WFD, the time dependent distribution of the aircraft's residual strength, and the impact of inspections on the structural integrity of the aircraft. These theoretical models cover the following areas:

a.   Multiple Fatigue Crack Initiation (Probabilistic Analysis).

b.   Multiple Fatigue Crack Growth (Deterministic Analysis).

c.   Residual Strength in the presence of MSD/MED (Deterministic Analysis)

d.   Risk Assessment and Overall MSD/MED Models.

These probabilistic effects can be derived from parameters which influence the development of MSD and WFD and which they themselves show a probabilistic character. The major parameters are the initial design of a structural part, the loading, the manufacturing process and the material properties. These properties obviously have a great influence on the fatigue life (MSD behaviour) of a structure. Any approach to assess MSD, therefore, has to consider the probabilistic effect of these parameters. For the majority of the models the probabilistic effect is done be means of a Monte-Carlo simulation (a method of automatically analysing the effect of randomly varying inputs on the outputs of the modelled system). The model consists of 2 parts, a probabilistic and a deterministic part. Within the probabilistic algorithm the initial damage scenario is determined, while the subsequent steps, such as damage accumulation, crack growth and residual strength are calculated in a deterministic approach. Such a model is used to determine the initial damage scenario of the susceptible structure considered in this Thesis and therefore more details about the theoretical model can be found at Chapter 6. Reference 3 does, however, give an excellent summary of the models used by Airbus Industrie, Boeing Commercial Airplanes, Lockheed Martin Aeronautical Systems and Delta Air Lines.

Initially, after the Aloha 737 Accident, the majority of the research concentrated on fuselage joints and such research was vindicated as service experience (Reference 3) has shown that this is one of most MSD susceptible areas. Testing predominantly took the form of generic coupons, rather than specific aircraft components, such as simple specimens, to determine the initiation and growth of MSD, and complex specimens, to determine the residual strength of representative stiffened panels. Several manufacturers, as detailed above, use a stochastic approach based on the Monte-Carlo simulation procedure to determine damage scenarios, which are the basis for the WFD evaluation. A series of initial damage scenarios are randomly defined taking material scatter onto account. Generally the material scatter of the number of cycles to failure of the generic specimens, mentioned above, is used. The research now proposed by the AAWG changes the focus to investigating the variability of MSD cracking for typical high loaded fuselage joints with high secondary bending. Constant amplitude tests with small and large coupons are proposed, to determine the scatter up to the first 0.005-inch (0.127mm) flaw and up to failure to compare results with data from in-service aircraft.

Currently a considerable amount of the type of research proposed by the AAWG is being conducted at the Full-Scale Aircraft Structural Test Evaluation and Research Facility (FASTER) at the Federal Aviation Administration William J Hughes Technical Centre as detailed at References 19, 20 and 21. This unique facility hosts a test fixture that is capable of applying to full-scale curved panels a combination of loads, including internal pressurisation, tensile hoop, longitudinal, and frame loads, and shear skin loads, that simulates real flight loading conditions encountered by an aircraft fuselage. Results of the research conducted at this facility will identify any shortcomings or additional issues that had not been identified with generic research that does not precisely simulate real aircraft structure design and loading conditions. Despite being unable to duplicate the impressive capabilities of the FASTER facility, this Thesis also attempts to investigate some of the AAWG proposals by trying to predict the onset of MSD in a, less researched, circumferential butt joint at the crown of an aircraft fuselage, using a theoretical model similar to that used by Airbus Industrie but incorporating the results of extended fatigue specimen testing of retired fuselage structure.

3 Royal Air Force VC10

3.1 Introduction

The Vickers VC10 entered commercial service in 1962 and has been in Service with the Royal Air Force, as a multi-role air refuelling tanker and transport aircraft, since 1966. The design of the VC10 commenced at BAe Weybridge in the early 1950's and was intended to meet a requirement for BOAC, the forerunner to British Airways, for a medium to long range passenger aircraft to fly the flagship BOAC routes. Powered by 4 Rolls-Royce Conway engines and carrying a maximum of 130 passengers, it had a range of 3800nm.
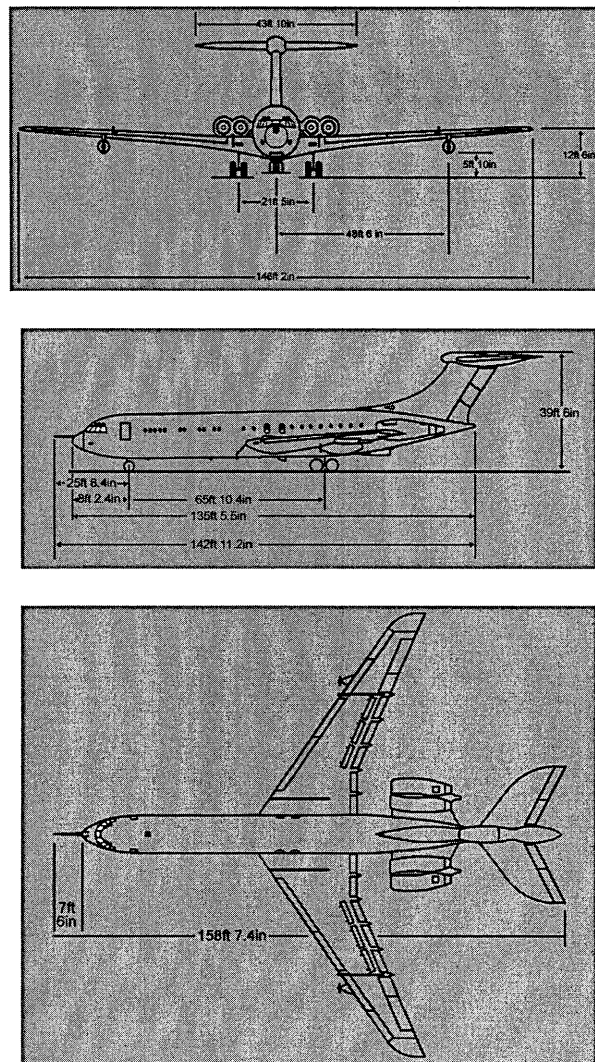
Figure 3-1: RAF VC10 Dimensions

The VC10 was produced in 2 main versions, namely the Standard and the Super-VC10 variants, which featured an increased wingspan and greater passenger capacity. The design was one of the first British attempts at a Fail-Safe (FS) design, although Vickers conducted a number of fatigue tests aimed at guaranteeing an initial crack-free life.
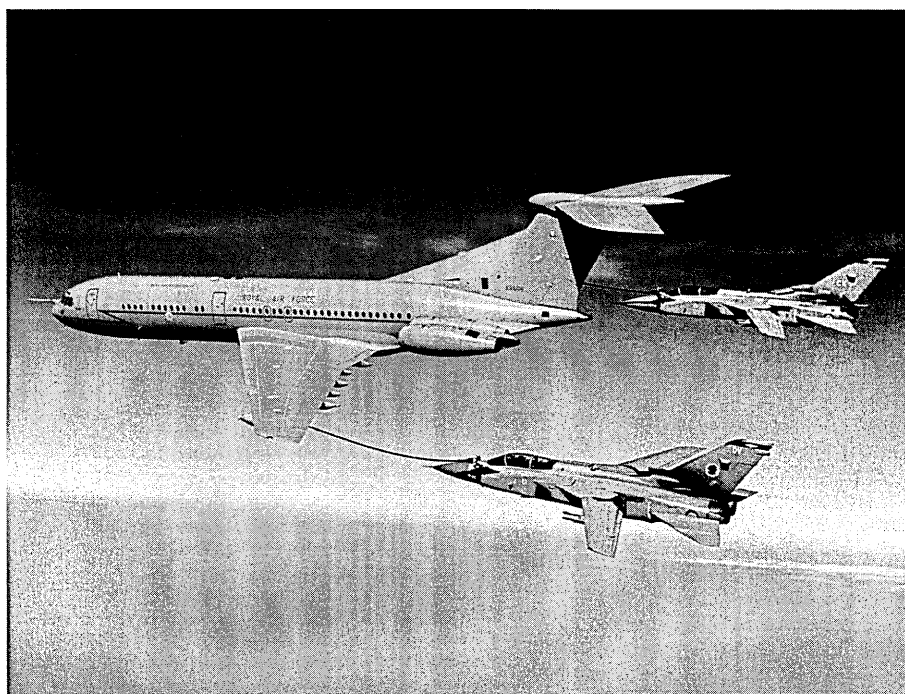
Figure 3-2: RAF VC10 Multi-Role Air Refuelling Tanker and Transport Aircraft

The VC10 CMk1 entered RAF service in 1966 as a passenger, freight and air ambulance aircraft, and was a hybrid version of the commercial variants in that it comprised of a standard fuselage, albeit including a large freight door, mounted on a Super VC10 wing. A total of 14 C Mk1 aircraft were ordered and all had been delivered to the RAF by August 1968. The first of the tanker variants, VC10 KMk2, (tanker conversions of 5 Ex-BA/Gulf Air, Standard VC10 airliners) were delivered in 1983 followed by the first VC10 KMk3 (tanker conversions of 4 Ex-East African Airways Super VC10 airliners) in 1985. The first of the VC10 KMk4 (tanker conversions of 5 Ex-BA Super VC10 airliners) were delivered to the RAF in April 1994. The oldest of these aircraft had in excess of 45 000 flying hours and 16 000 flight cycles at the time of conversion. Thirteen of the C Mk1 aircraft were converted to C Mk1K standard between Feb 91 and Feb 97 increasing their capability to the Air Refuelling role. All VC10 tanker variants have 2 wing pod and one centreline hose drum units to transfer fuel to receiver aircraft.

Following the introduction of an early retirement programme and other operational requirements the current RAF VC10 active fleet now consists of 11 CMk1K, 4 KMk3 and 4 KMk4 aircraft. The current disposition of the Fleet is shown in Figure 3-3. To date, 5 of these retired aircraft have been subjected, in

accordance with RAF policy, to a deep structural examination or teardown destructive programme by QinetiQ, Farnborough. The aim of the Programme is to verify not only the condition of known trouble areas within the structure but to take the opportunity to examine areas that would not normally be open during normal maintenance procedures. A VC10 KMk2 has recently completed such a teardown examination from which sections of the fuselage where removed to provide extended fatigue test specimens for this Thesis. The remainder of the VC10 fleet is expected, based on latest plans and options, to remain in service until phase out between 2008 and 2013. After which the Future Strategic Tanker Aircraft (FSTA) should, as is currently the intention, replace it.

RAF VC10 FLEET DISPOSITION
(June 2004)
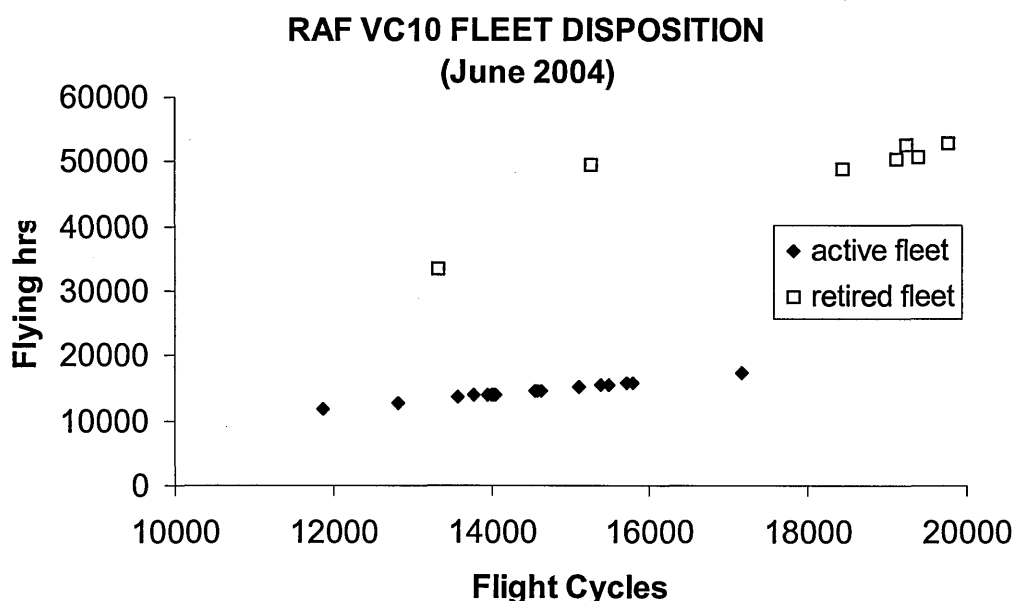
Figure 3-3: RAF VC10 Fleet Disposition (June 2004)

3.2 Design Philosophy

The VC10 was designed under a 'fail safe' philosophy with no defined upper life limits. As mentioned above, however, a number of fatigue tests aimed at guaranteeing an initial crack-free life had been conducted. These tests were based upon a theoretically derived load spectrum for a typical BOAC standard VC10 operating a 3-hour flight plan at an average take-off weight of 250 000lb (113 398Kg). RAF VC10 aircraft however, operate at an average TOW in the range of 260 000 to 290 000lb (117 934 – 131542Kg), have a super VC10 wing with a 6 ft (1.83m) greater wingspan and operate completely different sortie profiles to normal civil airliners as detailed below. These details together with the fact that, as was common practice in the 1950s, the same airframe had been used for both the static and fatigue tests, with the subsequent crack retardation effects, made it highly likely that the predictions of the fatigue test would not be applicable to RAF VC10 aircraft. The first signs of such

discrepancies were identified in 1987 when a 15" (38cm) crack was discovered in a VC10 KMk2 wing centre-member spar-web.

A review of the testing concluded that the aircraft had no valid fatigue life clearance and, given that the fail-safe philosophy was no longer considered adequate, it was decided to adopt damage tolerance (DT) as the basis for continuing structural integrity assurance. In the short-term, during the transition to DT, inspection intervals were assessed to account for the higher RAF operating weights and the Structural Sampling Programme (SSP) was refined to include a much greater level of directed inspections. The long-term activity centred on the production of a Fatigue Type Record (FTR) for the VC10, based on the outcome of a fatigue and damage tolerance evaluation using the results from an extensive Finite Element Model. The evaluation finally identified some 257 Structural Significant Items (SSIs), which lead to 660 primary damage calculation sites across the VC10 variants. This would represent an enormous increase in the scheduled maintenance requirements of the VC10 and it soon became apparent that it would prove impracticable to complete all the inspections before the first aircraft retired from Service. It was therefore decided that 140 SSIs covering components, which had not been compromised by the inadequacies of the original fatigue test programme, would have their inspection threshold recalculated. The other areas of the airframe were re-assessed as Principal Structural Elements (PSEs) and Structural Control Points (SCPs) to create approximately 100 SCP- driven directed inspections.

This decision ensured that the VC10 entered a pseudo-damage tolerant regime whilst at the same time ensuring that the RAF have an aircraft they can fly to meet its full operational requirements. Reliance of this approach is however being placed upon complimentary programmes such as Ageing Aircraft Audits (AAA) and teardown inspections of key structural features on retired airframes. Although military aircraft are not regulated by the civil requirements detailed at Chapter 1, military airworthiness requirements do stipulate the completion of AAAs, which include an evaluation of the potential of WFD. A VC10 AAA was completed by BAe in April 1992 and follow on action from the Audit included maximising the opportunities afforded by the teardown programme to address ageing aircraft issues, such as widespread fatigue damage, the interaction of corrosion and fatigue, and the long-term effects of repairs.

3.3 Sortie Profile Codes

As mentioned above, RAF VC10 aircraft are operated in a different manner to how they were originally designed to be used in the civil airliner role. Typical flight cycles of RAF aircraft are divided into Sortie Profile Codes for ease of identification and monitoring of individual aircraft utilisation. The SPCs applicable to all marks of the VC10 can be categorised into 4 main groups:

    a.   Crew Training.

    b.   Route Flying.

c. Air Refuelling Operations.

d. Miscellaneous.

The most commonly utilised SPC for the tanker variants is the standard towline air-refuelling (AR) sortie as detailed below:
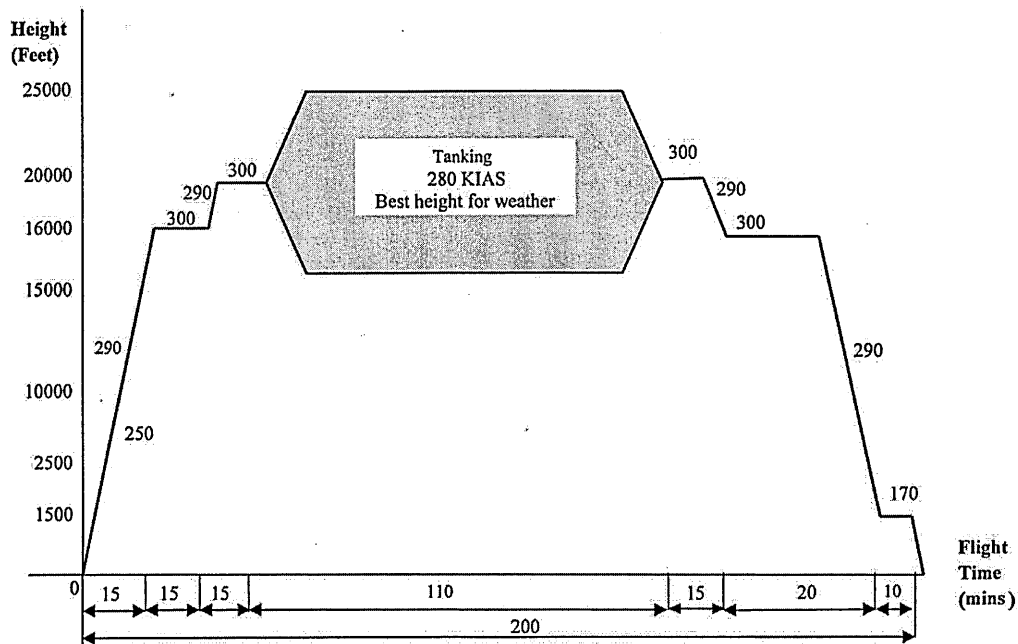
Figure 3-4: RAF VC10 Standard Towline Air Refuelling Sortie

Normal cruise is carried out at 300 Knots Indicated Air Speed (KIAS) at or below 31000ft (9449m) and M 0.82 above 31000ft (9449m). AR usually takes place between 10000ft (3048m) and 30000ft (9144m) depending upon operational restrictions, receiver performance or weather. AR elements of a tanking sortie take place in a racetrack pattern, with straights approximately 30 miles long. The aircraft is turned using 20-30 degrees angle of bank, spending approximately 30% of the time in the turn. Approximately 80% of the tanking is flown with the wing hoses deployed and 20% using the centreline hose. Equipment failures may result in AR being conducted with only one wing hose deployed. On conclusion of AR, the aircraft may be climbed to a more economical level for further transit.

An Air Engineer controls the pressurization of the fuselage. Aircraft are pressurized immediately after each take-off and de-pressurized immediately before each landing, including rollers. During cruise the cabin is normally maintained at 8.5 psi differential pressure for transport sorties and 9 psi differential on AR sorties. Prior to descent, on the majority of sorties, cabin differential is increased to 9 psi. Typically, 4 psi differential pressure is

33

achieved at an altitude of about 10,000-12,000 ft and 7 psi differential pressure is achieved at an altitude of about 24,000-26,000 ft.

3.4 Operational Loads Measurements

To validate the DT analysis described above, various Operational Load Measurement (OLM) Programmes have been conducted on RAF VC10 since 1986. The Programmes essentially involve fixing strain gauges to the areas of the airframe under evaluation and recording the loads experienced by the structure for numerous flight cycles. One such OLM Programme included the instrumentation of the fuselage crown of a RAF VC10 KMk2 as detailed at Figure 3-5.
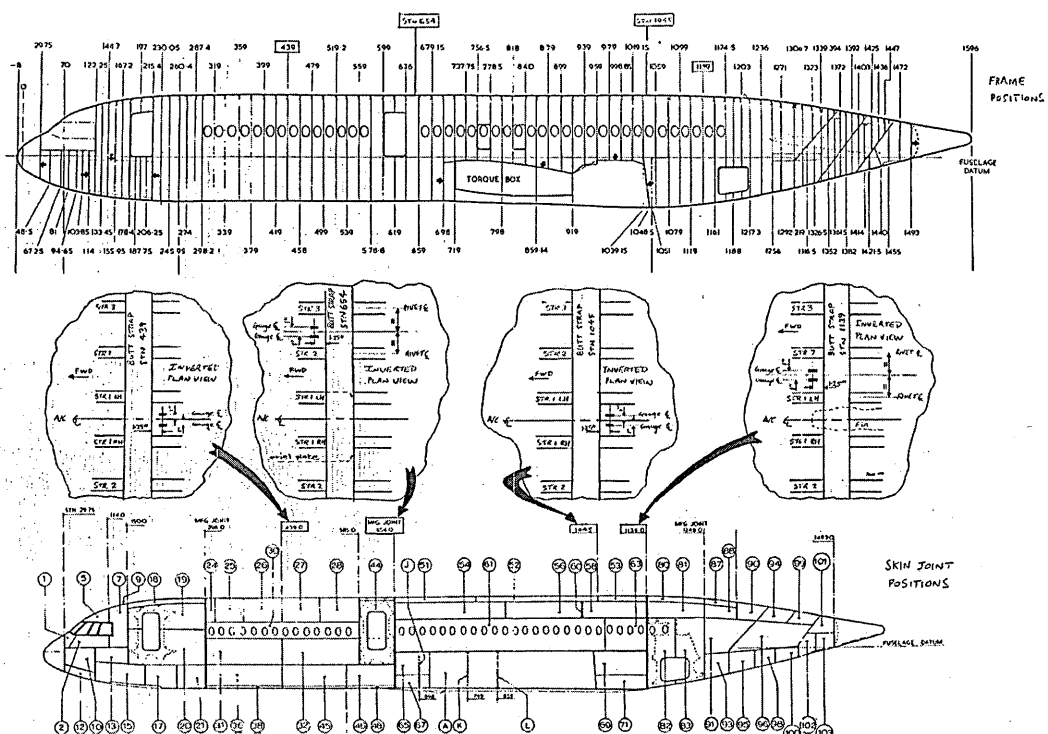
Figure 3-5: Location of Strain Gauge Bridges for Fuselage Butt Strap OLM Programme

As explained at Chapter 2, circumferential joints at the crown of the fuselage is an area susceptible to MSD but represents a less MSD researched area, with a more complex stress configuration than most of the longitudinal fuselage lap joints. After the data from the OLM Programme had been collected it was subjected to rain-flow analysis and then weighted in an appropriate manner to generate spectra for a typical VC10 KMk2 flight after taking into account all of the KMk2 SPCs. The spectra identified (more details of which can be found at Chapter 4 and Appendix A) that the longitudinal stresses at Fuselage Station (FS) 1045 were the highest of all 4 of the FS's analysed. It was therefore

decided to try to predict the onset of MSD in a RAF VC10 circumferential butt joint at the crown of the fuselage at FS 1045.

3.5 VC10 KMk2 – ZA142

The retired aircraft used to provide the extended fatigue test specimens, as detailed at Chapter 4, was a RAF VC10 KMk2 aircraft, military designation ZA142. This Standard VC10 aircraft first flew on 20 December 1963 and was delivered to Gulf Air on 22 Apr 1964 and entered RAF service in 1983. The aircraft retired from active RAF Service on 31 March 2001 and had accumulated a total of 50 456 flying hours and 19 127 flight cycles. The aircraft was then subjected to a teardown destructive examination during which 4, approximately one-metre square, sections were removed from the crown of the fuselage at FS 439, 654, 1045 and 1139. The results of the teardown examination had not been published during the compilation of this Thesis. The section of the fuselage removed from FS1045 was used to produce the extended fatigue specimens detailed at Chapter 4. Despite the fact that ZA142 was a standard VC10, it was still believed that the results of any analysis would still be fairly representative of the surviving variants.

3.6 Fuselage Station 1045 – Butt Joint Configuration

Fuselage Station 1045 is located aft of the wing torque box and main landing gear bay just before fuselage begins to narrow in the region of the empennage as detailed at Figure 3-6 & 3-7.
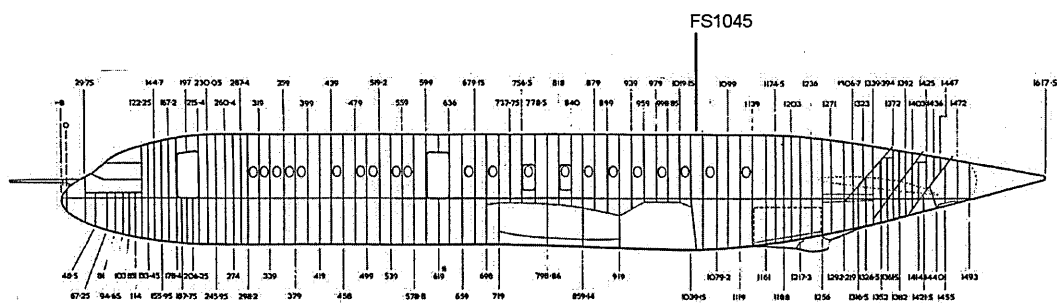
Figure 3-6: RAF VC10 Fuselage Station (FS) 1045

35
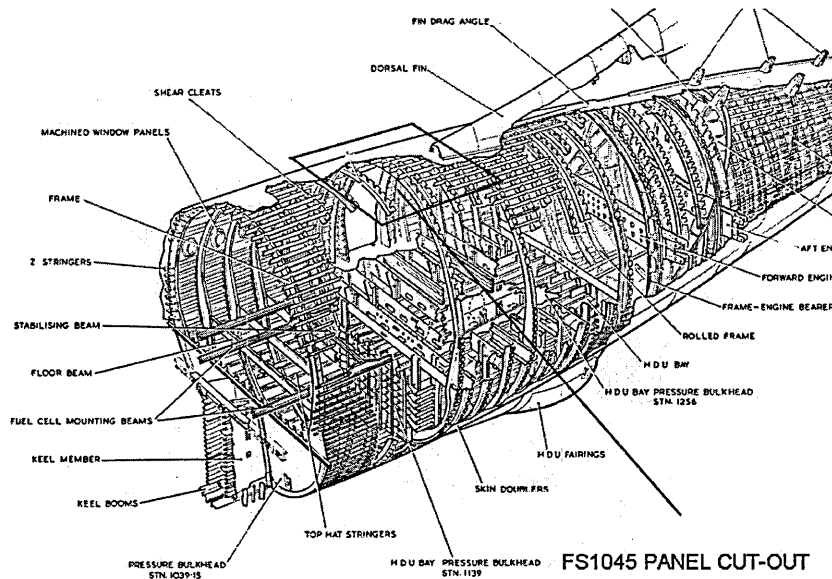
Figure 3-7: FS1045 Circumferential Butt Joint Panel Cutout

Prior to the removal of the panels from the crown of the fuselage, each area was labelled with boundaries and identification marks to indicate the location and orientation of the section with respect to the aircraft. The FS 1045 panel was approximately 1m long (longitudinal direction) with the circumferential butt joint in the middle and was 5 stringer bays wide (3 stringers either side of the centre line). A picture of the FS1045 panel is provided at Figure 3-8.
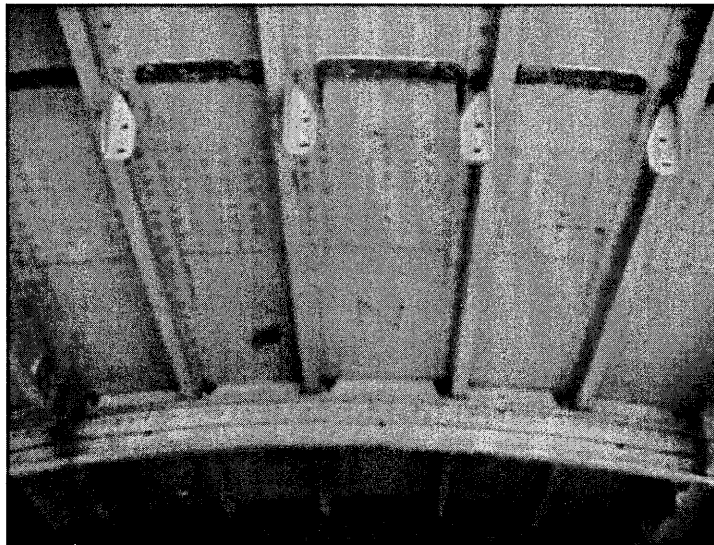
Figure 3-8: Picture of the Fuselage Panel Removed from FS 1045

The configuration of the butt joint is detailed at Figure 3-9 and Figure 3-10 below. The fuselage and the butt strap were constructed from L72 aluminium and wet assembled using PRC and 3/16 inch (VGS6424) rivets. The pitch

between stringers is approximately 230mm and the width of the Butt Strap is 165mm. The original Vickers drawings gave the forward fuselage skin thickness as 14swg (2.03mm) and the rearward skin as 15swg (1.83mm) with a butt joint thickness of 13swg (2.34mm). Once the panel had been cut into the specimens, detailed at Chapter 4, the thickness of the skin was checked and no difference in the thickness of the forward and rearward skin could be identified. Taking the primer and paint finish into consideration the thickness of the skins at FS1045 was determined to be 1.83mm. The butt joint was confirmed as being 2.34mm thick.
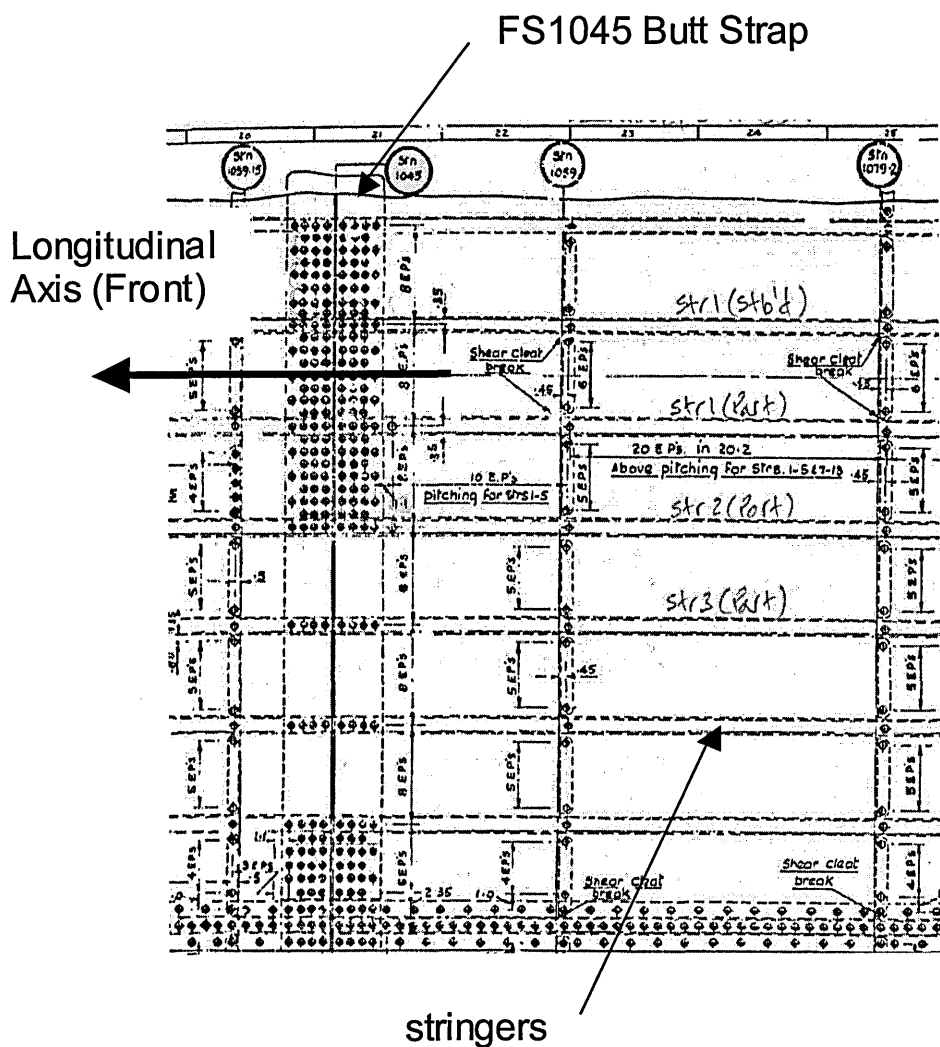
Figure 3-9: FS1045 Butt Strap Configuration

FS1045 Butt Strap

Longitudinal Axis
(Front)

stringer#1(port)

stringer#1(starboard
)
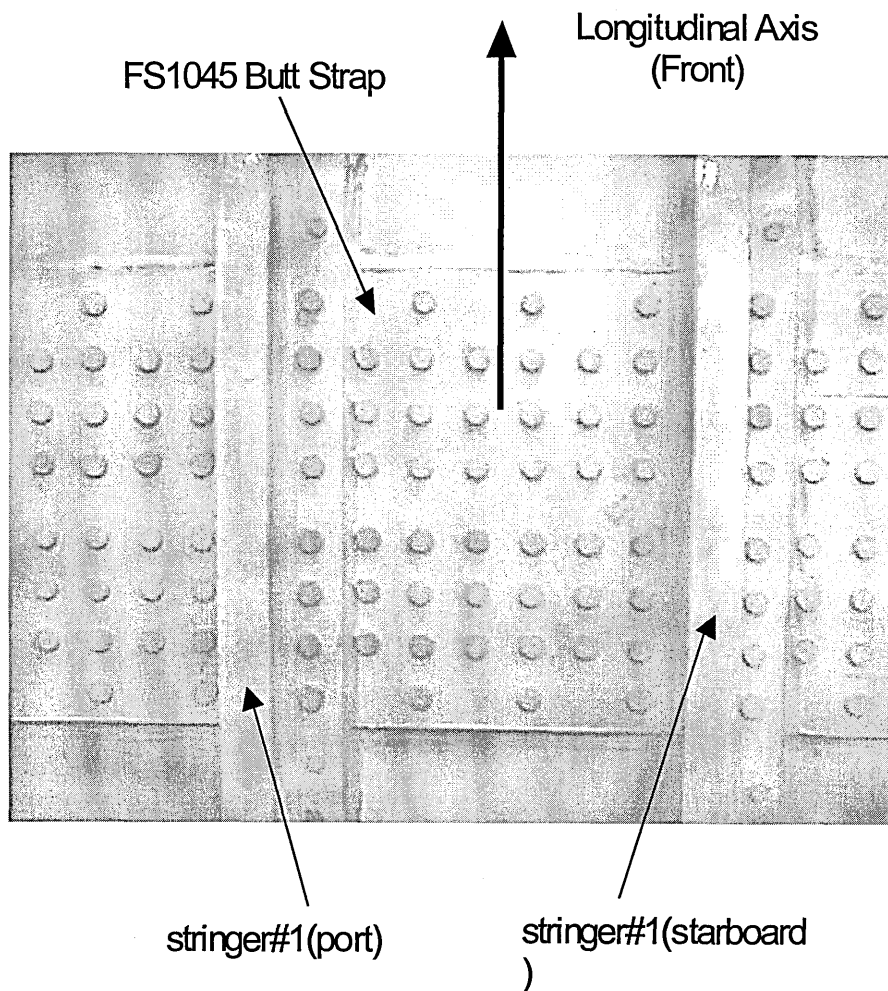
Figure 3-10: FS1045 Butt Joint

4 Extended Fatigue Testing

4.1 Introduction

The fuselage skin stress is due primarily to cabin pressurisation and fuselage bending. As detailed at Chapter 3, the cabin pressure differential can vary slightly but for the majority of the flight it is at a maximum of 9psi ($66.9KN/m^2$) producing an average hoop stress, as detailed at Chapter 5, of $68.8MN/m^2$ or $30.2MN/m^2$ in the circumferential butt joint. The fuselage bending at the FS 1045 circumferential butt joint was, however, determined during a RAF VC10 Operational Load Measurement (OLM) Programme, as detailed at Chapter 3, and varies considerably for different flights, manoeuvres, gusts and other varying loads (see Appendix A).

The maximum fuselage bending stress at the crown of FS1045 was determined to be 1.57 times greater than the average hoop stress but this factor increased to 6.6 times when local stresses were taken into consideration at the joint (see Chapter 5). As it was not possible to fatigue test the panel bi-axially it was decided to produce specimens for extended fatigue testing to failure using variable and constant amplitude uniaxial longitudinal (fuselage bending) loads derived from the RAF VC10 OLM Programme as detailed below. The biaxial stress state at the crown of FS1045 would then be analysed theoretically, as detailed at Chapter 5, to determine whether or not the results would have to be factored to take into account the hoop stresses not included in the extended uniaxial fatigue test. The final dimensions of the specimens along with the test procedure used and the results obtained, including observations made from the fracture surfaces, are provided within this Chapter.

4.2 Specimens

The fuselage panel used to produce the specimens was removed from the crown of RAF VC10 ZA142's fuselage at FS 1045. It was approximately 5 stringer bays wide (circumference) and 1m long (longitudinal axis) with a circumferential butt joint located approximately half way along its length as illustrated at Figure 4-1.

The forward and aft fuselage panels were constructed from 15swg (1.83mm) L72 superseded by L163, L164 (previously DTD610 equivalent to 2014A) aluminium alloy clad sheet. The butt joint consisted of a 166mm wide L72 (2014A) aluminium alloy clad butt strap with 8 equally spaced columns of alternatively 8 and 6, 4.76mm diameter, rivets (VGS6424) between each longitudinal stringer. The stringer pitch was 229.2mm producing a circumferential rivet pitch of 28.7mm for all but the outer most row of rivets which had a rivet pitch of 57.3mm. The longitudinal rivet pitch was 19.05mm as detailed at Figure 4-2.

stringer#1(stb'd)

logitudinal axis (fwd)

stringer#2(stb'd)

stringer#1(port)

stringer#3
(stb'd)

stringer#2
(port)

stringer#3
(port)

longitudinal
Z-stringers

FS 1045
circumferential
butt joint
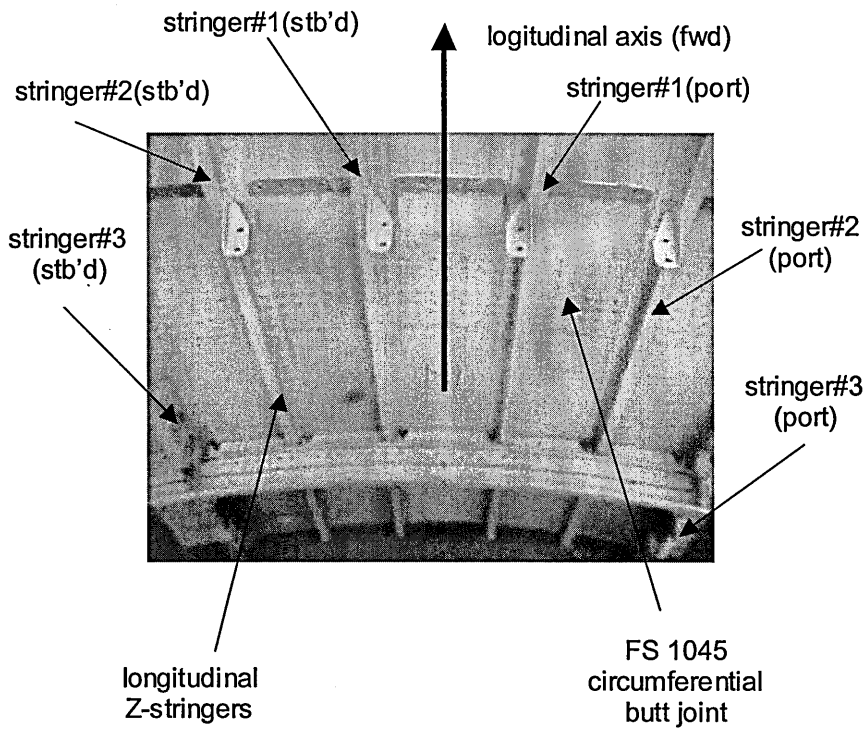
Figure 4-1: Crown Fuselage Panel (FS1045)

Z stringer
(bottom)

Longitudinal axis (fwd)

edge of
butt strap

57.3mm

83mm

57.2mm

butt
line

3.97mm diameter
pilot hole for **4.76mm**
diameter rivets
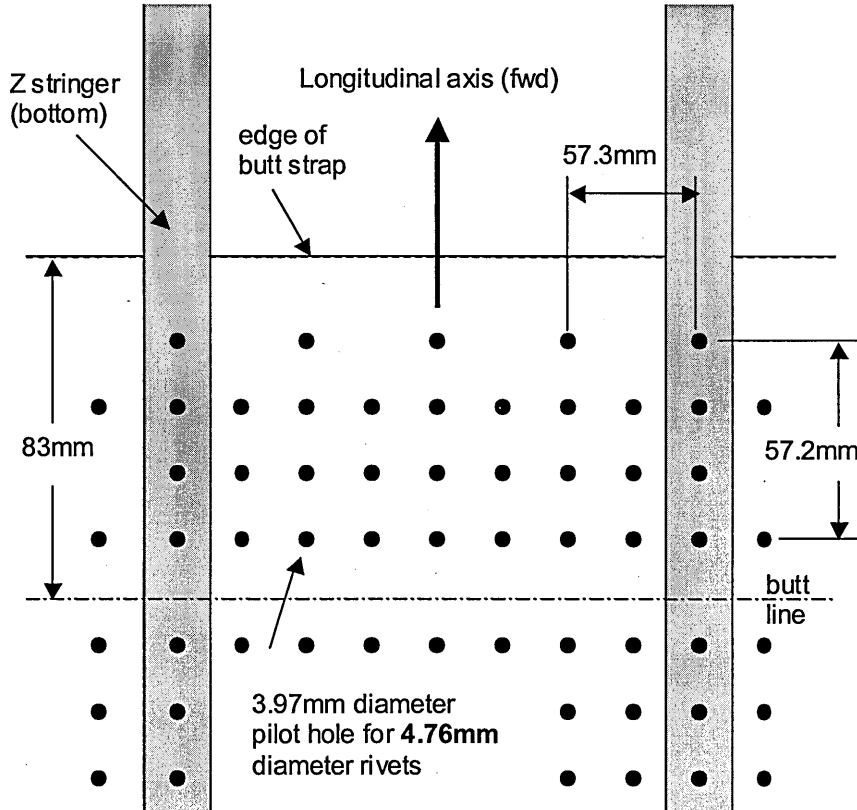
Figure 4-2: Internal Plan View & Dimensions of FS1045 Butt Joint

A total of 5 (15mm wide, 346mm long) specimens (3x8 rivet specimens and 2x6 rivets specimens) were obtained from each stringer bay as detailed in Figure 4-3. This resulted in a total of 25 specimens being obtained from the panel, the orientation and location of each specimen in relation to the stringers and the aircraft axes is detailed at Figure 4-4. Each 6 and 8 rivet specimen was initially cut out of the pane, using a band saw, along a line, as close as practicably possible, half way between each rivet column. The specimens were then machined to the final dimensions as detailed at Figure 4-5 with the rivets, as close as practicably possible, along the centre line of the specimen.
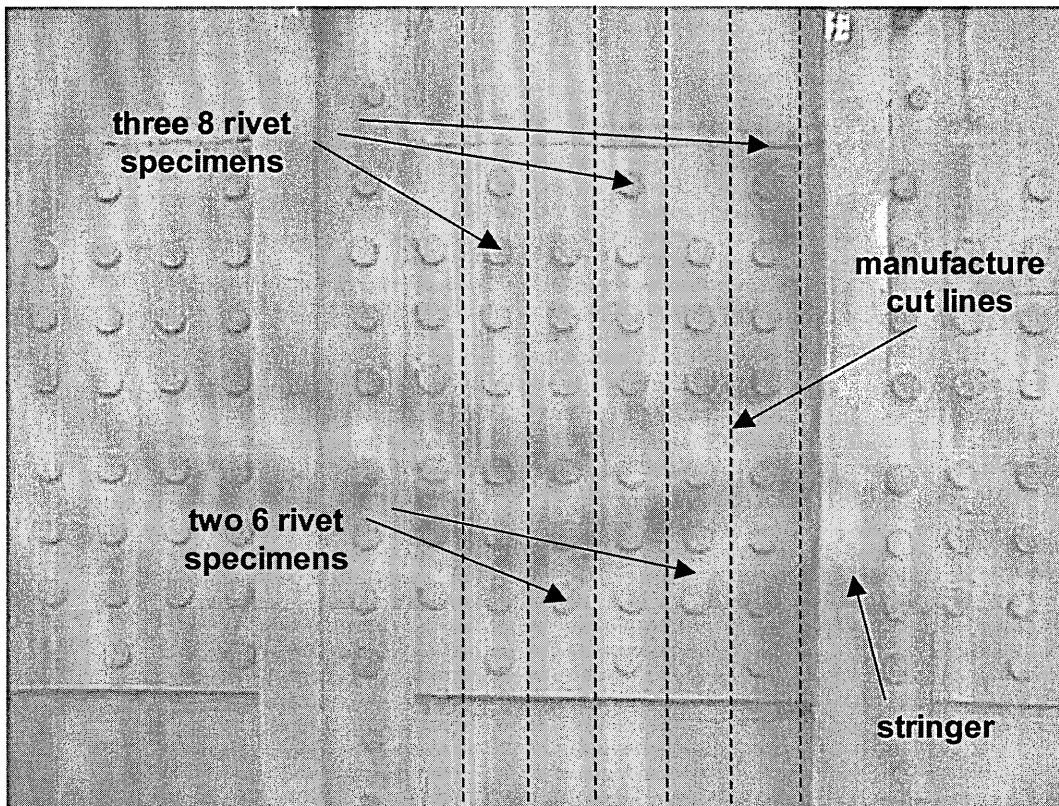
Figure 4-3: Number of Specimens Produced per Stringer Bay
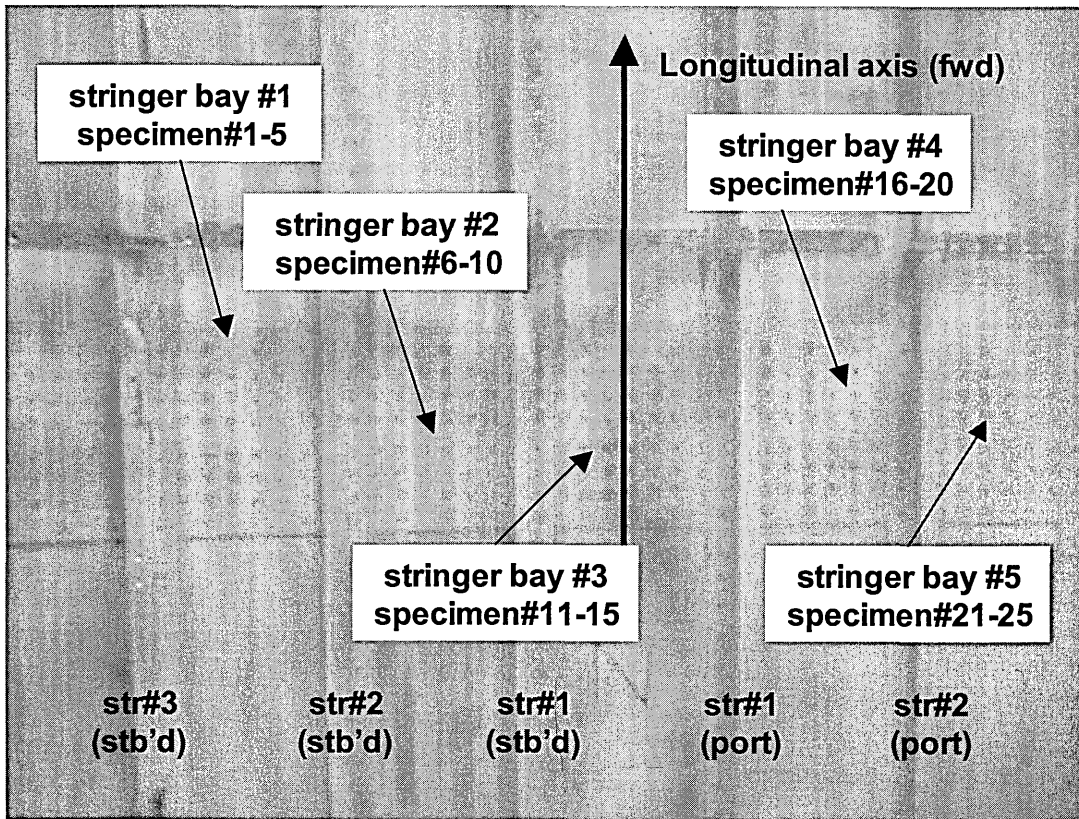
Figure 4-4: Specimen Location & Orientation
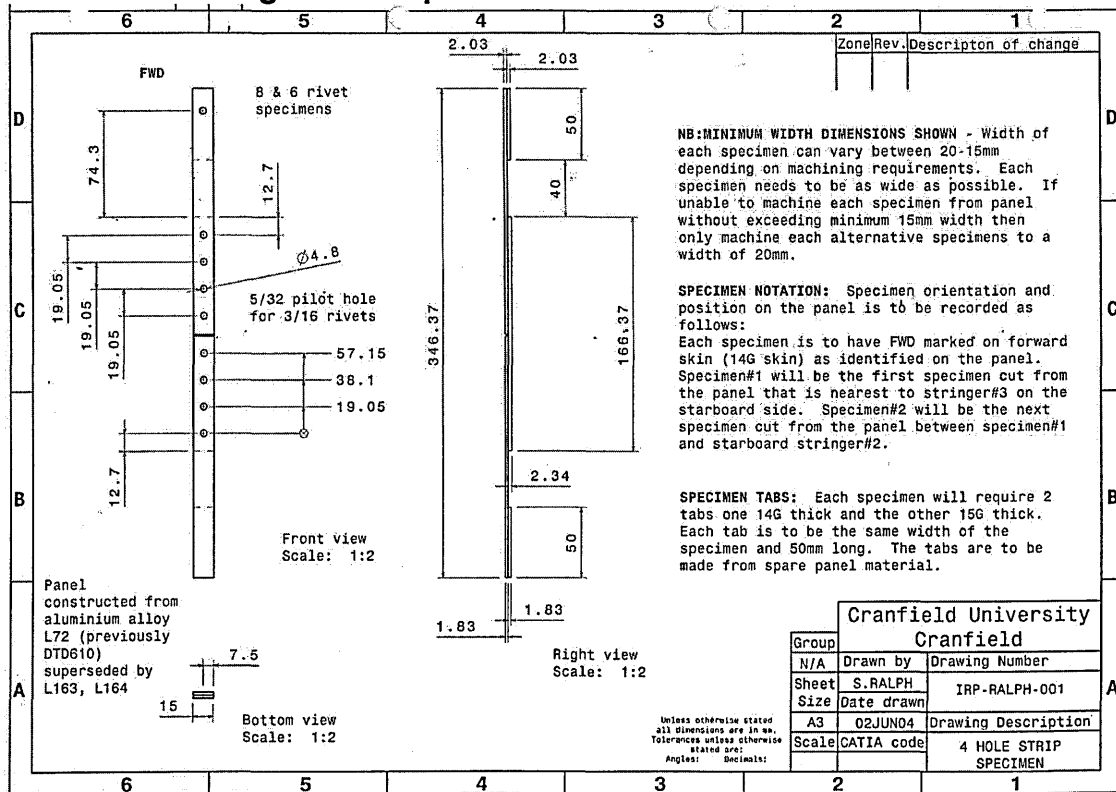
Figure 4-5: 6 & 8 Rivet Specimen Final Dimensions

Once the specimens had been machined to a width of 15mm the thickness of the forward and aft skins were checked. Contrary to the original VC10 drawings and as detailed in Figure 4-5, there was no difference in the thickness of the forward and aft skins, which, after taking into consideration the primer and paint, was established as being 1.83mm (15swg). No other discrepancies in the dimensions were identified. As shown in Figure 4-6 & 4-7 tabs, made from the same material as that of the skin, were attached to either end of the specimen using a general purpose adhesive. As there was no difference between the thickness of the forward and aft skin, 2 tabs were affixed to each end of the specimen (not depicted in Figure 4-5). This would ensure that the specimen could be clamped into the test machine (minimum clamp thickness of 2mm) and would also duplicate, as close as practicably possible, the transfer of load through the joint in the real aircraft.
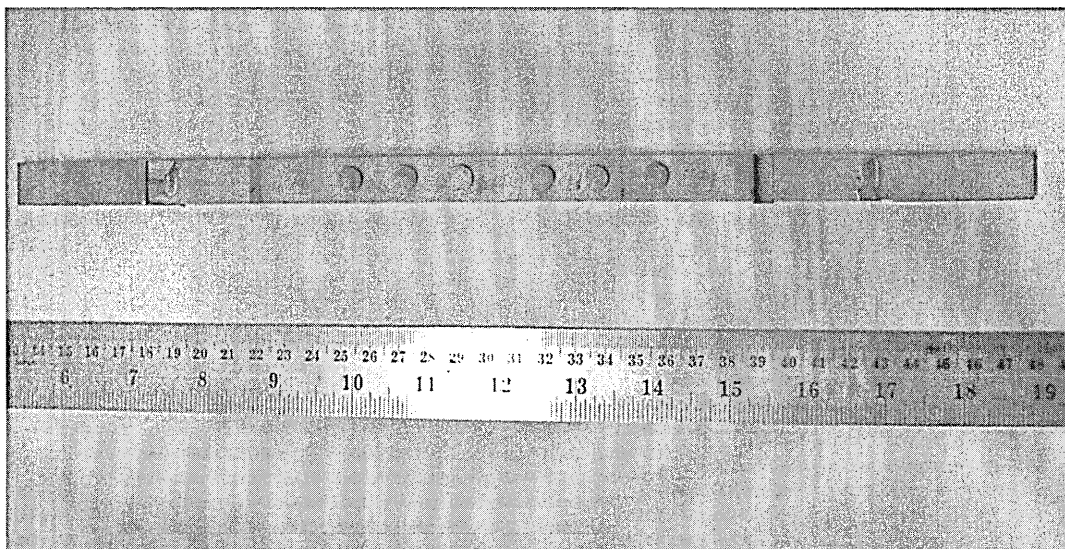
Figure 4-6: 6-riveted Specimen - Plan View
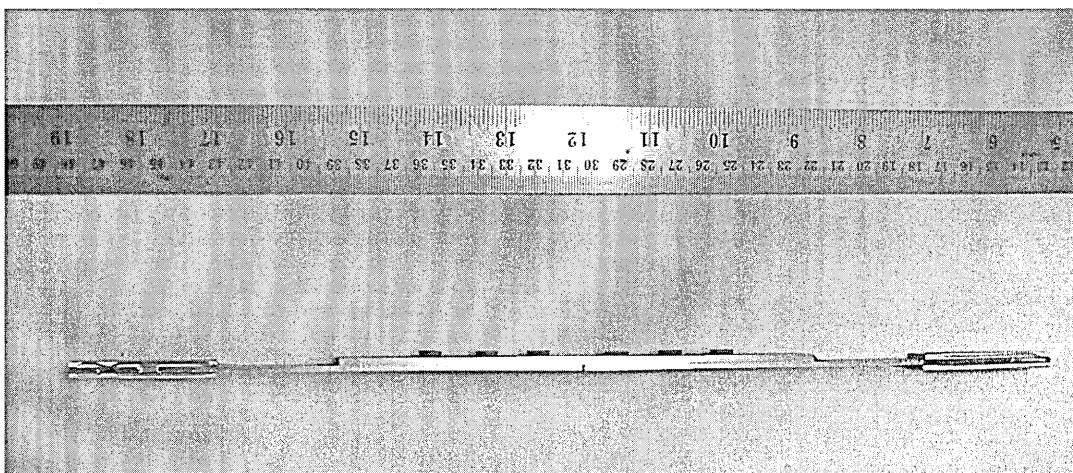
Figure 4-7: 6-riveted Specimen - Side View

43

4.3 Facility

The specimens were fatigue tested using a uniaxial digitally controlled 50KN Instron Test Facility as shown in Figure 4-6. The minimum applied load to the specimens was established as being 2.64KN and the average test load was 2.96KN, which are both below the recommended 10% of the maximum capability of the test machine. Ideally a lower capacity machine should have been used to test the specimens however, no other test machines were available and any induced errors would be minimised by the machine's digital control unit. No major problems were encountered during the tests but the machine did stop during some of the initial 2.64KN tests. The problem was resolved by recalibrating the test machine each time a new specimen was placed in the machine. All constant amplitude fatigue tests were conducted at 10Hz but planned variable amplitude tests could only be conducted at 6Hz due to the testing being at the lower capacity of the machine.
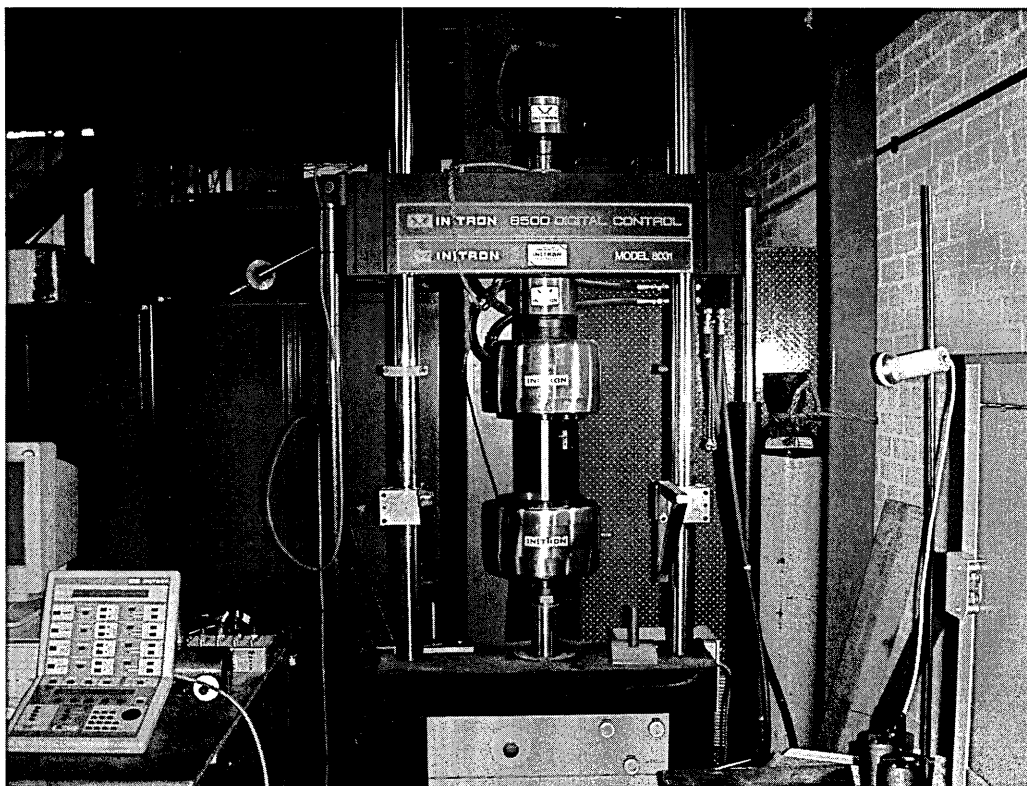
Figure 4-8: 50KN Uniaxial Instron Test Facility

The specimens were all tested in the same orientation, with the forward fuselage skin being clamped in the upper most hydraulic clamp and the other end of the specimen being clamped by the lower hydraulic clamp. Apart from the specimen being clamped at each of its ends, no other restraints were placed on the specimen during testing. Some lateral displacement of the specimen was observed, especially at the higher test loads detailed below, during the

tests. No precise measurements were taken but the displacement was no greater than 5mm at the highest load tested.

4.3.1 Programme

The original intension was to perform variable amplitude extended fatigue testing of some of the specimens to failure using an average longitudinal stress spectrum obtained from the OLM Programme. This spectrum is described in more detail at Appendix A. The results of these tests would then be used to compare the severity of the finally selected constant amplitude load, used for the majority of the testing, to determine whether it was equivalent to an average flight's fatigue damage. Due the project's time constraints, however, coupled with the realistic possibility of not being able to fail the specimens, within an appropriate time period, it was decided to start testing using a constant amplitude load.

The spectrum analysis performed at Appendix A was used to select an appropriate maximum and minimum load that would be experienced by the FS1045 butt joint during each average flight that the aircraft would perform. This load was then initially increased by 50% to determine whether or not the specimen would fail. Once it was established that the specimen would fail, within an acceptable time period in which to complete the thesis, the load was lowered until the actual loads experience by the aircraft were established to be sufficient to fail the specimens within an acceptable time period. The majority of the tests were then performed at this load in order to obtain sufficient data in which to determine a realistic average and standard deviation. The final test programme is detailed below, Table 4-1, but, due to time constraints, the 2 specimens identified for variable amplitude fatigue testing were unfortunately not tested to failure.

specimen type	total #	%	max sigma	# to test	# tested	amplitude	# to test	# tested	amplitude
	1	50%	1.63E+08	1	1	CA	0	0	VA
8 rivets	1	25%	1.35E+08	1	1	CA	0	0	VA
	2	11%	1.20E+08	2	2	CA	0	0	VA
	9	0%	1.08E+08	8	8	CA	1	0	VA
	2	-11%	9.60E+07	2	2	CA	0	0	VA
	15			14	14		1	0	
	1	50%	1.63E+08	1	1	CA	0	0	VA
6 rivets	1	25%	1.35E+08	1	1	CA	0	0	VA
	0	11%	1.20E+08	0	0	CA	0	0	VA
	6	0%	1.08E+08	5	5	CA	1	0	VA
	2	-11%	9.60E+07	2	2	CA	0	0	VA
	10			9	9		1	0	

Table 4-1: Specimen Test Programme

4.3.2 Variable Amplitude Loads

Operational longitudinal stresses at the FS1045 circumferential butt joint were obtained from an Operational Loads Measurements (OLM) Programme, detailed at Chapter 3, on a RAF VC10 KMk2. The fuselage stresses were obtained for various different Sortie Profile Codes (SPCs) including taxiing, take-off and landing and were then subjected to rainflow cycle counting analysis. Each sortie was then weighted accordingly to produce a spectrum that was representative of a typical RAF VC10 KMK2 flight. The spectrum was provided in order of magnitude only and was therefore rearranged, as detailed at Appendix A, to produce a typical flight spectrum with a more representative stress distribution. To simplify the analysis and to produce as realistic a spectrum as possible the final spectrum used amalgamated the average fatigue damage encountered for 10 flights into one spectrum as illustrated at Figure 4-9.
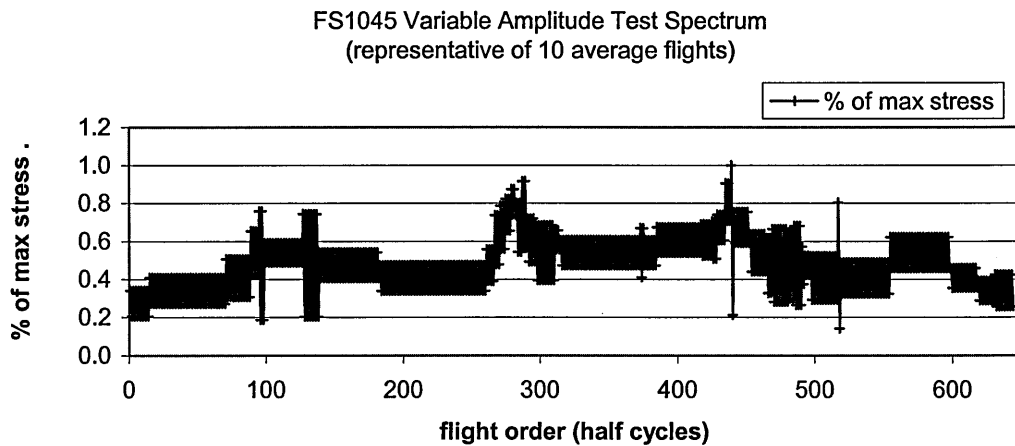
Figure 4-9: Variable Amplitude Test Spectrum

As detailed above, there was insufficient time in which to complete the 2 variable amplitude tests. Specimen#18 was tested for over 3 days, using the above spectrum at 6Hz, and did not fail and there was insufficient time in which to complete the test.

4.3.3 Constant Amplitude Loads

A total of 23 specimens were extended fatigue tested to failure using a constant amplitude load at 10Hz. The magnitude of the load varied during initial testing to ensure that the specimens would fail within a time frame suitable to complete the thesis. All the test loads were, however, a percentage of a maximum and minimum load taken directly from the variable amplitude spectrum obtained from the RAF VC10 OLM Programme. The cycle selected related to the maximum stress experienced during an average flight of 108MN/m^2, which

produced a minimum stress of 22.9MN/m^2. This meant that the stress ratio R was 0.21.

4.4 Results

A total of 25 specimens were prepared for extended uniaxial fatigue testing of which 23 were tested using various constant amplitude loads. The remaining 2 specimens were due to be tested using the variable amplitude load spectrum, identified above, but there was insufficient time in which to complete these tests.
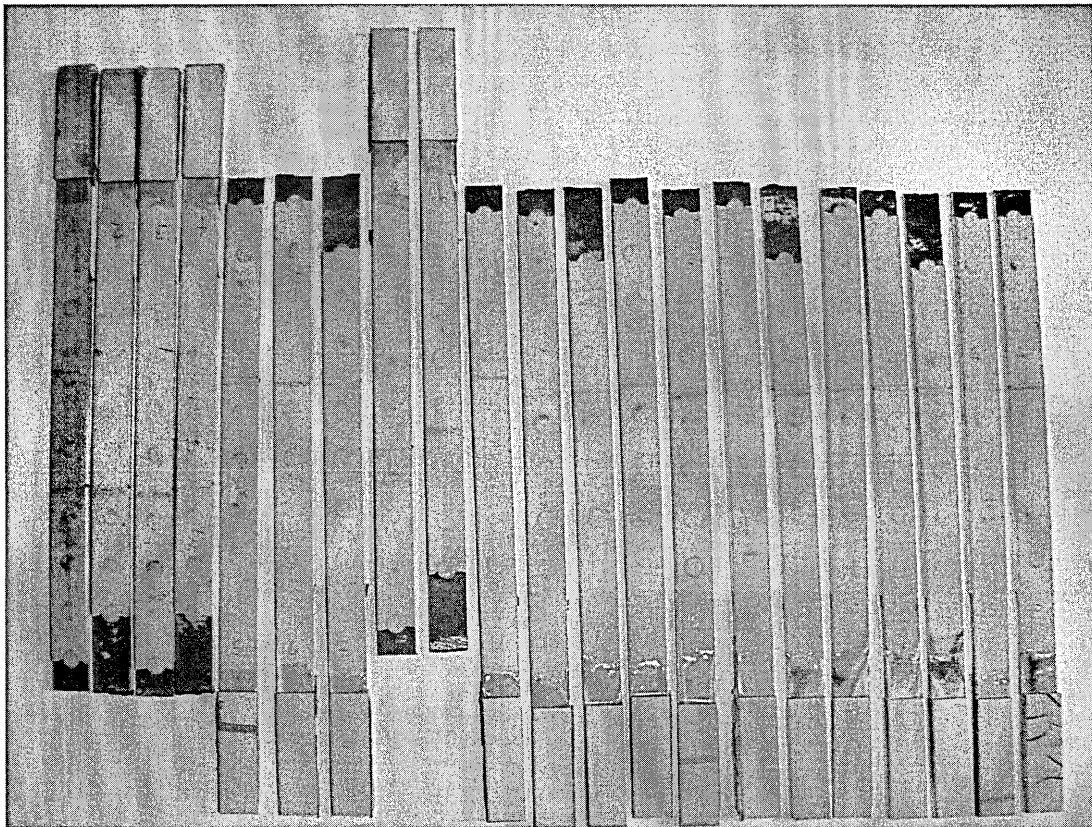
Figure 4-10: Tested Specimens (Forward Orientation at Top)

All of the 23 constant amplitude fatigue tested specimens failed, as expected, along the outer most rivet of the butt joint (Figure 4-11) apart from 2 specimens (specimen#19 & 24) which both failed along defects at the join. Of the 21 specimens that failed along the outer most rivet, 6 failed along the forward most outer row of rivets and 15 failed along the aft most row of rivet along the butt joint. The number of cycles it took to fail each specimen at each test load in the test facility is summarised at Figure 4-11.

TEST SPECIMEN S-N CHART
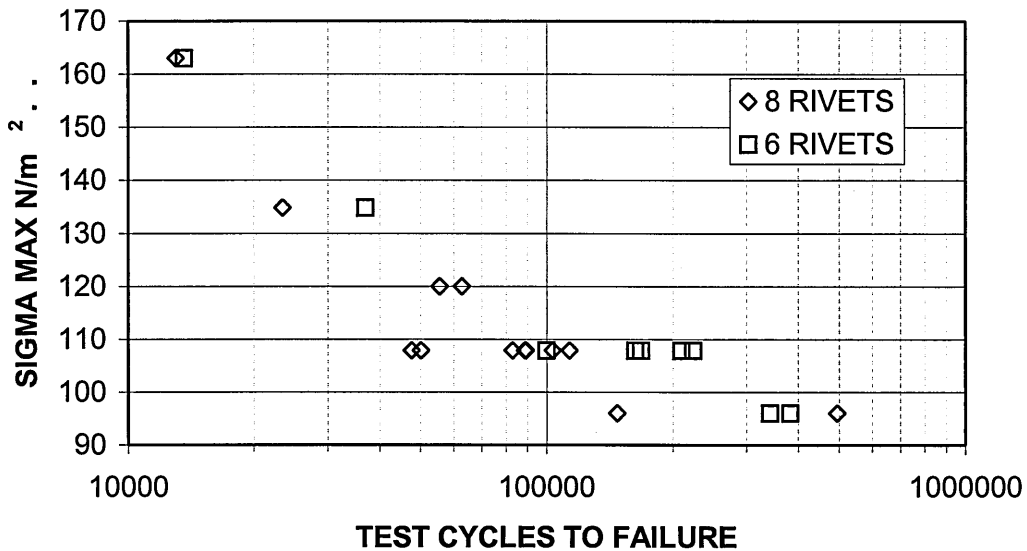
Figure 4-11: Test Specimen S-N Chart

It is clear from Figure 4-11 that the majority of the 6 rivet specimens took far longer to fail than the 8 rivet specimens, which were subjected to the same load. The precise number of cycles it took to fail each specimen along with any comments about each of the specimens is provided at Appendix B. As explained earlier, the specimens were cut from the fuselage panel with the rivets aligned, as close as practicably possible, along the centre line of the specimen. This aircraft, like most aircraft, was manufactured by hand and consequently, as detailed at Appendix B, 13 specimens had end rivets that were slightly offset from the centre line of the specimen. All the other specimens had rivets that were approximately located along the centre line of the specimen. It was also observed that the dimensions of the squeezed tail of the rivets varied considerably, as illustrated at Figure 4-12, with some examples of clinched rivet tails. No precise measurements were taken but approximate comparisons of average squeezed rivet tail dimensions (height and diameter) per specimens tested at the same load identified that those with smallest squeezed tail height and largest tail diameter took the longest to fail.

No variable amplitude tests were completed and the original intention to compare the number of cycles to failure with the selected constant amplitude load number of cycles to failure could therefore not be performed. The number of constant amplitude test cycles to failure was assumed to be representative of one flight, which was considered to be extremely conservative. The constant amplitude cycle used only occurred every 10 flights in the average variable

amplitude spectrum, detailed above, and despite there being a couple of similar large cycles in the spectrum they also did not occur during every average cycle.
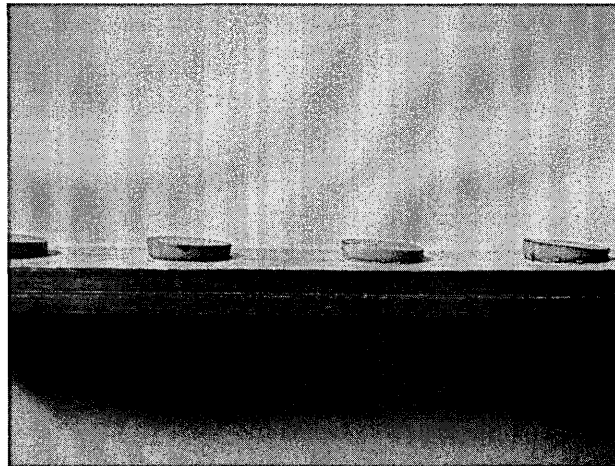
Figure 4-12: Examples of Clinched Rivets

4.4.1 Fracture Surfaces

All of the failed specimen fracture surfaces were examined using a microscope paying particular attention to the region of crack initiation. It was observed that, for all of the specimens that failed along the outer most rivet of the butt joint, a fatigue crack had initiated from the high stress concentration region at the tip of the countersink, as shown at Figure 4-13 & 4-14. The fatigue crack length varied but the average was approximately 3.5mm before the onset of fracture. Full details and images, at various magnifications, of the fracture surfaces of each specimen are provided at Appendix B.
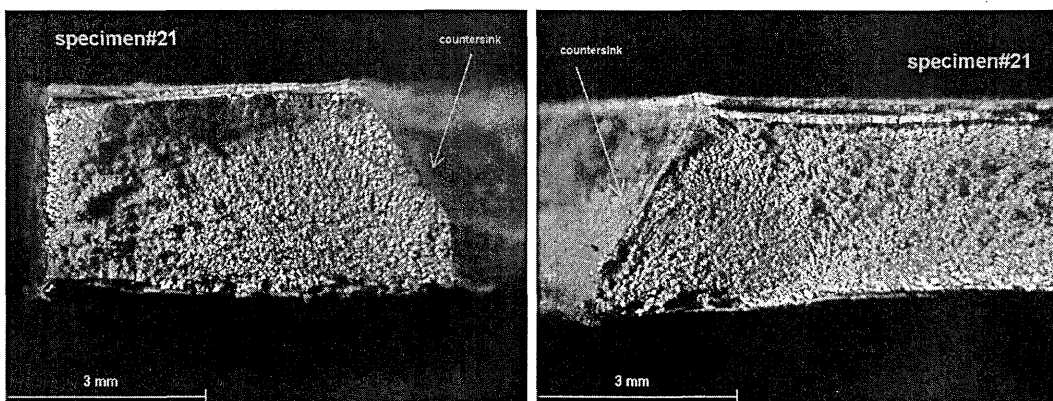
**Figure 4-13: Fracture Surfaces - Specimen#21
(both sides of countersink hole)**

Specimen#21 took 103485 constant amplitude test cycles to fail at a maximum load of 2.96KN. Fatigue cracks initiated at the tip of the countersink and propagated to approximately 3.5mm before the specimen fractured.
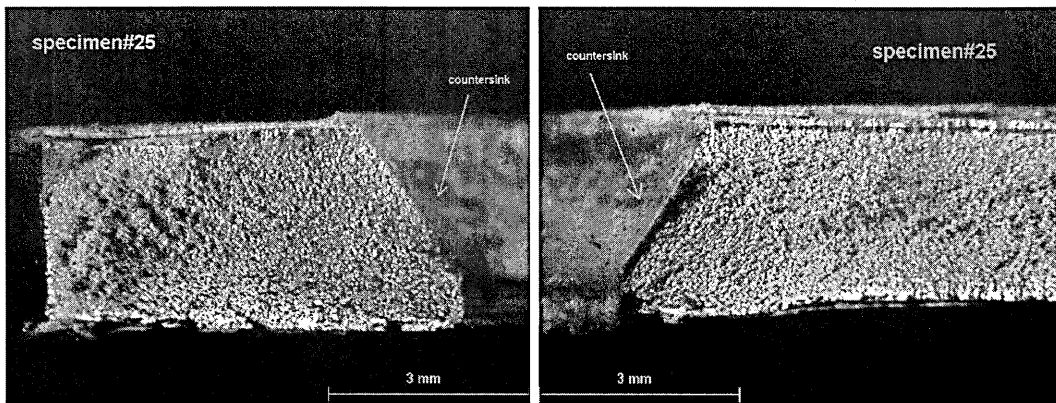
Figure 4-14: Fracture Surfaces - Specimen#25
(both sides of countersink hole)

Specimen#25 took 50168 constant amplitude test cycles to fail at a maximum load of 2.96KN. Fatigue cracks initiated at the tip of the countersink and propagated to approximately 3mm before the specimen fractured.

The fracture surfaces of the 2 specimens that failed along the butt strap, where the 2 skins meet, can be seen at Figure 4-15 & 4-16 below. In both cases it is clear that the fatigue crack has initiated from defects along the surface of the butt strap between the 2 adjacent skins.
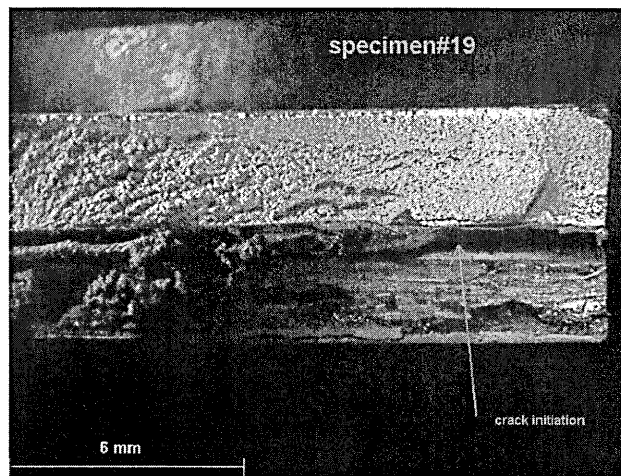
Figure 4-15: Fracture Surface – Specimen#19
(butt strap failed)

Speciemen#19 (6-rivet specimen) took 167923 constant amplitude test cycles to fail at a maximum load of 2.96KN. Fatigue cracks initiated at defects along the surface of the butt strap in the gap between the 2 outer skins.

50
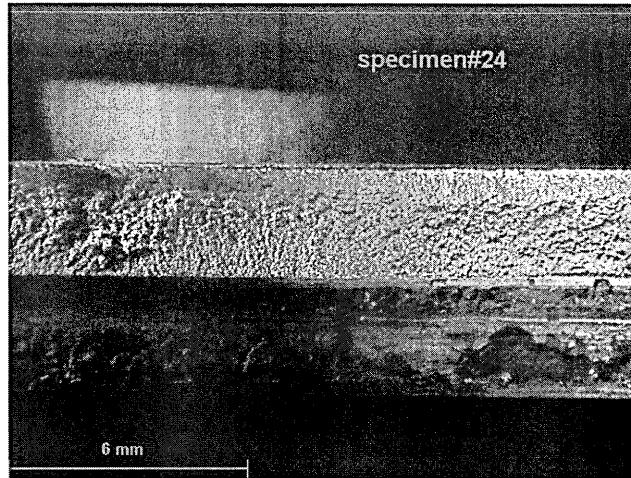
**Figure 4-16: Fracture Surface – Specimen#24
(butt strap failed)**

Speciemen#24 (6-rivet specimen) took 100057 constant amplitude test cycles to fail at a maximum load of 2.96KN. Fatigue cracks initiated at defects along the surface of the butt strap in the gap between the 2 outer skins.

From the observations made using the microscope, 6 specimens, that showed the most evidence of possible corrosion pitting, were selected for examination using the Scanning Electron Microscope (SEM). The SEM analysis identified the presence of predominantly 3 different mechanisms of fracture; ductile fracture, fatigue and a mixture of ductile and fatigue fracture. All 6 specimens showed signs of pre-existing defects and all of them also had small (50 microns) amorphous regions characteristic of the presence of corrosion as detailed at Figures 4-17 & 4-18 below.
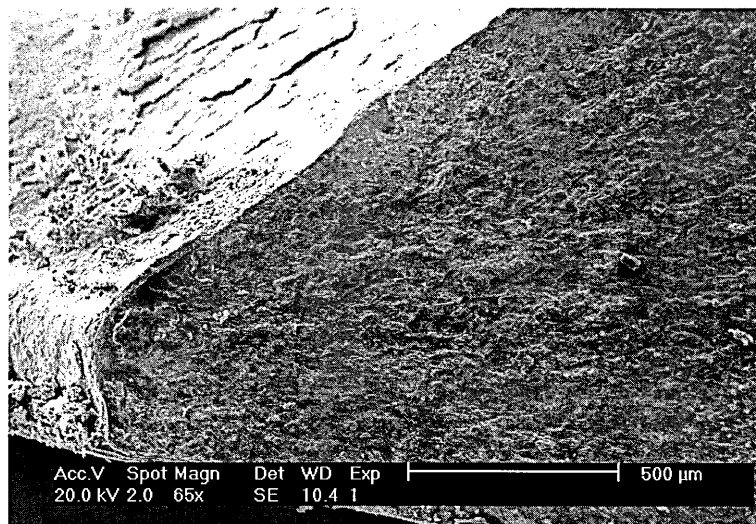
Figure 4-17: SEM Image of Specimen#9 Fracture Surface

Evidence of pre-existing fatigue and amorphous regions along the edge of the countersink
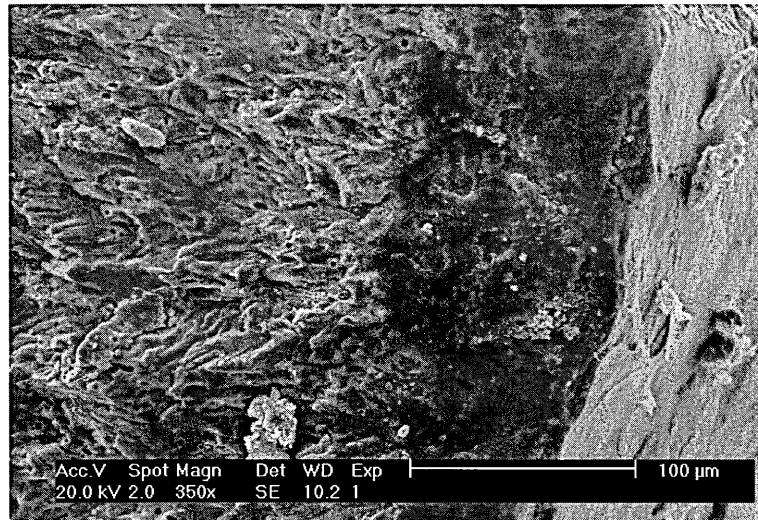
Figure 4-18: SEM Image of Specimen#9 Fracture Surface

Pre-existing fatigue and a larger amorphous region was evident at the extreme tip of the countersink on the other side of Speciemen#9's fracture surface.
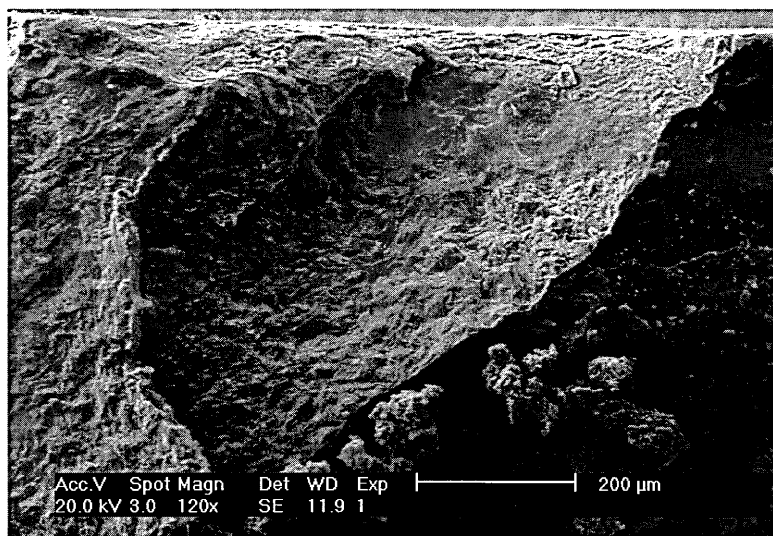
Figure 4-19: SEM Image of Specimen#15 Fracture Surface

A pre-existing defect and amorphous regions are evident at the extreme tip of the countersink.

It was also possible to detect that, from the SEM micrographs, the direction of crack propagation had changed probably due to the different loading conditions experienced in the uniaxial fatigue test facility as shown at Figure 4-20 below. Again, full details and images can be found at Appendix B.
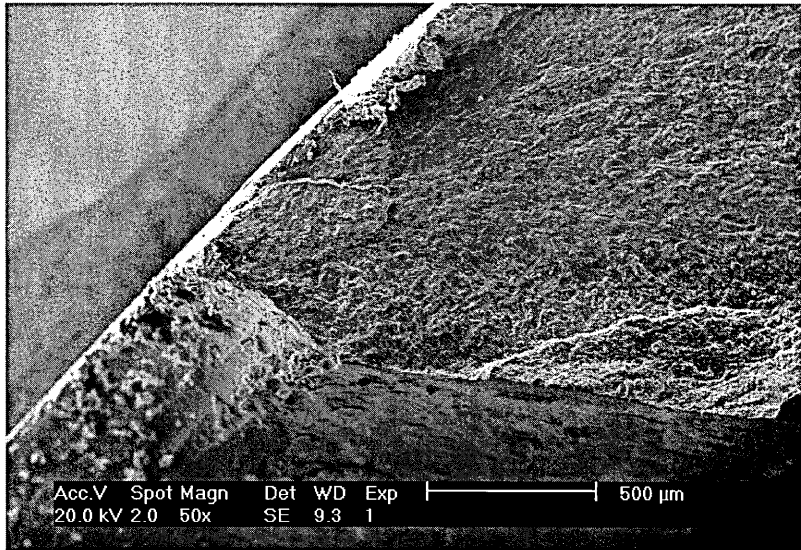
Figure 4-20: SEM Image of Specimen#21 Fracture Surface

Multiple fatigue fracture surface planes, some exhibiting pre-existing fatigue, are evident at the tip of the countersink. Higher magnification images suggest a possible change in the direction of some of the fatigue cracks

5 Biaxial Fatigue

5.1 Introduction

As explained at Chapter 4, the skin stress in a fuselage is due primarily to cabin pressurisation and fuselage bending. Cabin pressurisation will normally remain fairly constant throughout the flight whereas the fuselage bending stresses vary with respect to flight conditions and location along and around the fuselage. An Operational Loads Measurements (OLM) Programme performed on an RAF VC10 aircraft, detailed at Chapter 3, identified, out of the areas analysed, that the crown of FS1045 was subjected to some of the highest fuselage bending stresses. This section of the fuselage was therefore selected to predict the onset of MSD.

To obtain the necessary data to predict the onset of MSD, this section of the fuselage would need to be subjected to a, as realistic as possible, extended fatigue test. One of the best facilities currently available to conduct such a test is the FASTER facility as detailed at Reference ##. This test is able to replicate the conditions of the real aircraft. Unfortunately, such a test facility was not available to conduct the extended fatigue test of the RAF VC10 FS1045 fuselage panel. It was therefore decided to cut the fuselage panel into specimens, which would then be tested using uniaxial longitudinal bending stresses, as explained at Chapter 4.

Unfortunately, the significance of the circumferential hoop stresses are ignored during such uniaxial extended fatigue tests and it was therefore decided to attempt to determine, using theoretical methods, what impact the inclusion of the hoop stresses would have on the fatigue life of the specimens. This Chapter explains the method employed to determine the impact of the biaxial stress state, in the fuselage panel at FS1045, on the uniaxial extended fatigue test results provided at Chapter 4.

5.2 Biaxial Fatigue Theories

References 26, 29 & 30 illustrates some of the complexities of multiaxial fatigue as well as identifying some of the problems associated with the numerous methods available to evaluate fatigue life. The majority of the theories do, however, concentrate on the fact that fatigue cracks usually initiate from the surface of a component where there is a plane stress distribution. The strain distribution, however, is triaxial as there is usually an out-of-plane strain at the surface. The are predominantly 3 major criterion:

    a.   Principal Strain Criterion.

b. Principal Stress Criterion.

c. Maximum Shear Stain Criterion.

Each of these Criterion essentially maintain the form of the uniaxial strain life equation, detailed below, but with a modified strain parameter in accordance with the theory behind each criterion. Various constants are then applied to the equation to ensure that the proposed biaxial equation produces the same endurance for a uniaxial load condition as the unmodified uniaxial strain life equation.

In accordance with Reference 28, the Uniaxial Strain Life Equation is as follows:

$$\frac{\Delta \varepsilon}{2} = \frac{\sigma_f'}{E}(2N_f)^b + \varepsilon_f'(2N_f)^c$$

Where:

$\Delta \varepsilon$	=	Applied Strain Range.
$2N_f$	=	Endurance in Reversals.
σ_f'	=	Fatigue Strength Coefficient.
ε_f'	=	Fatigue Ductility Coefficient.
b	=	Fatigue Strength Exponent.
c	=	Fatigue Ductility Exponent.

5.2.1 Principal Strain Criterion (PSC)

For uniaxial stress the principal strain is the axial strain in the direction of the principal strain. As explained above, for plane stress conditions there is usually a triaxial strain distribution. In accordance with Reference 40, for any stress state it is always possible to define a new coordinate system, which has axes perpendicular to the planes, which the maximum normal stresses act and on which no shearing stresses act. These planes are called principal planes and the stresses normal to these planes are called principal stresses ($\sigma_1, \sigma_2, \sigma_3$) with corresponding principal strains ($\varepsilon_1, \varepsilon_2, \varepsilon_3$). The principal strain criterion proposes that fatigue cracks will initiate on planes that experience the largest amplitude of principal strain. The axial strain in the uniaxial strain life equation is therefore replaced by principal strain to produce the following multiaxial fatigue equation:

55

PSC Multiaxial Life Equation:

$$\frac{\Delta\varepsilon_1}{2} = \frac{\sigma'_f}{E}(2N_f)^b + \varepsilon'_f(2N_f)^c$$

In accordance with Reference 28, the PSC is recommended for the analysis of brittle material such as cast irons and very high strength steels. The criterion tends to give unsafe life estimates for ductile materials and would therefore not be appropriate for analysing the life of the FS1045 circumferential butt joint.

5.2.2 Principal Stress Criterion (PS'C)

Most early attempts to analyse biaxial fatigue where based on the Principal Stress Criterion (PS'C) which, as the name implies, is based on determining the principal stresses as defined above. The principal stresses for any stress state can be calculated using the following equations derived in Reference 40:

$$\sigma_{1,2} = \frac{\sigma_x + \sigma_y}{2} \pm \sqrt{\left(\frac{\sigma_x - \sigma_y}{2}\right)^2 + \tau_{xy}^2}$$

Once the principal stress is known the fatigue life is determined using the amplitude of the largest principal stress (σ_1) with a S-N chart obtained by testing an axially loaded specimen. The PS'C does not, therefore, take into consideration the effect of the second principal stress (σ_2) on the fatigue life. The PS'C should therefore only be used for brittle materials such as cast irons and high strength steels as it would give unsafe fatigue predictions for ductile materials. This criterion is therefore also not suitable for predicting the fatigue life of relatively ductile aluminium alloys.

5.2.3 Maximum Shear Strain Criterion

The Maximum Shear Strain Criterion (MSSC) proposes that fatigue cracks will initiate on planes, which experience the maximum shear strain amplitude. From the derivation of the principal stresses at Reference 40, it can also be shown that maximum and minimum shear stresses occur on planes 45^0 to the principal planes and are equal and opposite in value such that:

$$\tau_{max} = \frac{\sigma_1 - \sigma_2}{2}$$

Similarly, in accordance with Reference 40, the principal strains can be represented as follows:

$$\varepsilon_{1,2} = \frac{\varepsilon_x + \varepsilon_y}{2} \pm \sqrt{\left(\frac{\varepsilon_x - \varepsilon_y}{2}\right)^2 + \left(\frac{\gamma_{xy}}{2}\right)^2}$$

The maximum shear strain occurs on planes at 45^0 to the planes of the principal strains and is therefore calculated as follows:

$$\frac{\gamma_{max}}{2} = \frac{\varepsilon_1 - \varepsilon_3}{2}$$

Where

$$\varepsilon_3 = \frac{-\nu}{1-\nu}\left(\varepsilon_1 - \varepsilon_2\right)$$

The applied strain in the Uniaxial Life Strain Equation is therefore replaced by maximum shear strain and various different theories then manipulate the right hand side of the equation to produce similar fatigue lives for the uniaxial case.

The Brown-Miller takes the above criterion further by proposing that the maximum fatigue damage occurs on the plane which experiences the maximum shear strain amplitude and is a function of both the shear strain and the strain normal to the plane as illustrated in Figure 5-1 below:
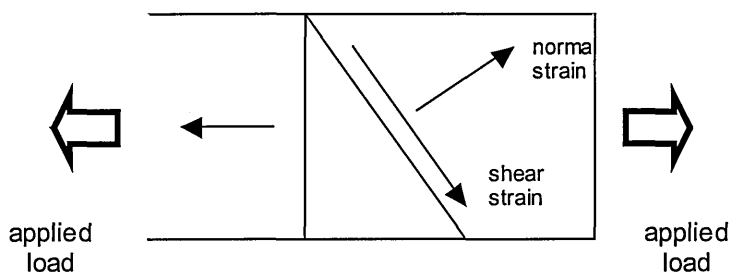
Figure 5-1: Plane of Maximum Shear Strain

The strain normal to the maximum shear strain is (ε_n) and can be derived in a similar manner to the equations above, as shown at Reference 40, to give:

$$\varepsilon_n = \frac{\varepsilon_1 + \varepsilon_3}{2}$$

The applied strain in the Uniaxial Strain Life Equation is now replaced by the maximum shear strain and the normal strain to produce the following equation:

$$\frac{\Delta\gamma_{max}}{2} + \frac{\Delta\varepsilon_n}{2} = C_1 \frac{\sigma'_f}{E}(2N_f)^b + C_2\varepsilon'_f(2N_f)^c$$

Assuming that the fatigue cracks initiate on the plane of maximum shear strain, Miller, Brown and Kandil calculated that the constants C1 and C2 were equal to 1.65 and 1.75 respectively. The Kandil-Brown-Miller strain life equation is therefore as follows:

$$\frac{\Delta\gamma_{max}}{2} + \frac{\Delta\varepsilon_n}{2} = 1.65\frac{\sigma'_f}{E}(2N_f)^b + 1.75\varepsilon'_f(2N_f)^c$$

In accordance with Reference 28, the above equation gives the most realistic life estimates for ductile materials and was therefore selected to determine the biaxial fatigue life of the FS1045 circumferential butt joint. The Uniaxial Strain Life Equation would then be used to determine fatigue life of the butt joint under the uniaxial load used in the extended fatigue test and compared with the result obtained for the biaxial case.

The Uniaxial Strain Life Equation can also be modified to take into account the maximum shear strain produced by the uniaxial load, in a similar manner to that used above, as follows:

Replacing the applied strain in the Uniaxial Strain Life Equation with shear strain the equation becomes:

$$\frac{\Delta\gamma}{2} = C_1 \frac{\sigma'_f}{E}(2N_f)^b + C_2\varepsilon'_f(2N_f)^c$$

This time, in accordance with Reference 28, the constants C1 and C2 can be evaluated by making the above equation and the Uniaxial Strain Life Equation give the same endurance for uniaxial stresses. For uniaxial stress, with an axial strain ε_1, the principal strains $\varepsilon_2 = \varepsilon_3 = -\nu\varepsilon_1$ it therefore follows that:

$$\gamma_{max} = \varepsilon_1 - \varepsilon_3 = \varepsilon_1 - (-\nu\varepsilon_1) = (1+\nu)\varepsilon_1$$

For uniaxial stresses, the shear strain amplitude is $(1+\nu)$ times the direct strain amplitude, so the equation can be re-written as follows:

$$\frac{\Delta\gamma}{2} = \left(1+\nu_e\right)\frac{\sigma_f'}{E}\left(2N_f\right)^b + \left(1+\nu_p\right)\varepsilon_f'\left(2N_f\right)^c$$

For elastic strains Poisson's ration (ν_e) is approximately 0.3 and for purely plastic strains Poisson's ration (ν_p) is 0.5. The Uniaxial Strain Life Equation expressed in terms of maximum shear strain is as follows:

$$\frac{\Delta\gamma}{2} = 1.3\frac{\sigma_f'}{E}\left(2N_f\right)^b + 1.5\varepsilon_f'\left(2N_f\right)^c$$

Reference 28 states that this equation tends to give conservative life estimates for ductile materials and was therefore used in the following analysis to give another comparison in the uniaxial and biaxial fatigue lives of the FS1045 circumferential butt joint.

5.3 Stress & Strain Calculations

To determine the uniaxial and biaxial principal strains at the FS1045 circumferential butt joint it was first necessary to calculate the local stresses at the outer most rivet of the joint. As explained at Chapter 3 & 4, the cabin pressure differential can vary slightly but for the majority of the flight it is at a maximum of 9psi (66.9KN/m^2). The fuselage bending stresses, however, vary considerably for different flight conditions, manoeuvres, gusts and other varying loads. The FS 1045 circumferential butt joint stresses were, however, determined during a RAF VC10 Operational Load Measurement (OLM) Programme, as detailed at Chapter 3. The stress spectrum produced, see Appendix A, identifies that the stress in the fuselage skin, at FS1045, reaches a maximum of 108MN/m^2 and a minimum of 22.9MN/m^2.

To determine the stresses at the outer most rivet hole of the butt joint, were the specimens fractured, a Finite Element Model of the butt joint could have been produced but unfortunately, due to the time restrictions of the Project, it was decided early in the Project that this would not be possible. There is however a significant amount of research on determining the stresses at different rivet positions throughout various different fuselage joints. Reference 34 is an excellent example of such work and was therefore used to evaluate the stress at the outer most rivet of the FS1045 butt joint.

The outer most rivet load was calculated using the following graph, Figure 5-2, from Reference 34. The thickness of the butt strap (t_2), as detailed at Chapter

4, is 13swg (0.09inches, 2.34mm) and the thickness of the skin panel (t_1) is 15swg (0.07inches, 1.83mm). The load on the outer most rivet per every 6.9MN/m^2 (1KSI) of gross stress (σ_{gr}) was therefore calculated, from Figure 5-2, as being 111.2N. Therefore, with a maximum gross stress of 108MN/m^2 the load on the outer most rivet was 1.739.8N.

SKIN THICKNESS t_1 (INCHES)

FIRST ATTACHMENT LOAD PER 1 KSI GROSS STRESS

FIRST ATTACHMENT

1 KSI

SKIN THICKNESS t_2 (INCHES)
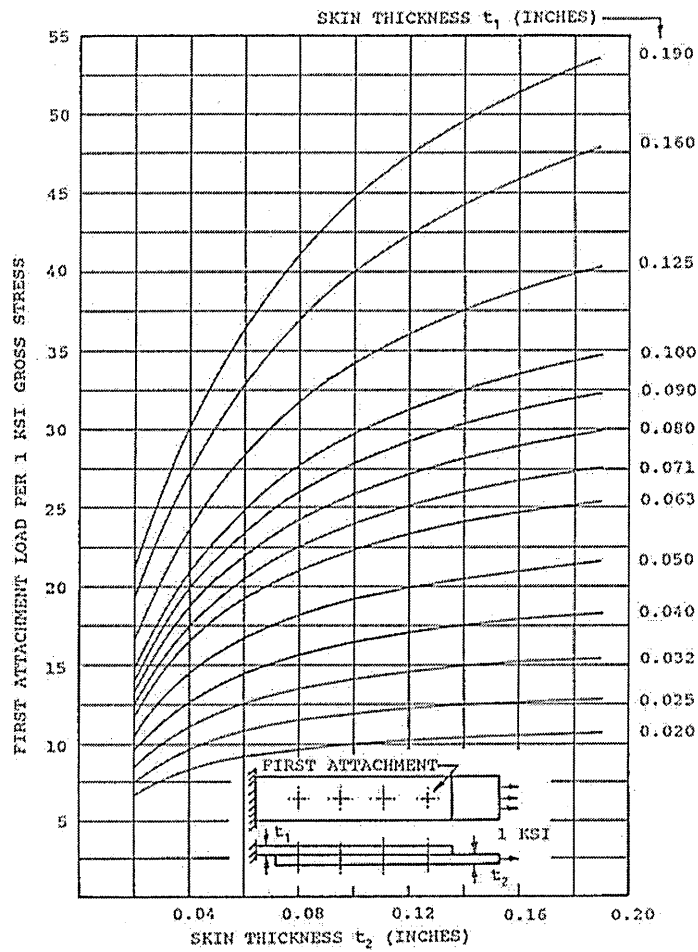
Figure 5-2: First Fastener Load per 1 KSI Gross Stress

The diameter of the rivets were 4.76mm, so the bearing stress (σ_{br}) on the outer most rivet of the butt joint was therefore calculated as follows:

$$\sigma_{br} = \frac{1739.8}{1.83 \times 10^{-3} \times 4.76 \times 10^{-3}} = 199.8 \times 10^{6} N$$

The ration of bearing stress to gross stress was therefore:

$$\frac{\sigma_{br}}{\sigma_{gr}} = \frac{199.8}{108} = 1.85$$

60

The fuselage circumferential hoop stresses were calculated using the following thin walled cylinder approximation:

$$\sigma_h = \frac{\Delta P \times R}{t}$$

Where

σ_h = Hoop Stress

ΔP = Pressure Differential

R = Radius of Fuselage

t = Skin Thickness

With a maximum pressure differential of 66.9KN/m2 (9psi plus 0.7psi suction) and a fuselage radius of 1.88m, the average Hoop Stress in the fuselage was therefore calculated as follows:

$$\sigma_h = \frac{66.9 \times 10^3 \times 1.8796}{1.83 \times 10^{-3}} = 68.7 MN/m^2$$

The Hoop Stress in the butt joint, where the total skin thickness is 4.17mm, is as follows:

$$\sigma_h = \frac{66.9 \times 10^3 \times 1.8796}{4.17 \times 10^{-3}} = 30.2 MN/m^2$$

The maximum fuselage bending stress at the crown of FS1045 was, therefore, determined to be 1.57 times greater than the average hoop stress but this factor increased to 6.6 times when the local stresses, determined above, were taken into consideration at the joint.

5.3.1 Uniaxial Analysis

To determine the uniaxial fatigue life of the butt joint using the equations detailed above it is necessary to calculate the applied strain and the shear strain at the outer most rivet. The only readily available cyclic material data was for aluminium alloy 2023 – T3 (Reference 33) and, although this is not exactly the same as the equivalent VC10 fuselage material (2014A), this data was used throughout the uniaxial and biaxial fatigue endurance comparisons. A list of the material data is detailed at Appendix C.

61

As detailed above, the maximum local longitudinal (bending) stress at the outer rivet is 199.8MN/m2. For the uniaxial case, this is the only applied stress. The maximum applied strain was therefore calculated as follows:

$$\varepsilon_{1(max)} = \frac{\sigma_1}{E} = \frac{199.8 \times 10^6}{74 \times 10^9} = 0.0027$$

The minimum local longitudinal (bending) stress at the outer rivet was 42.4MN/m2 and the minimum applied strain was therefore;

$$\varepsilon_{1(min)} = \frac{\sigma_1}{E} = \frac{42.4 \times 10^6}{74 \times 10^9} = 0.00057$$

The range of strain for the uniaxial case was therefore:

$$\frac{\Delta\varepsilon}{2} = \frac{\left(\varepsilon_{1(max)} - \varepsilon_{1(min)}\right)}{2} = 0.00106$$

The range of maximum shear strain was calculated using:

$$\frac{\gamma_{max}}{2} = \frac{(1-\nu)}{2}\varepsilon_1$$

This was determined for both maximum and minimum principal strains and the final range in maximum shear strain was determined as follows:

$$\frac{\Delta\gamma_{max}}{2} = \left(\frac{\gamma_{max}}{2}\right)_{max} - \left(\frac{\gamma_{max}}{2}\right)_{min} = 0.00142$$

5.3.2 Biaxial Analysis

To determine the biaxial fatigue life of the butt joint using the equations detailed above it is necessary to calculate the normal strain and the maximum shear strain at the outer most rivet. Again, the only readily available cyclic material data was for aluminium alloy 2023 – T3 (Reference 33) and, although this is not exactly the same as the equivalent VC10 fuselage material (2014A), this data was used throughout the uniaxial and biaxial fatigue endurance comparisons. A list of the material data is provided at Appendix C.

The range of normal and maximum shear strains were calculated using the following equations:

$$\frac{\gamma_{max}}{2} = \frac{\varepsilon_1 - \varepsilon_3}{2} \quad \text{and} \quad \varepsilon_n = \frac{\varepsilon_1 + \varepsilon_3}{2}$$

As there was no applied shear stress (assumed to be zero) the maximum principal stresses at the outer most rivet of the butt joint were:

For the maximum longitudinal (bending) stress:

$$\sigma_{1(max)} = 199.8 MN/m^2$$

$$\sigma_{2(max)} = 30.2 MN/m^2$$

For the minimum Longitudinal (bending) stress:

$$\sigma_{1(min)} = 42.4 MN/m^2$$

$$\sigma_{2(min)} = 30.2 MN/m^2$$

The strains for each of the above stress states were then calculated using the following equations:

$$\varepsilon_1 = \frac{1}{E}\left(\sigma_1 - \nu\sigma_2\right) \quad \text{and} \quad \varepsilon_3 = \frac{-\nu}{E}\left(\sigma_1 + \sigma_2\right)$$

The full analysis is provided at Appendix C and the calculated strains, above, were then used to calculate the range of maximum shear strain as follows;

$$\frac{\Delta\gamma_{max}}{2} = 1.796 \times 10^{-3} - 3.81 \times 10^{-4} = 1.42 \times 10^{-3}$$

Similarly, the range of normal strain was calculated as follows:

$$\frac{\Delta\varepsilon_n}{2} = 3.85 \times 10^{-4} - 2.86 \times 10^{-5} = 3.56 \times 10^{-4}$$

5.4 Fatigue Calculations

5.4.1 Uniaxial Analysis

For the Uniaxial Strain Life Equation:

$$\frac{\Delta\varepsilon}{2} = \frac{\sigma_f'}{E}(2N_f)^b + \varepsilon_f'(2N_f)^c$$

The applied strains, calculated above, were substituted into this equation along with the cyclic material constants obtained from Reference 33 and listed at Appendix C as follows:

$$1.064\text{x}10^{-3} = 1.95\text{x}10^{-3}(2N_f)^{-0.114} + 1.765(2N_f)^{-0.927}$$

The equation was then solved using the spreadsheet detailed at Appendix C.

For the Uniaxial Maximum Shear Strain Equation:

$$\frac{\Delta\gamma}{2} = 1.3\frac{\sigma_f'}{E}(2N_f)^b + 1.5\varepsilon_f'(2N_f)^c$$

The maximum shear strains, calculated above, were substituted into this modified Uniaxial Strain Life Equation, along with the appropriate cyclic material constants from Reference 33 to produce the following equation:

$$1.415\text{x}10^{-3} = 2.53\text{x}10^{-3}(2N_f)^{-0.114} + 2.648(2N_f)^{-0.927}$$

Again, this equation was solved using the spreadsheet at Appendix C.

5.4.2 Biaxial Analysis

For the Kandil-Miller-Brown Strain Life Equation:

$$\frac{\Delta\gamma_{max}}{2} + \frac{\Delta\varepsilon_n}{2} = 1.65\frac{\sigma_f'}{E}(2N_f)^b + 1.75\varepsilon_f'(2N_f)^c$$

The biaxial maximum shear strain and normal strain, calculated above, were substituted into the above equation along with the appropriate cyclic material constants from Reference 33 to produce the following:

$$1.771 \times 10^{-3} = 3.21 \times 10^{-3}(2N_f)^{-0.114} + 3.09(2N_f)^{-0.927}$$

This equation was also solved using the spreadsheet at Appendix C.

5.5 Comparison of Uniaxial & Biaxial Fatigue Calculations

The results of the above analysis are summarised at Table 5-1 below. The analysis essentially identifies that fatigue endurance of the biaxial stress condition experienced at FS1045 circumferential butt joint is not significantly affected by the presence of the hoop stress. The local longitudinal stress in approximately 6.6 times greater than the equivalent local hoop stress and is the predominant factor in deciding the fatigue endurance of the joint. The results of the uniaxial extended fatigue test were therefore not altered to take account of the real biaxial stress state of the joint.

	Uniaxial Strain Life Equation	Uniaxial Max Shear Strain Life Equation	Biaxial Max Shear & Normal Strain Life Equation
Cycles to Failure (N$_f$)	4.6x10^3	4.9x10^3	4.7x10^3
Uniaxial/Biaxial Ratio	0.98	1.04	1

Table 5-1: Comparison of Uniaxial & Biaxial Fatigue Lives

As expected, the magnitude of the above results do not compare with the uniaxial extended fatigue test results provided at Chapter 4. The cyclic material data used in the above analysis, from Reference 33, is for aluminium alloy 2024-T3 for a crack initiation of 0.5mm. The extended fatigue tests were conducted using aluminium alloy L72 (equivalent to 2014A) and the average crack length was in the region of 3.5mm. The purpose of the above analysis was not, however, to identify the fatigue life of the material but to make a comparison in the endurance of the material under uniaxial and biaxial stress conditions. As the same cyclic material constants were used throughout the analysis and the stress conditions used are representative of the stresses experienced at the FS1045 butt joint and the stresses used in the extended fatigue tests, the above results should give a good approximation of the significance of omitting the hoop stress in the uniaxial extended fatigue tests.

6 Analysis Method for MSD

6.1 Introduction

As explained at Reference 3, Airbus, Boeing, Lockheed Martin and Delta Airlines all use different methodologies to assess Multiple Site Damage (MSD) and Multiple Element Damage (MED). They all, however, agree in the fact that MSD and its subsequent phenomenon WFD largely depend on probabilistic effects. These effects can be derived from parameters, which influence the development of MSD and WFD and, which themselves exhibit a probabilistic character. The major parameters are the initial design of a structural part, the loading, the manufacturing process and the material properties. These parameters obviously have a great influence on the fatigue life and MSD behaviour of a structure and therefore any approach to assess MSD has to consider the probabilistic effect of these parameters.

From the many research papers on MSD, such as References 9, 14, 15, 16, 19, 36 & 39, one of the most commonly used methods of assessing MSD probabilistic effects, is done by means of a Monte-Carlo Simulation. This is essentially a method in which values for uncertain variables are randomly generated over and over to simulate a particular model. The model usually consists of 2 parts; a probabilistic and a deterministic part. The probabilistic algorithm is used to determine the initial damage scenario whereas the deterministic approach is used in subsequent steps to calculate damage accumulation, crack growth and residual strength. Unfortunately, due to time restraints, this Thesis will only consider the initial damage scenario and a elementary detectable crack growth evaluation as detailed below.

6.2 Initial Damage Scenario

As explained at Reference 3, a fatigue endurance test of a structural panel containing a row of nominally identical fastener holes is analogous to testing a series of simple specimens with a single fastener hole. Each single hole specimen initiates cracking at different times, despite being manufactured to a common procedure. Similarly, multiple hole structural panels will not initiate cracks at the same time at each hole.

The initial damage scenario models therefore assume that the crack initiation time at each site susceptible to fatigue cracking is connected to the probability distribution for fatigue endurance given by testing a large number of simple specimens. A good estimate of the scatter (Standard Deviation) in the fatigue endurance of details representative of the aircraft structural feature is therefore

66

fundamental to the MSD assessment. The degree of variability in the manufacturing process originally used in the production of the component determines whether MSD will occur, since poor quality control in manufacture results in rogue flaws and the lead crack scenario, detailed at Chapter 2, of traditional damage tolerance criteria.

One of the best methods of obtaining a realistic standard deviation of fatigue data is by conducting extended fatigue tests of MSD susceptible structure from retired aircraft. Obviously this is not always a viable option and is not without its difficulties but it does eliminate a large number of the variables that could be introduced by alternative methods such as supplemental fatigue endurance tests. Such tests usually use 'new' specimens that are unlikely to be representative of the original production standard, due to process and material changes over the service life of aircraft.

As explained at Chapter 4, extended fatigue tests of specimens cut out of a RAF VC10 fuselage were used to produce the average number of cycles to crack initiation and the associated standard deviation in the results. As the FS1045 circumferential butt joint consisted of 8 and 6 consecutive columns of rivets, crack initiation data was obtained for both scenarios as detailed at Table 6-1 below. The prediction of the onset of MSD was however concentrated on the outer most row of rivets, Figure 6-1, as the bearing load in these rivets was determined to be considerably higher than the inner rivet bearing loads of the butt joint.

8 rivet specimens

specimen number	aircraft cycles	specimen cycles	total cycles	mean (cycles)	std dev (cycles)	total cycles (log cycles)	mean (log cycles)	std dev (log cycles)
5	19127	83067	102194	101534.4	23155.31	5.0094254	4.995559	0.107863
6	19127	113564	132691			5.12284147		
11	19127	88930	108057			5.03365291		
13	19127	47653	66780			4.82464641		
20	19127	83094	102221			5.00954013		
21	19127	103485	122612			5.08853298		
23	19127	89298	108425			5.03512943		
25	19127	50168	69295			4.8407019		

6 rivet specimens

specimen number	aircraft cycles	specimen cycles	total cycles	mean (cycles)	std dev (cycles)	total cycles (log cycles)	mean (log cycles)	std dev (log cycles)
12	19127	162973	182100	192036.8	48427.74	5.26030995	5.270731	0.121474
17	19127	223780	242907			5.38544003		
19	19127	167923	187050			5.27195771		
22	19127	209816	228943			5.35972737		
24	19127	100057	119184			5.07621796		

Table 6-1: Extended Fatigue Test Results
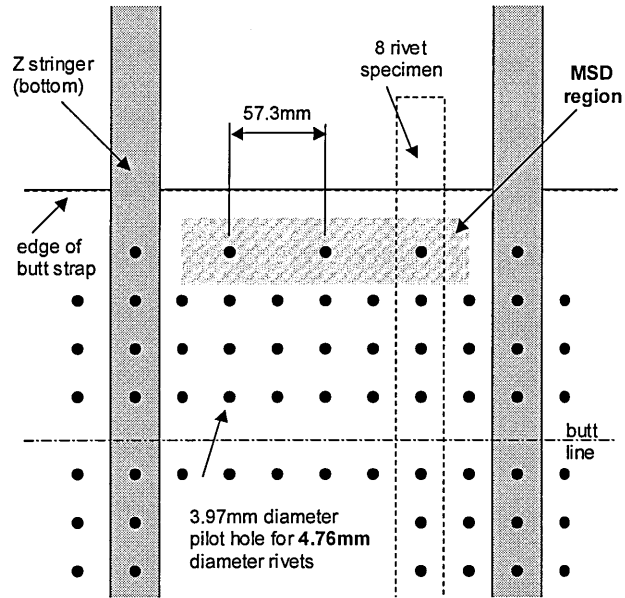
Figure 6-1: Region of FS1045 Circumferential Butt Joint MSD Evaluation

Reference 34 provides a comprehensive evaluation of the rivet load distributions in various different fuselage joints and repairs an example of which is provided at Figure 6-2 below. The theory used at Reference 34 was applied to the FS1045 circumferential butt joint, at Chapter 5, to determine the bearing stress on the outer most rivet of the joint.
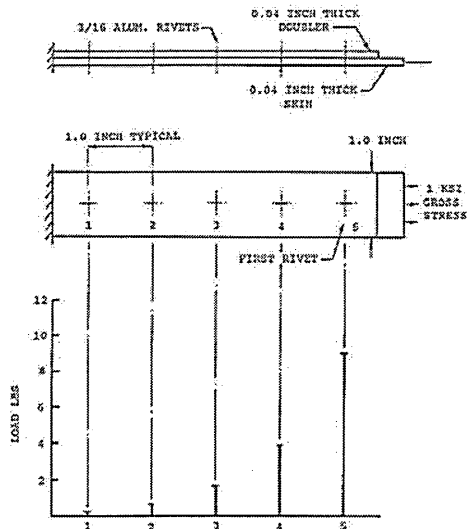
Figure 6-2: Example of Rivet Bearing Load Distribution (Reference 34)

As explained at Chapter 2, MSD will initiate in uniform stress distributions and a FEM would usually be developed to determine the stress distribution in each bay taking into consideration the presence of the relatively stiff longitudinal stringers. Unfortunately, due to the time restrictions of this Project, a FEM was not created for the stringer bay. Rivets, which were likely to be in the uniform region of the stringer bay stress distribution, as detailed at Figure 6-3 below, were therefore selected for MSD evaluation. For the outer most row of rivets there were 3 rivets per stringer bay that could be assumed to fall within the uniform stress distribution of the stringer bay. These rivets were therefore included in the MSD region that is considered in the following analysis.
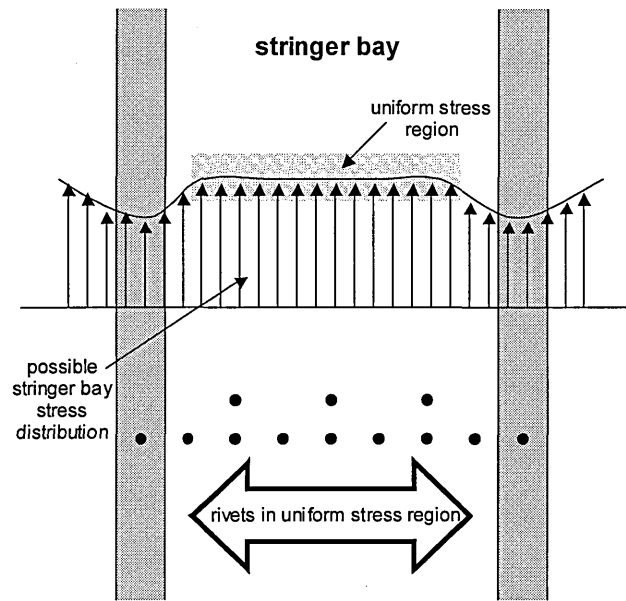
Figure 6-3: Possible FS1045 Stringer Bay Stress Distribution

To transform the individual hole fatigue endurance data detailed above to the multiple hole structure of the FS1045 butt joint the data is extrapolated in order to derive a damage scenario for multiple holes. To determine the initial damage scenario the fatigue life distribution was assumed to be a lognormal distribution. The 6 potential damage sites or Fatigue Critical Locations (FCL) in the stringer bay (generally 2 per rivet hole), identified at Figure 6-1 above, are then allocated different fatigue endurances, drawn randomly from the overall lognormal distribution of fatigue lives for the specimens. This is then considered as one MSD scenario, which was then repeated for another 399 of these 6 FCL scenarios. The average fatigue endurance and associated standard deviation of each scenario can then be determined, as detailed at Appendix D, and illustrated graphically at Figure 6-4, using a Cumulative Distribution Function (CDF).

The randomly allocated fatigue life of each FCL was performed using Gaussain random numbers as follows:

$$LogN_{FCL} = \mu[Log] + \alpha.\sigma[Log]$$

where

$LogN_{FCL}$ =   Randomly Allocated Fatigue Life of each FCL

       $\mu[Log]$ =   Mean Fatigue Life

       α =   Gaussain Random Number

       $\sigma[Log]$ =   Standard Deviation

Rearranging the above equation and taking logs, as follows, it is then possible to determine the actual number of cycles to MSD initiation of each FCL:

$$N = e^{(2.3(\mu[Log] + \alpha.\sigma[Log]))}$$

Further details of the above analysis is provided at Appendix D and results are shown graphically using a normal cumulative distribution at Figure 6-# below.

INITIATION OF MSD
(OUTER MOST RIVET ROW - 6 FCL)
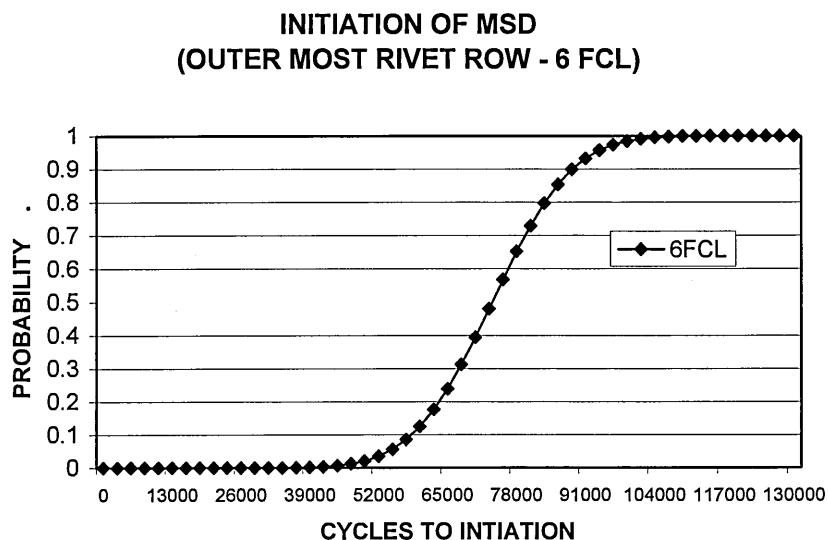
Figure 6-4: Probability of MSD Initiation
(FS1045 Butt Joint - Outer Rivet Row)

A similar procedure, for comparison, was performed for the 6 rivet specimen results but this time evaluating the initiation of MSD in the second most outer row of rivets as shown at Figure 6-5 below. In this evaluation there are, however, 14 FCLs where it is reasonable to assume a fairly uniform longitudinal stress distribution between each stringer. The results of the analysis are provided at Appendix D and illustrated at Figure 6-6 below.
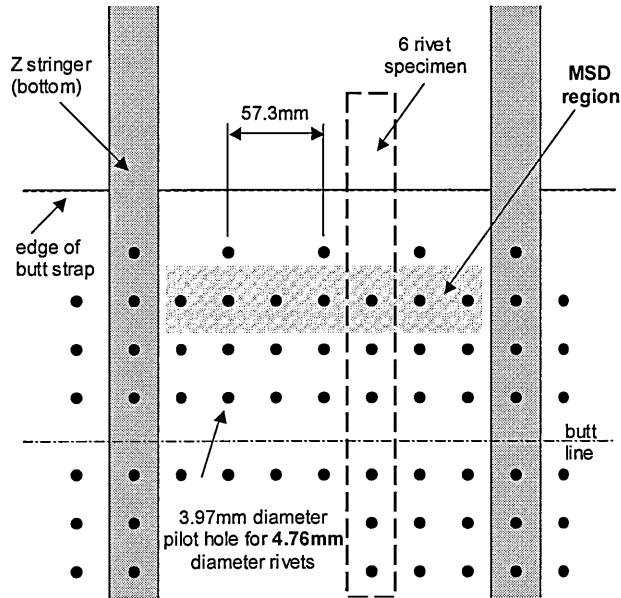
Figure 6-5: Region of MSD Evaluation (6-Rivet Specimens)
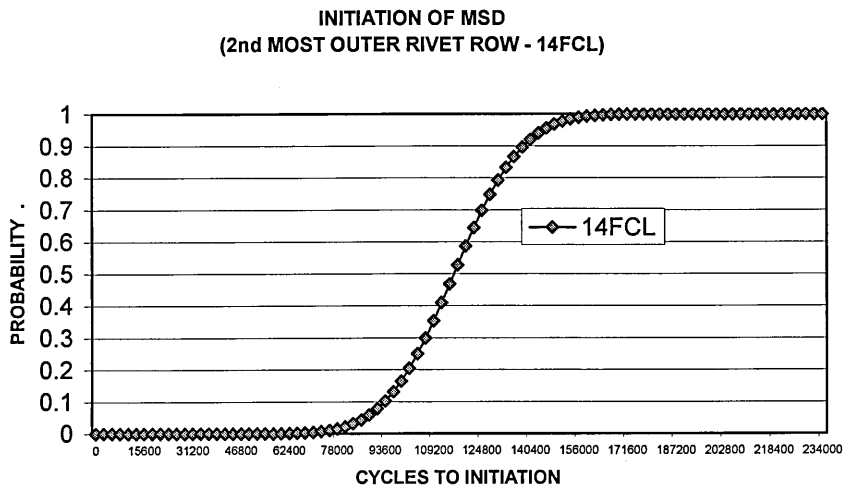
Figure 6-6: Probability of MSD Initiation
(FS1045 Butt Joint - 2nd Most Outer Rivet Row)

6.3 Detectable Crack Growth Evaluation

The next phase of the MSD assessment is to estimate the growth of each of the above initiated fatigue cracks using techniques of linear elastic fracture mechanics. Stress intensity factor solutions are used to take into the consideration the interaction of adjacent cracks and rivet holes normally using finite element analysis, boundary element methods or compounding processes. The link-up of adjacent cracks are then included within the crack growth simulation using various link-up theories, as mentioned in Chapter 2 and Reference 2, such as Plastic Zone Link-up.

The cracks are then grown to a given lead crack size or structural failure according to a residual strength criterion. This whole process would then form a single Monte-Carlo iteration, which would then be repeated many times with different randomly allocated fatigue endurances at each FCL. The final output is a failure distribution associated with the multiple hole MSD region selected. The results are generally presented graphically, as shown at Figure 6-7 below.
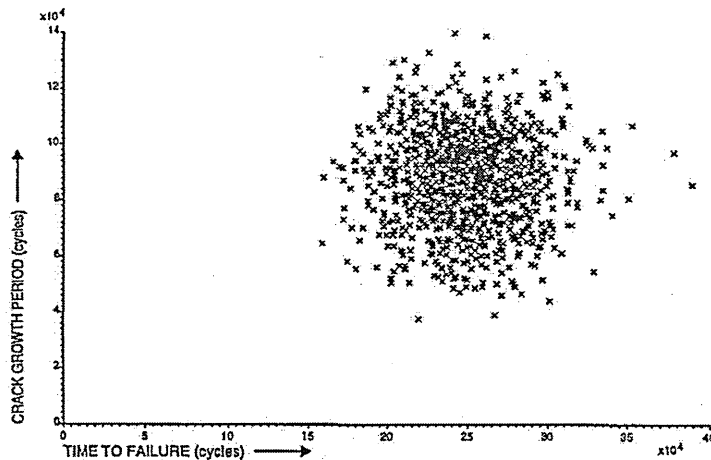
**Figure 6-7: Fatigue Endurance of Multiple Hole Configurations
(Reference 3)**

Unfortunately, the models required to simulate the interaction of adjacent cracks in each particular MSD region do take a considerable amount of time to create. The time restrictions of this Thesis therefore precluded the creation of a MSD model for the MSD regions identified above. There is, however, a considerable amount of literature available on models used for different MSD regions and the interaction of adjacent cracks. It has been suggested in some literature, such as Reference 36, that crack interaction effects are not established until the distance between adjacent crack tips is less than 50% of the rivet pitch.

The Non Destructive Inspection (NDI) Programme conducted at Reference 3 suggests that the minimum detectable crack length is 6.3mm. As the rivet pitch of the outer most row of rivets is 57.3mm, adjacent cracks will be able to grow to a length of 14.3mm, using the above 50% assumption, without being influenced by crack interaction effects (see Figure 6-8 below). As the average crack length of the extended fatigue tested specimens was 3.5mm, it was therefore decided to grow the crack 2.8 mm, using Reference 43, and include the additional fatigue cycles in the crack initiation simulation, described above, to determine the onset of detectable MSD.
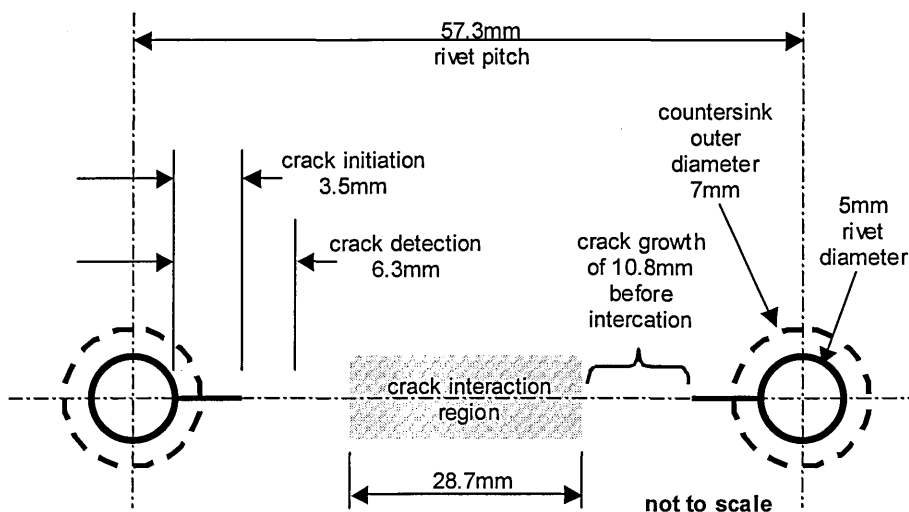
Figure 6-8: Interaction of Adjacent Cracks

The analysis performed, using Reference 43, is included at Appendix D. Various single and double crack growth scenarios were considered and it was eventually decided to include the worst-case scenario of a double 3.5mm crack. Reference 43 predicted that it would take an additional 1189 constant amplitude cycles to propagate the cracks 2.8mm so that they would be considered detectable in accordance with Reference 3.

These additional crack propagation cycles were added to the crack initiation results as detailed at Appendix D and shown graphically in the CFD below at Figure 6-9. It can, therefore, be determined from the diagram that there will be a 50% probability of detectable MSD being present in the outer rivet row of the FS1045 circumferential butt joint when the aircraft has consumed 78989 cycles. As can be seen from the current disposition of the VC10 fleet at Figure 3-3, the current fleet leader has consumed about 18000 flight cycles over nearly 40 years active service and is therefore extremely unlikely to consume 60000 flight cycles in the next 10 years. There is however a 10% probability that detectable MSD will be present in the butt joint after 59689 cycles have been consumed but this still leaves over 40000 cycles to be consumed.

INITIATION & DETECTION OF MSD
RAF VC10 FS1045 CIRCUMFERENTIAL BUTT JOINT
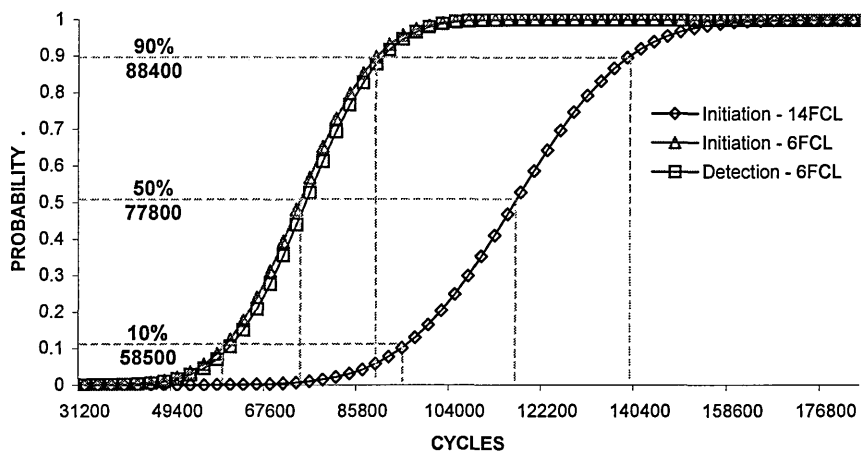
Figure 6-9: Comparison of MSD Initiation & Detection

The earliest possible predicted initiation of MSD in the FS1045 circumferential butt joint is after 32000 cycles, which, on current RAF VC10 utilisation, will take the RAF VC10 fleet leader over 45 years to achieve. From the analysis performed, the onset of MSD in the FS1045 butt joint is extremely unlikely to occur in the active fleet of RAF VC10 aircraft prior to their retirement in 2013. The analysis does however assume initiation at a crack length of 3.5mm whereas 1.25mm is normally assumed plus, as explained at Chapter 2, there are over 16 major regions of the airframe that are susceptible to MSD. The most likely regions for the earliest onset of MSD are the fuselage longitudinal lap splice joints but as explained at Reference 3 an evaluation of all MSD susceptible structural regions is required to determine which details are susceptible within the expected life of each particular aircraft type. Longitudinal lap splice joints have large regions of uniform stress distributions which, for those joints along the centre line of the aircraft, vary slightly from flight to flight as they are dominated by fuselage pressurisation hoop stresses.

Circumferential butt joints at the crown of the fuselage are, however, especially for T-tail rear engine aircraft (such as the VC10), dominated by fuselage bending stresses, which vary considerably depending on numerous factors and the largest of which are localised to the crown of the fuselage (further point from the neutral axis). There are, therefore, other areas of the VC10 fuselage that are likely to be more susceptible to MSD than the FS1045 circumferential butt joint, which should be evaluated to determine susceptibility.

74

7 Discussion and Conclusion

7.1 Introduction

This Chapter analyses the results of the RAF VC10 circumferential butt joint extended fatigue tests, the biaxial fatigue evaluation and the MSD analysis with the findings of other similar research to validate the assumptions made. The discussion starts by considering the test results and then progresses to take into consideration other factors that influence the prediction of the onset of MSD. The discussions are then summarised in the conclusion at the end of the Chapter.

7.2 Discussion

7.2.1 Specimen Results

Fatigue Endurance

The results of the extended fatigue tests at Chapter 4, identified that there is a significant difference in the fatigue endurance of the 8 and 6 rivet specimens at each respective test load. The majority of the tests were conducted at a constant amplitude maximum load of 3.0KN and a stress ratio (R) of 0.212. This was an actual in-service RAF VC10 cycle load obtained from the in-service stress spectrum of an Operation Loads Measurement (OLM) Programme which included the instrumentation of FS1045 at the crown of the fuselage as detailed at Chapter 3 and Appendix A. The average fatigue endurance of the 8 rivet specimens, at the above test load, was approximately 102000 cycles whereas the 6 rivet specimens, at the same load, had an average fatigue endurance that was nearly twice that of the 8 rivet specimens at 192000 cycles.

As explained at Chapter 5 and Reference 34, the outer most row of rivets in a joint or repair experience the greatest rivet bearing loads and are therefore subjected to most fatigue damage. This phenomenon was extensively investigated at Reference 34 where the rivet load distribution of a simple riveted doubler repair (Figure 7-1) was analysed by simulating each rivet as an elastic spring under shear load and each portion of the skin and doubler repair as a bar. The resulting load distribution of each rivet in the idealised strip (identified in Figure 7-1) of the doubler repair is shown at Figure 7-1 below.
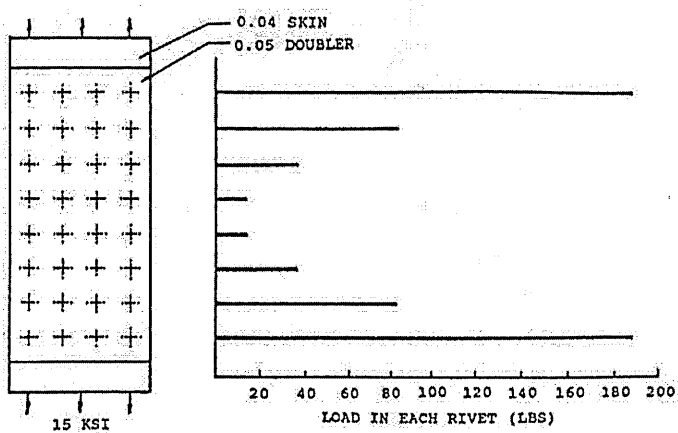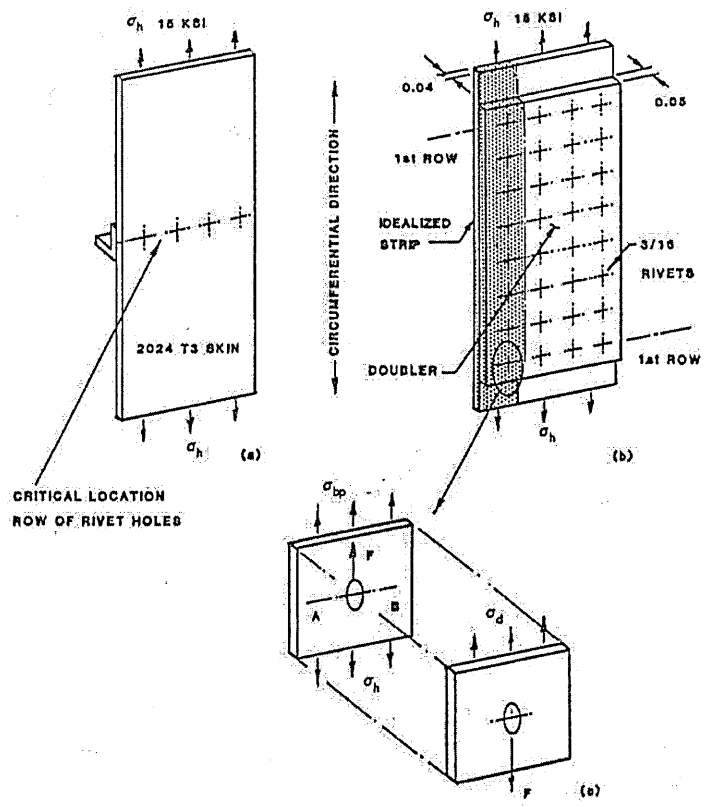
Figure 7-1: Doubler Repair – Rivet Load Distribution (Reference 34)

It was determined at Reference 34, and as depicted at Figure 7-1, that the highest loads were at the first row of rivets and the ratio of the skin bearing stress at the first row of rivets over the gross applied stress was 1.6. A similar calculation can be performed for the second row of rivets and the ratio of bearing stress to gross stress in this case was determined to be 0.7. The S-N Chart for the material used in the above example with various different bearing and gross stress ratios is provided at Figure 7-2 below. It can be determined,

from the chart, that the fatigue life of the first row of rivets (gross stress of approximately 100MPa) was 53800 cycles and the second row with bearing to gross stress ration of 0.7 would have a fatigue life of 90000 cycles. The fatigue life of the second row of rivets is approximately twice the fatigue life of the first row of rivets.
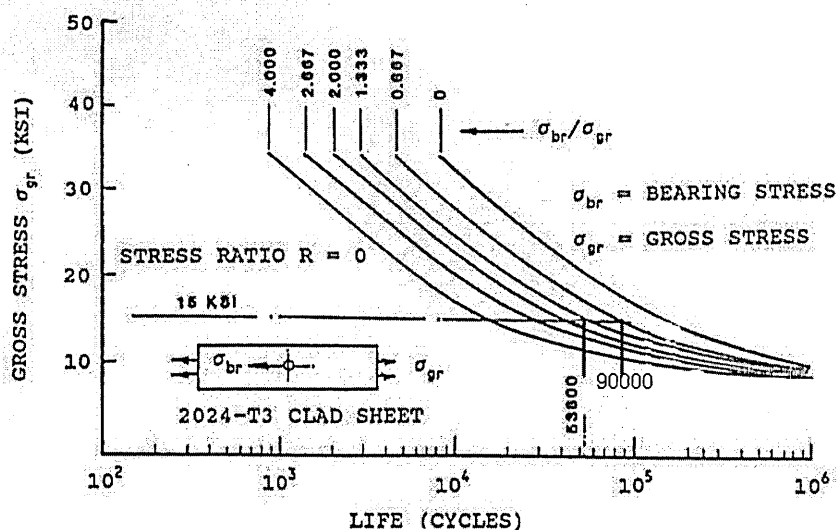
Figure 7-2: S-N Chart (2024-T3) Open Hole (Reference 34)

There was insufficient time in which to construct a FEM to establish whether or not the load distribution of the FS1045 butt joint was similar to the example given above. The transfer of load between the fuselage skins, the rivets and the butt strap would, however, be very similar to the doubler example above. The fatigue life of the 8 rivet specimens would represent the fatigue life of the outer most row of rivet holes and the 6 rivet specimens represent the fatigue life of the second most outer row of rivet holes. It is therefore reasonable to assume that the skin bearing stress at the outer row of rivets is at least twice the skin bearing stress at the second most outer row of rivets. The overall fatigue life of the second most outer row of rivet holes is therefore nearly twice the fatigue life of the outer most rivet holes despite the fact that it is intuitive to think that the overall load distribution of the 8 rivet specimens would be less and would therefore have a longer fatigue life than the 6 rivet specimens.

The findings of Reference 34 are further reinforced by the research conducted at Reference 18. An instrumented Boeing 737 longitudinal fuselage lap joint was subjected to ground pressurisation to determine the strains at various locations on the joint and the fuselage (Figure 7-3). It was concluded that most of the load in the skin above the lap joint was transferred into the skin around the upper rivet row. It was also noted that the strain levels in the upper skin of the joint decrease dramatically in the circumferential direction across the joint.

The skin around the middle rivet row exhibited only a fraction of the strain measured at the upper rivet row; the lower rivet row experienced even less strain. It was, however, noted that the lower rivet row of the inner skin experiences the same peak strains as the upper rivet row of the outer skin as shown in Figure 7-4.
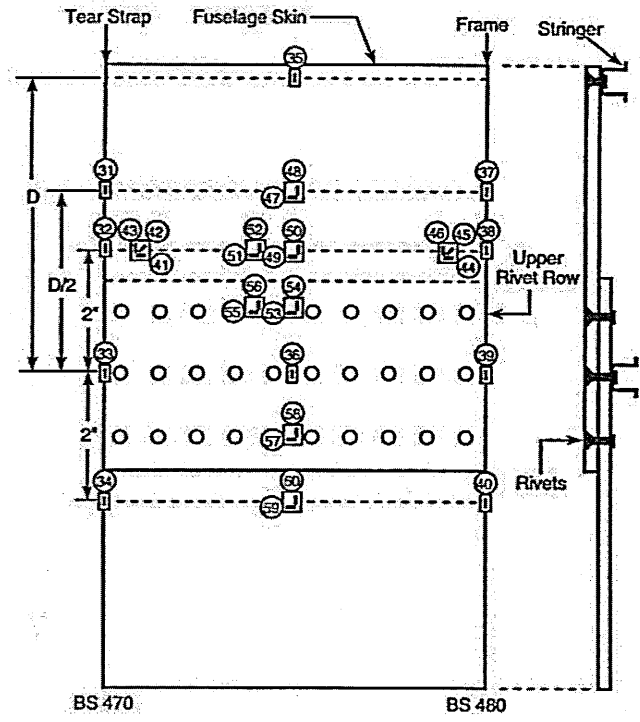
Figure 7-3: Boeing 737 Lap Joint (Reference 18)
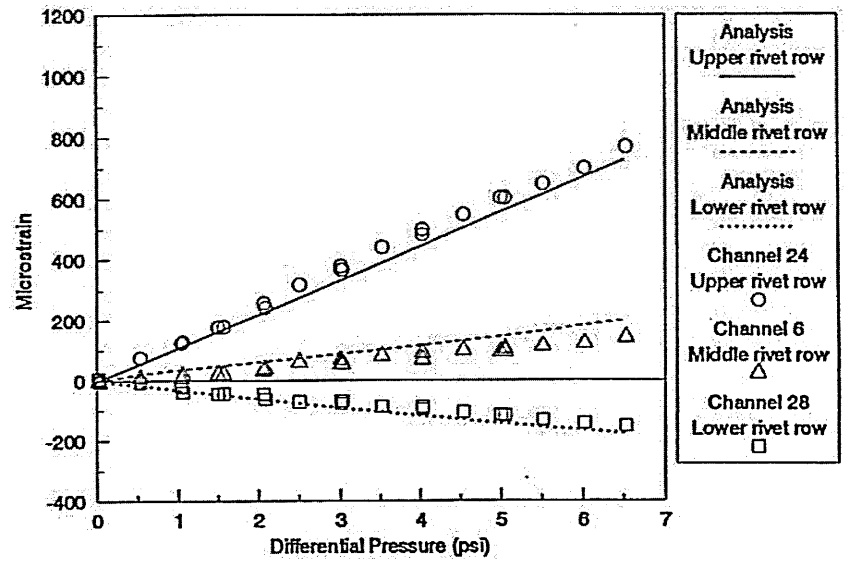
Figure 7-4: Comparison of Strains Across Lap Joint (Reference 18)

Although the above examples are not exactly representative of the FS1045 Butt Joint, the transfer of load between the fuselage skins, the rivets and the butt strap will be very similar and the outer most row of rivets (forward and aft in the case of the circumferential joint) will be subjected to highest skin bearing loads in the joint and will therefore be the first region in the joint to develop MSD.

Standard Deviation

Since the Aloha Accident a significant amount of fatigue tests have been performed on various airframe joints from simple lap joint specimens to full-scale structural tests. The tests identified that there are large differences in the fatigue lives of each joint. Reference 9 suggests that the cause for the scatter can be related to the following items:

     a.   Material.

     b.   Size and Surface Effects.

     c.   Manufacturing (including rivet squeeze forces).

     d.   Clamped Assembly Stresses.

     e.   Loading Conditions (including biaxial loading of full-scale structure not included in specimen tests).

     f.   Fretting.

     g.   Environmental Effects.

It was therefore slightly surprising to see that results produced at Chapter 4 only identified a small amount of scatter in the results of both the 8 rivet and 6 rivet specimens. Most of the research papers available give test results for specially manufactured specimens using pristine materials that have not been subjected to environmental and operational degradation. Extended fatigue testing of retired aircraft specimens allows consideration to be given to a whole spectrum of uncertainties such as manufacturing tolerances, operational usage, accidental and environmental damage. It was therefore somewhat of a surprise to notice that in comparison to pristine specimens the scatter of the retired aircraft specimen tests where considerably less.

There was also a significant difference in the standard deviation between the 8 Rivet and 6 Rivet specimens. There were, however, only five 6-Rivet specimens tested at a maximum load of 3KN (R=0.2) in comparison to eight 8-Rivet specimens. Ideally, a greater number of both 8 & 6-Rivet specimens would be tested (majority of research papers test at least 30 specimens) to provide greater confidence in the results and the scatter produced.

Specimen Type	Mean Fatigue Life (Cycles)	Standard Deviation (Log)
8 Rivet (Retired VC10 Circumferential Joint)	102 000	0.108
6 Rivet (Retired VC10 Circumferential Joint)	192 000	0.122
4 Rivet (Pristine A300 Circumferential Joint)	126 000	0.157

Table 7-1: Fatigue Life & Standard Deviation Comparison

It is difficult to draw any exact comparisons between retired and pristine specimens without actually manufacturing pristine examples of the specimens tested at Chapter 4. Even then the results would be compromised because it would be extremely difficult to duplicate the original material and manufacturing quality of the butt joint. Reference 15, however, provides test results of 30 small specimens manufactured to simulate the crack initiation process of an A300 circumferential joint. The average results of the tests along with the standard deviation in the results are provided at Table 7-1 along with averages given at Chapter 4.

There is an appreciable reduction in standard deviation of the fatigue lives of the retired aircraft specimens, which seems to suggest that as aircraft age the standard deviation of the fatigue life reduces. From the list of the main causes for scatter given above the main variable effecting retired aircraft specimens tests (in comparison to pristine specimens), apart from the biaxial loading considerations discussed later in this Chapter, is environmental (and operational) degradation. The presence of corrosion (discussed later in this Chapter) could be reducing the effect of the other scatter variables and thereby reducing the overall standard deviation in the fatigue life of the joint. Obviously this would have a dramatic impact on the prediction of MSD and further tests would be necessary to substantiate the above rudimentary findings.

Geometry Variations

As explained at Chapter 2, since the Aloha Accident there has been a considerable amount of research into determining the onset of MSD but there has also been a significant amount of research into designing fuselage joints to improve their fatigue endurance. Reference 9 includes a significant amount of research into the variables that influence the fatigue lives of riveted joints and identifies some of the geometric variables that can significantly affect the stress concentration in a joint as illustrated at Figure 7-5 below.
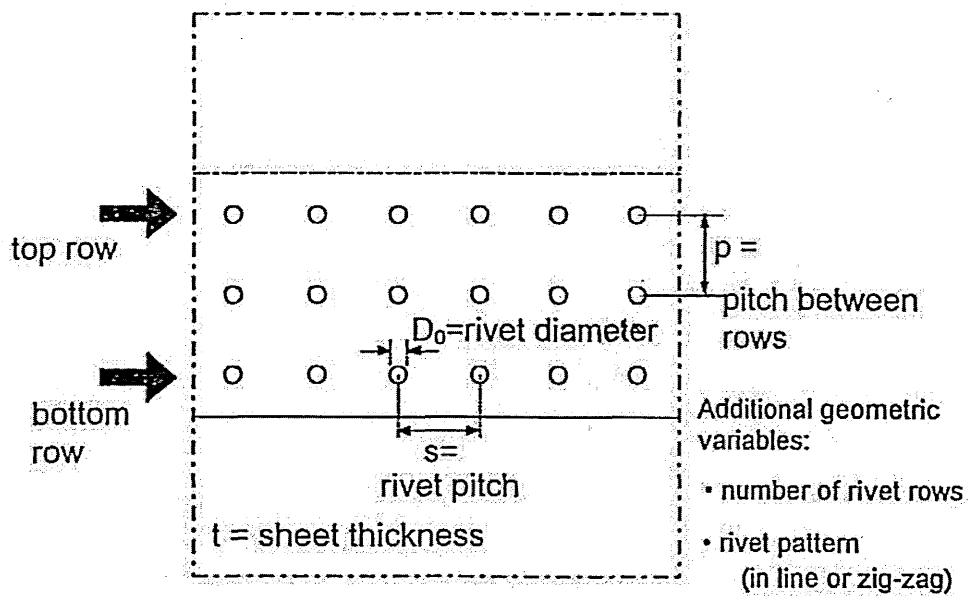
Figure 7-5: Fuselage Joint Geometric Variables (Reference 9)

Obviously, for retired aircraft specimens these variables are fixed but the research conducted at Reference 9 looks at each variable in more detail and in particular the influence of rivet geometry on fatigue life. It was found, at Reference 9, that the dimensions of the driven end of the rivet, as shown at Figure 7-6, had a direct relationship with the squeeze force applied to the rivet as shown at Figure 7-7.
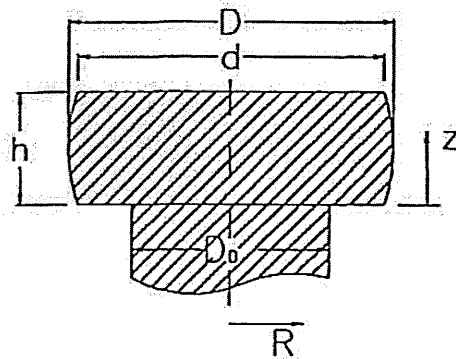
Figure 7-6: Rivet Dimensions (Reference 9)

81
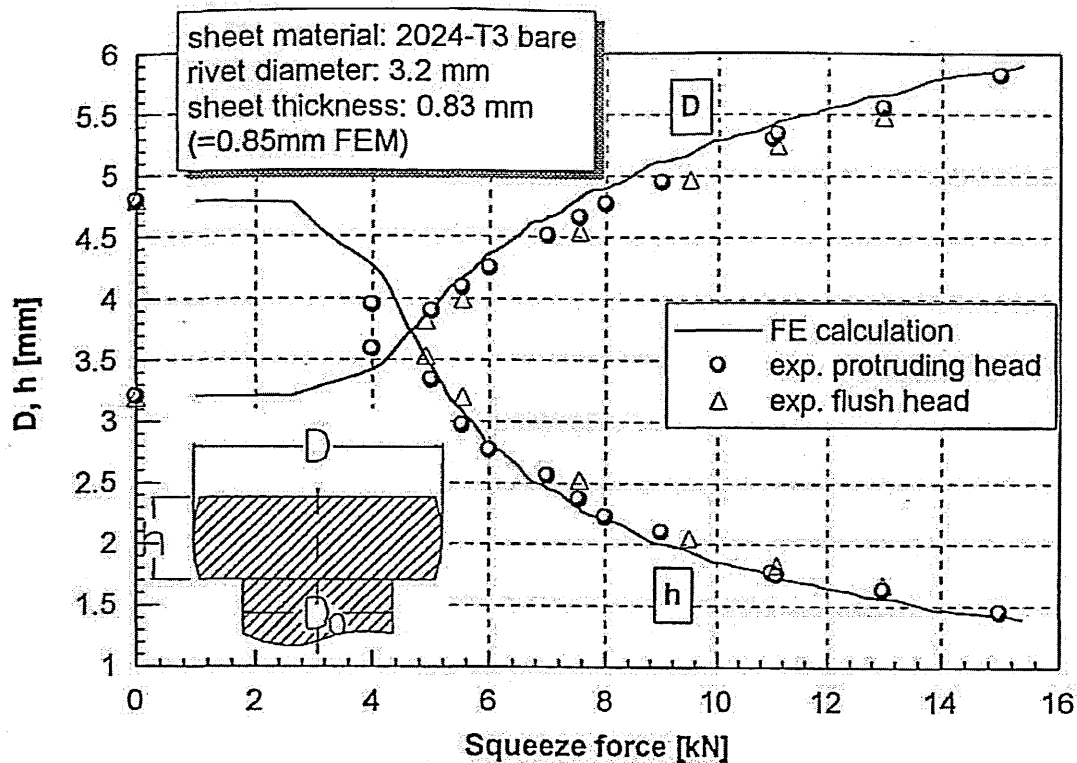
Figure 7-7: Relationship Between Rivet Head Dimensions & Squeeze Force (Reference 9)

As would be expected, for the same pre-driven rivet length, a higher squeeze force is required to reduce the (h) dimension and increase the (D) dimension of the driven rivet head. Figure 7-7 illustrates, however, that the relationship between the squeeze force and driven head dimensions is not linear due to strain hardening of the rivet material and an increasing resistance of the sheet material to hole expansion. This work done at Reference has now be taken even further by Cranfield University (by the author of Reference 36) to determine what effect the squeeze force has on the fatigue life of the rivet hole. The work is still being researched but initial findings show that a higher squeeze force relates to a longer fatigue life.

No precise measurements of the driven rivet heads of the RAF VC10 specimens were taken but comparisons, between specimens tested at the same constant amplitude loads, were made. Table 7-2 is a list of the 8 Rivet specimens, and their respective test fatigue lives, in order of largest (D) and smallest (h) driven rivet head dimensions (at the failed hole). It can be deduced from the work done at Reference 9 that, assuming the pre-driven length of the rivets were the same, the squeeze force applied to the Specimen#6 (with the largest D and smallest h dimension) was greater than the squeeze force applied to Specimen#8. The respective fatigue lives of the specimens do correlate with the initial findings of the research being conducted by the author of Reference 36 (apart from Specimen#5 & Specimen#6 which were indistinguishable) in that a higher squeeze force relates to a higher rivet hole fatigue life.

In Order of Highest Squeeze Force Largest (D) & Smallest (h) (@ Failed rivet hole)	Specimen #	Fatigue Life (Cycles)
1	6	113564
2	21	103485
3	23	89298
4	11	88930
5	5	83067
6	20	83094
7	25	50168
8	13	47653

Table 7-2: 8-Rivet Specimens - Squeeze Force V Fatigue Life

Other findings at Reference 8 & 9 identified that the fatigue initiation life of the rivet hole can be related to the quality of the riveting operation as proper rivet swelling can provide beneficial residual compressive stresses at the hole boundary. It was found, however, that to obtain substantial interference the rivet must be driven squarely to produce a rivet head similar to Figure 7-6 above. If the rivets do not properly fill the hole after being driven then poor fatigue quality can be expected. When rivets are not driven squarely it results in a 'clinched' installation as illustrated at Figure 7-8 below. As detailed at Chapter 4, some of the specimens were observed to have moderately clinched rivets. When clinching occurs the hole is not properly filled and the intended rivet swelling does not occur. The beneficial residual compressive stresses are therefore not present thereby reducing the fatigue endurance of the rivet hole.
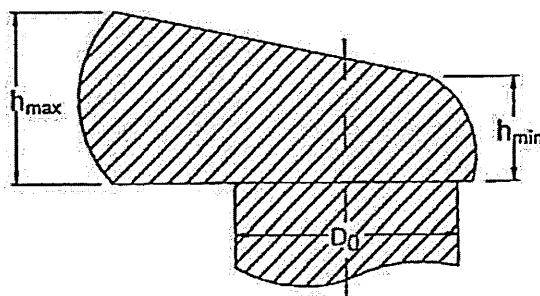
Figure 7-8: Deformed Rivet Head (Reference 9)

Severe rivet clinching, as shown at Figure 7-9 below, can cause a situation where there may be a gap between the hole boundary and the rivet wall which will allow some free boundary displacement. When this occurs the fatigue life of the rivet hole will be more representative of an open hole. None of the outer most rivets of all the specimens tested exhibited any signs of severe clinching.
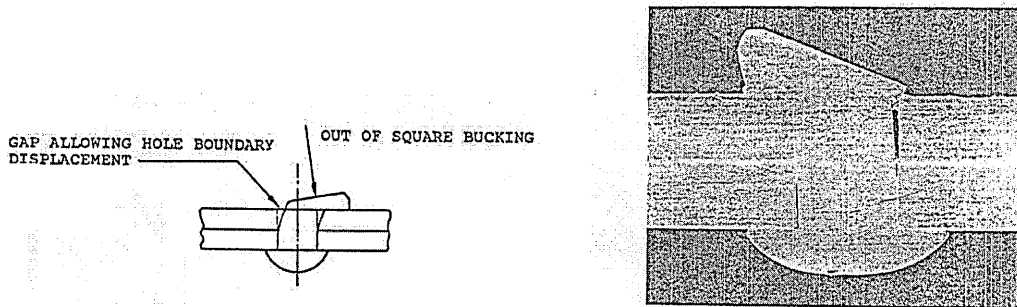
Figure 7-9: Example of Rivet Clinching (Reference 8)

As explained above and at Chapter 4 some of the specimens did exhibit moderate clinching with a difference of 1mm between h_{max} and h_{min} (Specimen#1). Overall the rivet quality, especially the outer most rivets, was fairly consistent. The only poor quality rivet was found on Specimen#20, as shown at Figure 7-10 below, which in this case was the second most outer rivet.
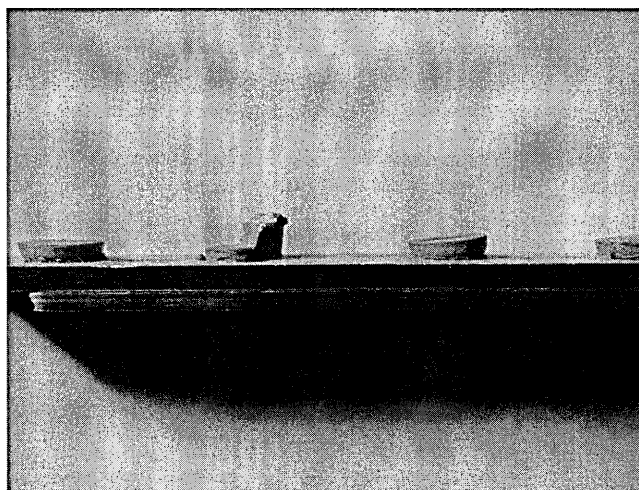
Figure 7-10: A Poor Quality Rivet - Specimen#20

Location.

The results provided at Chapter 4 were examined to determine whether or not there was a correlation between the locations of each specimen and their respective fatigue lives. With a fuselage radius of 74 inches (1.88m) there was approximately a 20cm difference in the distance from the centre of the fuselage crown (Specimen#13) to the neutral axis and the distance from the location of stringer#3 (Specimen#1 or Specimen#25). The longitudinal bending stresses experienced by Specimen#1 and Specimen#25 would therefore be less than

the stresses experienced at Specimen#13 and consequently the specimens furthest from the centre line would have experienced less fatigue damage and would therefore have a greater fatigue endurance post the extended fatigue tests. The results at Chapter 4 are, however, inconclusive and no correlation between specimen location and fatigue endurance could be found.

Corrosion.

The fracture surface analysis performed at Appendix B identifies that all of the specimens tested had evidence of defects at the extreme point of the countersink. The scanning electron microscope images of the 6 selected specimens, Appendix B, all had evidence of corrosion and pre-existing fatigue cracks less than 50×10^{-6}m in length. It is expected that the presence of such defects contributed to the fatigue endurance of the specimens but also influenced the standard deviation in the results, as explained above. No previous research could be discovered to substantiate this hypothesis but the comparison made with pristine samples above suggests that the effect of environmental degradation should be taken into consideration when trying to predict the onset of MSD in the susceptible structure aircraft. Further research duplicating the extended fatigue specimen tests using pristine material, acknowledge the fact that material and manufacturing standards will be different to the original specimens, would help to quantify the above findings.

7.2.2 Specimen Loading

Uniaxial & Biaxial Considerations

The analysis performed at Chapter 5 identified that as the local longitudinal bending stresses at the outer most rivet hole of the butt joint was nearly 7 times greater than the local circumferential hoop stresses the longitudinal stresses dominated the fatigue life the outer hole. The difference in the fatigue endurance of the outer most rivet hole between the biaxial longitudinal and hoop stress state and solely the longitudinal stress state were determined, using modified uniaxial strain life equations as detailed at Chapter 5, to be negligible (Table 5-1).

Further work would be required to determine the ratio of local longitudinal to circumferential stresses that would identify that both stresses would need to be considered to determine the correct fatigue life of the rivet hole. The design of the VC10, with a large T-tail and rear engine configuration, will produce large bending stresses in the fuselage in comparison to aircraft with wing-mounted engines. Although not a direct comparison, the results of the instrumented Boeing 737 fuselage pressure tests identify the differences in longitudinal and circumferential stresses at various locations around the fuselage. There are no measurements for the crown of the fuselage but highest located strain gauge (Channel 48 in Table 7-3 below) identifies a ratio of longitudinal to Hoop stress of 0.503 compared to the VC10 FS1045 crown ratio of 1.6.

Test Section Location	Measured Strain (μinch/inch)			Calculated Stress (ksi)		
	ε_θ	ε_z	$\varepsilon_z / \varepsilon_\theta$	σ_θ	σ_z	σ_z / σ_θ
S-4L, BS475 (Channels 17 and 18)	825 (0.776)	189 (0.875)	0.229	9.7 (0.724)	4.8 (0.716)	0.495
S-10L, BS475 (Channels 47 and 48)	931 (0.876)	222 (1.028)	0.238	11.0 (0.821)	5.5 (0.821)	0.503
S-14L, BS475 (Channels 61 and 62)	929 (0.874)	190 (0.880)	0.205	10.8 (0.806)	5.2 (0.776)	0.475
S-4L, BS785 (Channels 83 and 84)	948 (0.892)	266 (1.231)	0.281	11.3 (0.843)	6.0 (0.896)	0.536
S-10L, BS785 (Channels 91 and 92)	961 (0.904)	225 (1.042)	0.234	11.3 (0.843)	5.6 (0.836)	0.499

Table 7-3: Boeing 737 Fuselage Strains & Stresses (Reference 18)

It is therefore reasonable to assume that the VC10 does experience significantly larger fuselage bending stresses than the more conventional wing-mounted engine airliners. The biaxial fatigue analysis performed at Chapter 5 identifies that for the VC10 these bending stresses influence the fatigue life of the rivet holes at the crown of the fuselage. The uniaxial extended fatigue tests were, therefore, performed using the bending stresses obtained from the instrumentation of the crown of an in-service RAF VC10 aircraft at FS1045. The analysis therefore suggests that the loading conditions of the specimens should be similar to that experienced in the full-scale fuselage.

There is, however, evidence that this may not be the case. Firstly, the scanning electron microscope images, Appendix B, identify there is a difference in the crack propagation of pre-existing cracks and the crack propagation initiated during the uniaxial fatigue test. There was also evidence of cracks forming on different planes, which has been observed in similar tests, such as Reference 38 and Reference 39. Here the cause was attributable to fretting as the multiple fatigue fracture surface planes originated from the side of the specimen joint's faying surfaces. The FS1045 butt joint has sealant between the two faying surfaces and consequently no fretting was observed and the multiple fatigue fracture surface planes all originated from the region of the countersink. Secondly, the biaxial fatigue analysis does not take into consideration the effects of secondary bending (discussed later in this Chapter), which was observed during the testing of the specimens.

Secondary Bending

Due to the different thickness materials used in the construction of the FS1045 butt joint, as shown at Chapter 4, the neutral axis of the skins and the butt strap

is not a straight line coinciding with the line of the applied load. There are therefore eccentricities in the neutral line, which cause out-of-plane displacements and sheet bending occurs as was observed during the extended fatigue specimen tests. This bending is referred to as secondary bending and the research conducted at Reference 9 identified that it contributes to an increased stress concentration at the end rows of a riveted joint which significantly reduces the fatigue endurance of the joint as illustrated at Figure 7-11 below.
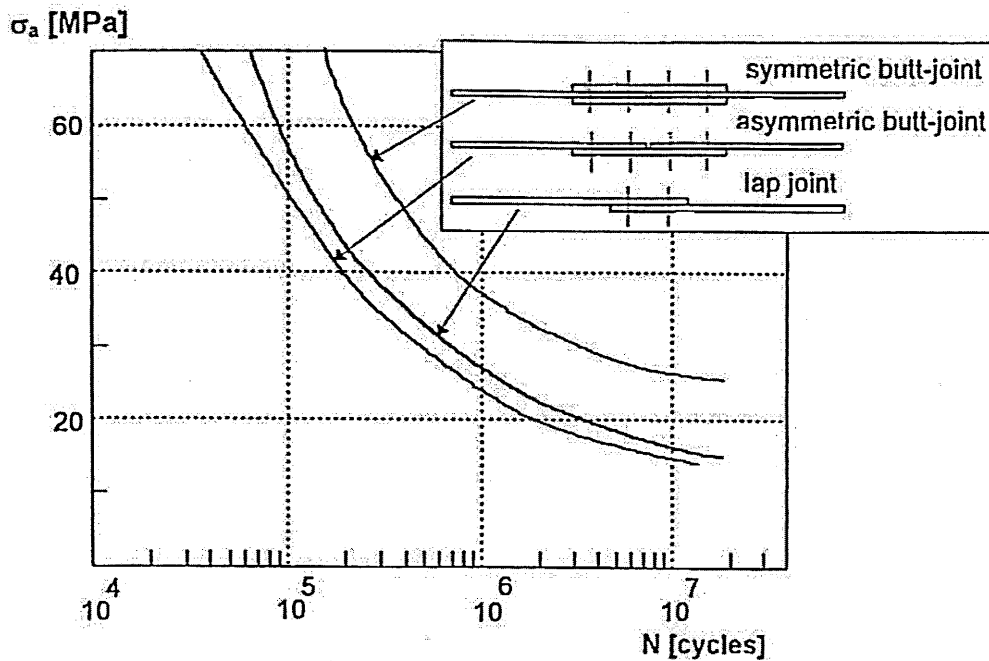
Figure 7-11: S-N Chart of Different Rivet Joints (Reference 8)

The tests, at Reference 9, were conducted on specimens, which did not take into consideration the effect that the fuselage curvature would have on secondary bending and subsequently the fatigue life of the joint. The work done, at Reference 19, using the Full-Scale Aircraft Structural Test Evaluation and Research (FASTER) facility at FAA William J Hughes Technical Centre, however, identifies that local bending is significant and greater than that predicted using FE analysis. High out-of-plane bending along the outer most rivet row of the fuselage panel lap joint tested (Figure 7-12) caused the skin to push up against the rivet heads to form the cracks as illustrated at Figure 7-13 below.
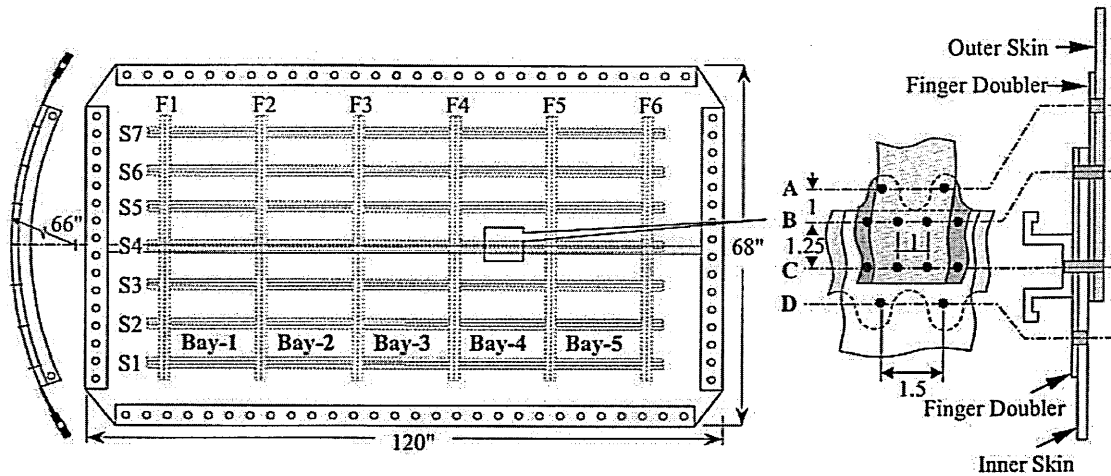
Figure 7-12: FASTER Test Panel (Reference 19)
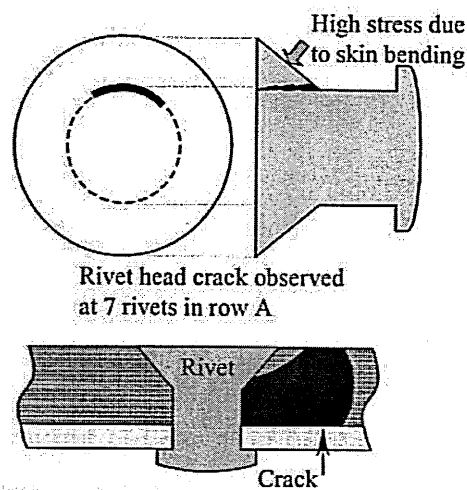
Figure 7-13: Failure Mode Along Outer Most Rivet Row of Lap Joint (Reference 19)

Although the above test in for a lap joint rather than a butt joint, most lap joint specimen research does not experience or consider this mode of failure and it is therefore reasonable to assume that the effect of fuselage curvature prevents out-of-plane displacements and increases the amount of out-of-plane bending stresses at the outer most row of rivets. No rivet head cracking was observed during the extended fatigue testing of the FS1045 butt joint specimens but, as with most specimen tests, the edges are not constrained and the specimen is free to move out-of-plane. Further research would need to be conducted to determine the failure mode and the effect on the fatigue life on the specimens if they were restricted from moving out-of-plane.

Constant & Variable Amplitude Considerations

The initial intention was to test some specimens using the longitudinal stress spectrum, at Appendix A, obtained from an instrumented in-service RAF VC10

aircraft and compare the fatigue life of the specimens to constant amplitude tests at different loads to determine which constant amplitude cycle represented the spectrum loading of the joint the best. Unfortunately, there was insufficient time in which to test the specimens using the spectrum so a cycle load from the spectrum (maximum load of 3KN, stress ratio of R=0.2) was used to perform constant amplitude extended fatigue tests of the specimens.

It is therefore unknown whether or not the selected constant amplitude load is representative of the fatigue damage that would be incurred during an average RAF VC10 flight using the spectrum at Appendix A. With insufficient time in which to determine the effects that crack closure, using the variable amplitude spectrum, would have on the fatigue life of the specimens it was assumed that the constant amplitude load used represented the overall fatigue damage incurred during an average flight. Further work would be required to determine the difference in the fatigue damage incurred between the variable amplitude spectrum and the constant amplitude cycle used. As the effect of crack closure, however, has not been taken into consideration the constant amplitude cycle load should be more severe than the variable amplitude spectrum and the results should therefore be the worst case and more pessimistic than if the variable amplitude spectrum was used.

Some research has been conducted, Reference 31 and Reference 34, into determining the difference in fatigue endurance due to spectrum and constant amplitude applied loads. Reference 34 identifies a method of representing a spectrum as a single cycle to produce the same crack growth rates, which, if applied to the tests, would give more confidence in the fatigue life of the specimens produced. The research done at Reference 31, however, suggests that despite the differences in fatigue endurance there will also be a significant difference in the amount of scatter with spectrum loads reducing the amount of scatter in the results produced by comparable single cycle loads. There is obviously further work required to ensure that the constant amplitude loads used in extended fatigue testing of specimens is realistic in both terms of fatigue endurance and scatter.

7.2.3 MSD Analysis

Stress Distribution. As there was insufficient time in which to construct a FEM of the stringer bay, the stress distribution had to be assumed as detailed at Chapter 6. There has, however, been a considerable amount of research in determining the stress distributions between fuselage frames and stringers. An example of which was conducted at Reference 9 where the rivet load distribution of a uniaxially loaded lap joint using a 3D FEM was determined as shown at Figure 7-14 and Figure 7-15 below.
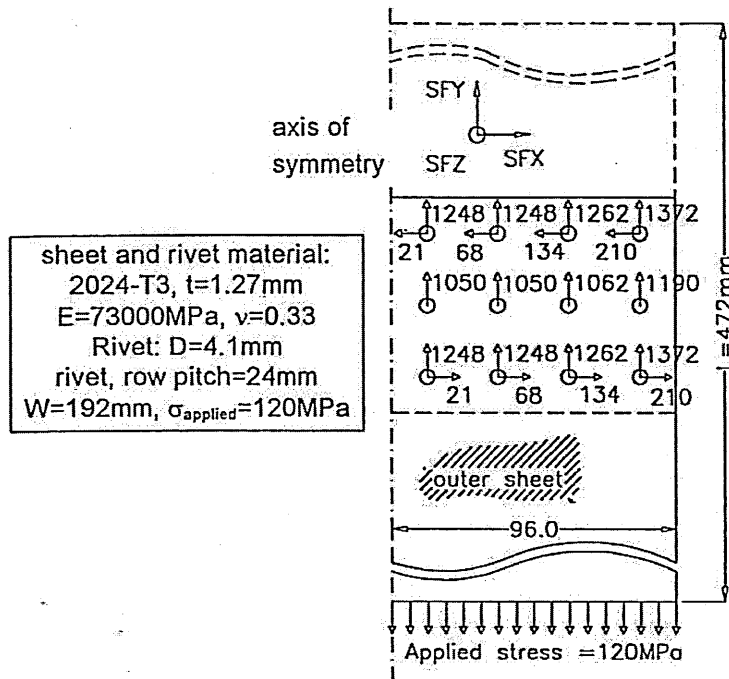
Figure 7-14: Uniaxially Loaded Lap Joint - Rivet Forces (Reference 9)
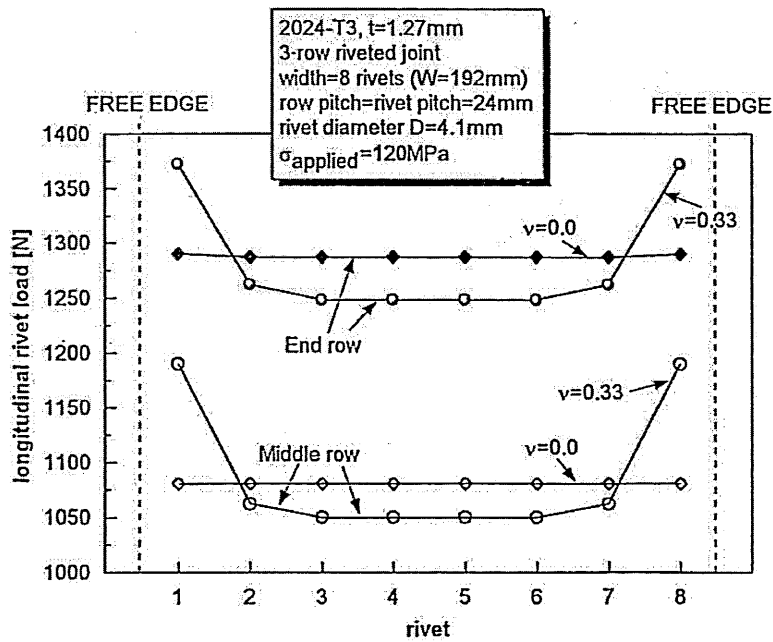
Figure 7-15: Rivet Load Distribution – 8 Rivet Row Lap Joint (Reference 9)

The load distribution away from the edges of the panel can be assumed to be uniform and is therefore the region susceptible to MSD. No FEM was produced of the FS1045 butt joint, but the above findings were applied to stress distribution as detailed at Chapter 6. The above FEM does however assume

the joint is uniaxially loaded and although the analysis performed at Chapter 5 suggests that the longitudinal stresses dominant the fatigue endurance of the FS1045 butt joint a FEM of the panel and the biaxial loads would help to substantiate the stress distribution and the local bearing stresses.

Fatigue Critical Locations (FCLs). The MSD analysis assumed that each rivet hole would have 2 fatigue critical locations at the 3 and 9 O'clock positions with the 12 and 6 O'clock positions being the direction of the longitudinal loads. This assumption is substantiated by the in-service findings, Reference 10, of Boeing 737 lap joints and the research conducted using the Full-Scale Aircraft Structural Test Evaluation and Research (FASTER) facility, Reference 19.

Reference 19 does, however, identify additional cracks in the head of the rivets caused by out-of-planes stresses discussed above. The research at Reference 10 also identifies that MSD initiation is most likely to occur at the centre of the bay being evaluated and crack initiation is not as random as that simulated using Monte Carlo prediction methods.

Random Scenarios. The analysis performed at Chapter 6 assumed 400 Monte Carlo simulations of the 6 FCLs scenario. The research conducted at Cranfield University, by the author of Reference 36, identifies that for Monte-Carlo simulations 400 random scenarios represents a good compromise between execution time and accuracy of the results as convergence in the results were obtained by around 350 simulations.
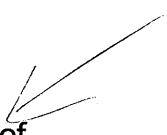
7.2.4 MSD Susceptible Detail

As explained at Chapter 2, the Circumferential Butt Joint at the crown of the fuselage has not been subjected to the same amount of research as the longitudinal lap splice joint. All MSD susceptible structure have regions of uniform stress and the lap splice has very large regions where the stress is uniform thereby increasing the likelihood of MSD. Conversely, the crown of the fuselage will have a much smaller region of uniform stress, as the bending stresses will be a maximum at the furthest point away from the neutral axis of the aircraft. It is therefore much more likely for MSD to be prevalent in longitudinal fuselage joints subjected to larger regions of uniform stress distributions. Chapter 2 also identifies 16 major regions of the airframe that are susceptible to either MSD or MED and it is important in any MSD evaluation to determine which area is most susceptible to MSD within the aircraft's DSG. This will require an evaluation of all susceptible areas, the most vulnerable of which would then be used to determine the point of WFD beyond which the aircraft may not be operated without further evaluation.

7.3 Conclusion

The MSD analysis performed identifies that, at current RAF VC10 operational usage rates, it is extremely unlikely for MSD to initiate in the FS1045 Circumferential Butt Joint, at the crown of the fuselage, prior to its retirement in 2013. The analysis also identified that the longitudinal bending stresses at FS1045 where the prevalent stresses in determining the fatigue endurance of joint. The local longitudinal bearing skin stresses in the outer row rivets of the joint being almost 7 times greater than the local circumferential hoop stresses. Despite the dominance of the longitudinal stresses, micrographs of the fracture surfaces of the extended fatigue test specimens suggested that the uniaxial applied load was not consistent with the loads experienced in the fuselage. These observations, however, could be attributable to not duplicating the out-of-plane stresses produced by secondary bending of the asymmetric butt joint in the fuselage as the specimens were tested without any out-of-plane displacement restrictions. All the specimens exhibited small (50×10^{-6} m) pre-existing cracks and corrosion pits which, in comparison to 'similar' pristine specimens, suggests that environmental and operational degradation contributes to reducing fatigue endurance and the standard deviation in the results. Further research is required to substantiate these rudimentary findings but if substantiated would have a dramatic effect on the prediction of MSD in aircraft structure. Although MSD is highly unlikely to occur in the FS1045 butt joint, research into WFD has identified that there are over 16 major regions of aircraft structure that are susceptible to MSD or MED. It is recommended that similar MSD analysis be performed for each susceptible region of the RAF VC10 structure to determine its susceptibility to MSD prior to retirement.

REFERENCES

1. Cranfield University Lecture Notes – Damage Tolerance in Aircraft – P E Irving.

2. Cranfield University Lecture Notes - Damage Tolerance and Aircraft Design Residual Strength if Stiffened Panels Ageing Aircraft Issues – T Swift.

3. Airworthiness Assurance Working Group (AAWG) – Recommendations for Regulatory Action to Prevent Widespread Fatigue Damage in the Commercial Airplane Fleet.

4. Flight International – June 2000.

5. The Meaning of Life – J W Bristow & R Minter.

6. The Age of the Plane – J W Bristow.

7. Aircraft of a Certain Age – J W Bristow.

8. Effect of Multiple-Site –Damage on Certified Lead Crack Residual Strength – T Swift.

9. An Experimental and Analytical Investigation on the Fatigue Behaviour of Fuselage Riveted Lap Joints – R P G Muller.

10. Characterisation of MSD in an In-service Fuselage Lap Joint – D Steadman, A Carter and R Ramakrishnan (Delta Airlines).

11. Modified Linkup Models for Determining the Strength and Stiffened Panels with Multiple Site Damage – B L Smith, A L Hijazi, A K M Haque, R V Myose (Wichita State University).

12. Boundary Effects on Residual Strength Analysis of KC-135 Fuselage Panels – D A Cope, T E Lacy, B Clapp, B Haroldson (Boeing & Wichita State University).

13. Modelling the Effect of Prior Corrosion on Fatigue Life Using the Concept of Equivalent Stress Concentration – C A Paul, J P Gallagher.

14. Airbus A300 Fuselage Programme for Life Extension and Widespread Fatigue Evaluation – H-J Schmitt, B Schmidt-Brandecker, H Trey (Daimler Chrysler Aerospace Airbus).

15.   An Example of Widespread Fatigue Damage Assessment in A300 Susceptible Structure – A Santgerma, J Beaufils, B Rosemberg (Aerospatiale Matra Airbus).

16.   An Engineering Approach to the Assessment of Widespread Fatigue Damage in Aircraft Structures – M Balzano, J Beaufils, A Santgerma (Aerospatiale Asronautique).

17.   An Experimental and Numerical Analysis of Multi-Site –Damaged Butt Joints – G Cavallini, R Galatolo, G Cattaneo.

18.   Experimental and Analytical Programme to Determine Strains in 737 Lap Splice Joints Subjected to Normal Fuselage Pressure Loads – D P Roach, D Y Jeong.

19.   Growth of Multiple-Site Fatigue Damage (MSD) in an Undamaged Fuselage Lap Joint Curved Panel – A A Ahmed, J G Bakuskas, P W Tan, J Awerbuch, A C Lau, T Tan.

20.   The Destructive Inspection and Evaluation of Retired Aircraft Fuselage Structure: Analytical Issues and Methods –D Steadman, A Carter, A Makeev (Delta Air Lines).

21.   Destructive Evaluation and Extended Fatigue Testing of Retired Aircraft Fuselage Structure: Project Update – , J G Bakuskas, A Carter.

22.   Some Exact and Approximate Solutions for the Modified von Mises Yield Criterion – J H Lee (University of Alaska Fairbanks).

23.   An Introduction to the Statistical Analysis of Engineering Data – ESDU Data Sheet Number 92040.

24.   Endurance of Riveted Lap Joints (Aluminium Alloy Sheet and Rivets) – ESDU Data Sheet 79031.

25.   Fatigue Behaviour of Metallic Lap Joints: A Study on the Effect of Riveting and of the Specimen Geometry – M Chiarelli, A Lanciotti, L Lazzeri (University of Pisa).

26.   Multiaxial Fatigue: A Survey of the State of Art – Y S Garud.

27.   Fatigue Crack Propagation in Aerospace Aluminium Alloys – R P Gangloff, R S Piascik, D L Dicus, J C Newman Jr.

28.   Durability Analysis Suite from Safe Technology User Manual – FE SafeWorks.

29.   Advances in Fatigue Life Prediction for Multiaxial States of Stress – D V Nelson (Stanford University).

30.   A New Approach to the Evaluation of Fatigue Under Multiaxial Loadings – Y S Garud (Stanford University).

31.   Projecting Aircraft Fleet Reliability – E S Meyer, S S Fields, P A Reid (The Boeing Company).

32.   Stress Intensity Factor Solutions for Countersink Holes Subjected to Combined Loading – J J M de Rijck, S A Fawaz.

33.   Materials Data for Cyclic Loading: Part D Aluminium Alloys & Titanium – C Boller, T Seeger.

34.   Repairs to Damage Tolerant Aircraft – T Swift.

35.   Structural Integrity of Aging Aircraft – C I Chang, C T Sun (629.7.02 STR).

36.   A Study of Geometrical Correction Factors in a MSD Scenario – A N Garcia, P Irving (CAA/W30637E/57).

37.   Fatigue and Corrosion in Aircraft Pressure Cabin Lap Splices – R J H Wanhill, M F J Koolloos (NLR-TP-2000-384).

38.   The Characteristics of Fatigue Damage in Fuselage Riveted Lap Splice Joints – R S Piascik, S A Willard (NASA/TP-97-206257).

39.   Multiple Site Damage in Riveted Lap-Joint Specimens – L M Silva, J P Goncalves, F M F Oliveira, P M S T de Castro.

40.   Mechanical Metallurgy - G E Dieter (539.3DIE).

41.   Multiaxial Fatigue – D F Socie, G B Marquis (539.43SOC).

42.   Fatigue Under Biaxial and Multiaxial Loading – K F Kussmaul, D L McDiarmid, D F Socie (624.042.1KUS).

43.   AFGROW – Linear Elastic Fracture Mechanics Programme.

44.   Analysis and Prediction of Multiple-Site Damage Fatigue Crack Growth – D S Dawicke, J C Newman, Jr (NASA TP3231).

45.   Biaxial Testing of 2195 Aluminium Lithium Alloy Using Cruciform Specimens – W M Johnston, W D Pollock, D S Dawicke (NASA/CR-2002-211942).

46.   Biaxial Testing of 2219-T87 Aluminium Alloy Using Cruciform Specimens – D S Dawicke, W D Pollock (NASA Contractor Report 4782).

47.   The Effect of Ground-to-Air Cycles on the Fatigue Crack Propagation in 2024-T4 Alcad Sheet Material – J Schijve, P De Rijk (NLR-TR M.2148).

48.   The Effect of the Sheet Width on the Fatigue Crack Propagation in 2024-T3 Alclad Material – J Schijve, A Nederveen, F A Jacobs (NLR-TR M2142).

49.   Research on Cumulative Damage in Fatigue of Riveted Aluminium Alloy Joints – J Schijve, F A Jacobs (NLL Report M.1999).

50.   Compendium of Stress Intensity Factors – D P Rooke.

51.   Prediction of Fatigue Life Under Random Loading – E D Poppleton (UTIA/REP-82).

52.   A Note on the Effect of Very Infrequent Load Range Changes on Cumulative Fatigue Damage – J A Dunsby, F R Thurston (NRC 6737).

53.   The Effect of Sheet Thickness on Fatigue-Crack Propagation in 2024-T4 Alclad Sheet Material – D. Broek, J Schijve (NLR-TR M2129).

54.   Analysis of the Fatigue Phenomenon in Aluminium Alloys – J Schijve (NLR-TR M2122).

55.   Advances in Fatigue and Fracture Mechanics Analyses for Metallic Aircraft Structures – J C Newman Jr (NASA/TM-2000-210084).

56.   Practical Applications of Fracture Mechanics in Aircraft and Aerospace Structural Problems – J J Kacprzynski (NRC20415).

APPENDIX A – RAF VC10 Stress Spectra Analysis

A.1   Introduction

To make the extended fatigue test applied load as realistic as possible, a stress spectra obtained from an in-service instrumented RAF VC10 aircraft was to be applied to the specimens. Initially, tests would be performed using a longitudinal stress spectrum to determine the fatigue life of the specimen and then obtain a similar single cycle load that would produce a similar fatigue life. Unfortunately, there was insufficient time in which to conduct the variable amplitude fatigue tests and a constant amplitude cycles from the FS1045 stress spectrum was eventually used for the extended fatigue specimen tests.

This Appendix explains how the stress spectrum for the crown of the fuselage at FS1045 was obtained and what constant amplitude load, used for the majority of the tests, was selected.

A.2   Operation Loads Measurements (OLM) Programme

To validate the RAF VC10 damage tolerance analysis described at Chapter 3, various Operational Load Measurement (OLM) Programmes have been conducted on RAF VC10 since 1986.   The Programmes essentially involve fixing strain gauges to the areas of the airframe under evaluation and recording the loads experienced by the structure for numerous flight cycles. One such OLM Programme included the instrumentation of the fuselage crown of a RAF VC10 KMk2 as detailed at Figure A-1 below.

After the data from the OLM Programme had been collected for various different sortie profile codes (see Chapter 3) it was subjected to rain-flow analysis and then weighted in an appropriate manner to generate spectra for a typical average VC10 KMk2 flight. The spectra produced for each of the instrumented fuselage stations (Table A-1 to Table A-4) identified that Fuselage Station (FS) 1045 was subjected to the highest longitudinal stresses. It was, therefore, decided to try to predict the onset of MSD in a RAF VC10 circumferential butt joint at the crown of FS 1045. The spectra foe FS1045 had however been supplied in order of magnitude and to try to duplicate a typical sortie the oorder of the stresses throughout the flight had to be determined as detailed below.
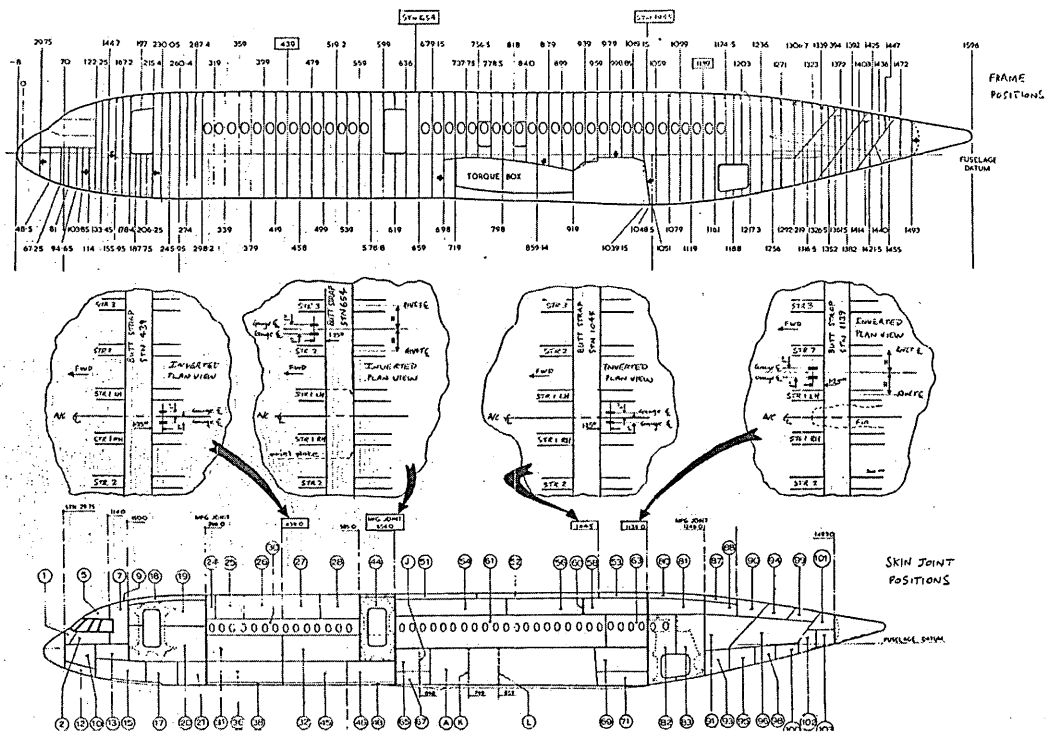
Figure A-1: Location of Strain Gauges for Fuselage Butt Strap OLM Programme

A.3 FS1045 Stress Spectrum

A.3.1 Sequencing

The data provided at Table A-5 was used to sequence the stress spectrum provided at Table A-3, for FS1045, to be more representative of a typical RAF VC10 sortie.

A.3.2 Test Spectrum

Once the spectrum had been sequenced the correct number of cycles at each particular maximum stress level had to be allocated to the overall spectrum. To prevent having 10 different spectrum cycles within the overall spectrum for FS1045 it was decided to amalgamate all the cycles into one spectrum, which would represent 10 typical average RAF VC10 flights. The spectrum is provided at Table A-6 and Figure A-2 below.

A.3.3 Constant Amplitude Loads

As explained above, there was insufficient time in which to determine a constant amplitude load that would produce the same fatigue damage as the spectrum for FS1045. It was therefore decided to select the maximum peak cycle load from the FS1045 spectrum and assume that this cycle was representative of the fatigue damage experienced at FS1045 during a typical average RAF VC10 sortie. The cycle selected was as follows:

Maximum Stress	=	108MPa
Stress Ratio R	=	0.212

To ensure that the extended fatigue tests could be completed within the time constraints of the Project, specimens were initially tested at the following loads until it was determined that the above load would cause the specimen to fail within a suitable period of time:

Maximum Stress	=	163MPa
Maximum Stress	=	135MPa
Maximum Stress	=	120MPa
All with a Stress Ratio R	=	0.212

VC10 KMk2 Stress Spectrum
Fuselage Station 439

Delta Sigma (psi)	N (per flight)	R (sigma min/sigma max)
10392.555	0.1489	-0.47132
8419.731	0.1289	-0.38551
7926.525	0.1667	-0.1509
6446.907	0.5555	-0.04871
3487.671	0.1489	0.39077
2501.259	0.5555	-0.21368
2501.259	0.1289	-1.49123
2501.259	0.3378	0.52189
2501.259	0.1489	0.60224
2008.053	1.7222	0.59717
2008.053	0.1289	-0.1068
2008.053	0.1489	0.66764
2008.053	0.5555	0.48879
2008.053	0.1289	-1.65116

Table A-1: Stress Spectrum FS439

VC10 KMk2 Stress Spectrum
Fuselage Station 654

Delta Sigma (psi)	N (per flight)	R (sigma min/sigma max)
11975.238	0.1489	-0.15398
10991.934	0.1667	-0.00482
10991.934	0.1289	-0.1119
9516.978	0.5555	0.06713
4600.458	0.1489	0.53298
4108.806	0.1889	0.57221
3617.154	0.2978	0.61351
3617.154	0.1489	0.65261
3125.502	0.3156	0.69257
3125.502	0.1289	0.18721
3125.502	0.1667	0.65703
3125.502	0.7044	0.6122
2633.85	0.5555	0.26829
2633.85	1.1689	0.66292
2633.85	0.5555	0.73451
2633.85	0.8889	0.70297
2142.198	0.2578	0.51394
2142.198	0.5555	0.60772
2142.198	1.02	0.75153
2142.198	0.1289	0.0687
2142.198	0.4645	0.80033
2142.198	3.8976	0.71694
2142.198	0.4867	0.77858
1650.546	1.2045	0.77458
1650.546	0.2778	0.46893
1650.546	0.5555	0.82495
1650.546	0.5555	0.6835

Table A-2: Stress Spectrum FS654

VC10 KMk2 Stress Spectrum
Fuselage Station 1045

Delta Sigma (psi)	N (per flight)	R (sigma min/sigma max)
12328.6175	0.1489	0.21199
10383.8215	0.1289	0.17517
8925.2245	0.1667	0.24744
8439.0255	0.5555	0.27354
6494.2295	0.3178	0.38989
6008.0305	0.5555	0.42237
5521.8315	0.1489	0.61455
5521.8315	0.1489	0.45641
4549.4335	0.7044	0.57536
4549.4335	0.1667	0.52962
4063.2345	0.1489	0.67635
4063.2345	0.1667	0.64706
4063.2345	0.5555	0.61194
3577.0355	0.2956	0.68259
3577.0355	1.111	0.56077
3577.0355	0.1489	0.70945
3577.0355	0.2978	0.65025
3090.8365	0.1289	0.65437
3090.8365	0.1489	0.7816
3090.8365	0.5445	0.69043
3090.8365	0.9333	0.60879
3090.8365	0.1667	0.71969
2604.6375	0.5756	0.77974
2604.6375	0.3556	0.75845
2604.6375	2.1889	0.73262
2604.6375	1.7822	0.65986
2604.6375	0.2956	0.7006
2604.6375	0.6844	0.6063
2604.6375	0.1489	0.79757
2118.4385	0.2978	0.81709
2118.4385	0.1489	0.84498
2118.4385	3.8976	0.71429
2118.4385	0.6844	0.60261
2118.4385	2.7775	0.66757
2118.4385	2.2048	0.74949
2118.4385	2.8867	0.77697
2118.4385	1.4112	0.79901
1632.2395	0.5555	0.73371
1632.2395	1.3556	0.82364
1632.2395	0.1667	0.84148
1632.2395	1.0911	0.7724
1632.2395	0.1667	0.80127

Table A-3: Stress Spectrum FS1045

VC10 KMk2 Stress Spectrum
Fuselage Station 1139

Delta Sigma (psi)	N (per flight)	R (sigma min/sigma max)
11497.974	0.1489	0.2111
9528.902	0.1289	0.23983
8052.098	0.1667	0.31744
6575.294	0.5555	0.34271
6575.294	0.1889	0.26523
6083.026	0.3666	0.37658
5590.758	0.1889	0.4122
5098.49	0.1289	0.44972
4606.222	0.1489	0.62193
4606.222	0.1489	0.48928
4113.954	0.7044	0.53106
3621.686	0.1667	0.6595
3621.686	0.1667	0.57526
3621.686	0.1489	0.69023
3129.418	0.1489	0.72657
3129.418	0.2956	0.69882
3129.418	0.5555	0.56691
3129.418	0.6844	0.62208
3129.418	0.1889	0.49288
2637.15	0.3156	0.67177
2637.15	0.2978	0.78479
2637.15	0.1667	0.74003
2637.15	0.5267	0.70986
2637.15	0.1489	0.76452
2637.15	0.9221	0.62217
2144.882	1.7156	0.68146
2144.882	0.6112	0.7833
2144.882	0.2978	0.80417
2144.882	0.5555	0.62229
2144.882	2.4	0.75746
2144.882	1.6112	0.7246
1652.614	0.5956	0.84565
1652.614	6.3683	0.69579
1652.614	0.649	0.82878
1652.614	4.1626	0.78089
1652.614	5.7465	0.74526
1652.614	0.1489	0.85949
1652.614	3.1043	0.80777

Table A-4: Stress Spectrum FS1139

File created by – Program CSG036 – Version 4.0

Working Directory – /import/cdstu01/stu014/stress/cmk1/fuselage/file_224

Input Files – cn007v09rff.key.1
cn007v09rfg.key.1
cn007v09rfh.key.1
cn007v09rfi.key.1
cn007v10rox.key.1

Output Files – Q58346_spc12_nx_mid_real.tbl

Results For – Element Number – 68346
Result Type – Normal-x middle surface

Fatigue Event	1 dP Pressure	1g Flight	dg Man.	10ft/s Gust	1g on Grnd.	Thrust Load	2 Pt. Landing	Lateral Load
g5	0	0	0	0	6651.465	0	0	0
1	0	12603.23	9447.301	493.9170	0	0	0	37.00880
2a	14.80989	13003.38	9410.978	526.4170	0	0	0	39.14531
2b	14.80989	13346.54	9338.783	553.9526	0	0	0	41.35967
3a	1038.187	15077.91	9140.908	696.5897	0	0	0	48.89915
3b	1038.187	10947.46	8889.732	912.7402	0	0	0	60.38953
4	4559.109	11113.73	9218.693	2155.183	0	0	0	35.55462
5	4559.109	11018.08	9119.319	2301.125	0	0	0	33.13142
6	4671.889	10895.90	9268.539	2123.268	0	0	0	27.06052
7	4671.889	11336.29	9724.549	2157.297	0	0	0	35.73777
8a	2040.214	10905.18	8855.551	1486.216	0	0	0	47.00217
8b	2040.214	10620.51	9052.567	1255.939	0	0	0	42.27184
9a	741.5689	10609.55	9025.312	1199.710	0	0	0	41.76318
9b	741.5689	13580.12	9215.479	909.5242	0	0	0	33.32131
10a	266.9517	12191.38	9307.607	735.1536	0	0	0	27.15972
10b	266.9517	14186.24	9170.461	583.1827	0	0	0	26.89474
g5	0	0	0	0	7099.418	0	0	0

DATUM CASE	DESCRIPTION	HEIGHT (ft)	FUEL WEIGHT (lbs)	FLAPS	AIRBRAKE	AILERON UPLIFT (degrees)	EAS (knots)	UNDER-CARRIAGE
	RAMP		90000					
	START TAKEOFF RUN		88000					
1	LIFT OFF	0	86000	TAKEOFF	IN	2.5	151	DOWN
2a	INITIAL CLIMB	50	85985	TAKEOFF	IN	2.5	161	DOWN
2b	INITIAL CLIMB	50	85985	TAKEOFF	IN	2.5	170	UP
3a	CLIMB	3500	85205	TAKEOFF	IN	2.5	207	UP
3b	CLIMB	3500	85205	IN	IN	2.5	285	UP
4	END CLIMB/ START CRUISE	33000	78500	IN	IN	2.5	274	UP
5	END CRUISE/ START CLIMB	33000	64500	IN	IN	2.5	274	UP
6	END CLIMB/ START CRUISE	37000	63500	IN	IN	2.5	249	UP
7a	END CRUISE	37000	23800	IN	IN	2.5	249	UP
7b	START DESCENT	37000	23800	IN	IN	2.5	249	UP
8a	DESCENT	10000	22860	IN	IN	2.5	283	UP
8b	DESCENT	10000	22860	IN	IN	2.5	244	UP
9a	START APPROACH	2500	22600	IN	IN	2.5	245	UP
9b	START APPROACH	2500	22600	TAKEOFF	IN	2.5	177	DOWN
10a	FINAL APPROACH	900	22150	TAKEOFF	IN	2.5	144	DOWN
10b	FINAL APPROACH	900	22150	LANDING	IN	2.5	135	DOWN

VC10 C.Mk.1   SPC 12

ZPW ~ 190,000 lbs

FIN TRIM SYSTEM ON

Table A-5: Sequencing Data

Table A-6: FS1045 Spectrum - Percentage of Maximum Load

| #	%	#	%	#	%	#	%	#	%	#	%	#	%	#	%	#	%
1	0.340735	51	0.407317	101	0.591563	151	0.540515	201	0.473923	251	0.473923	301	0.684784	351	0.607114	401	0.673688
2	0.20533	52	0.271913	102	0.487235	152	0.405111	202	0.338518	252	0.338518	302	0.393997	352	0.471709	402	0.538283
3	0.340735	53	0.407317	103	0.591563	153	0.540515	203	0.473923	253	0.473923	303	0.684784	353	0.607114	403	0.673688
4	0.20533	54	0.271913	104	0.487235	154	0.405111	204	0.338518	254	0.338518	304	0.393997	354	0.471709	404	0.538283
5	0.340735	55	0.407317	105	0.591563	155	0.540515	205	0.473923	255	0.473923	305	0.684784	355	0.607114	405	0.673688
6	0.20533	56	0.271913	106	0.487235	156	0.405111	206	0.338518	256	0.338518	306	0.393997	356	0.471709	406	0.538283
7	0.340735	57	0.407317	107	0.591563	157	0.540515	207	0.473923	257	0.473923	307	0.684784	357	0.607114	407	0.673688
8	0.20533	58	0.271913	108	0.487235	158	0.405111	208	0.338518	258	0.338518	308	0.393997	358	0.471709	408	0.538283
9	0.340735	59	0.407317	109	0.591563	159	0.540515	209	0.473923	259	0.473923	309	0.684784	359	0.607114	409	0.673688
10	0.20533	60	0.271913	110	0.487235	160	0.405111	210	0.338518	260	0.338518	310	0.393997	360	0.471709	410	0.538283
11	0.340735	61	0.407317	111	0.591563	161	0.540515	211	0.473923	261	0.556049	311	0.658138	361	0.607114	411	0.673688
12	0.20533	62	0.271913	112	0.487235	162	0.405111	212	0.338518	262	0.389568	312	0.55381	362	0.471709	412	0.538283
13	0.340735	63	0.407317	113	0.591563	163	0.540515	213	0.473923	263	0.556049	313	0.658138	363	0.607114	413	0.673688
14	0.20533	64	0.271913	114	0.487235	164	0.405111	214	0.338518	264	0.389568	314	0.55381	364	0.471709	414	0.538283
15	0.407317	65	0.407317	115	0.591563	165	0.540515	215	0.473923	265	0.556049	315	0.607114	365	0.607114	415	0.673688
16	0.271913	66	0.271913	116	0.487235	166	0.405111	216	0.338518	266	0.389568	316	0.471709	366	0.471709	416	0.538283
17	0.407317	67	0.407317	117	0.591563	167	0.540515	217	0.473923	267	0.735848	317	0.607114	367	0.607114	417	0.68922
18	0.271913	68	0.271913	118	0.487235	168	0.405111	218	0.338518	268	0.476138	318	0.471709	368	0.471709	418	0.522739
19	0.407317	69	0.407317	119	0.591563	169	0.540515	219	0.473923	269	0.735848	319	0.607114	369	0.607114	419	0.68922
20	0.271913	70	0.271913	120	0.487235	170	0.405111	220	0.338518	270	0.476138	320	0.471709	370	0.471709	420	0.522739
21	0.407317	71	0.407317	121	0.591563	171	0.540515	221	0.473923	271	0.7869	321	0.607114	371	0.607114	421	0.68922
22	0.271913	72	0.271913	122	0.487235	172	0.405111	222	0.338518	272	0.558266	322	0.471709	372	0.471709	422	0.522739
23	0.407317	73	0.504991	123	0.591563	173	0.540515	223	0.473923	273	0.7869	323	0.607114	373	0.669253	423	0.68922
24	0.271913	74	0.307433	124	0.487235	174	0.405111	224	0.338518	274	0.558266	324	0.471709	374	0.409543	424	0.522739
25	0.407317	75	0.504991	125	0.591563	175	0.540515	225	0.473923	275	0.822413	325	0.607114	375	0.669253	425	0.704782
26	0.271913	76	0.307433	126	0.487235	176	0.405111	226	0.338518	276	0.655932	326	0.471709	376	0.471709	426	0.507225
27	0.407317	77	0.504991	127	0.742503	177	0.540515	227	0.473923	277	0.822413	327	0.607114	377	0.607114	427	0.704782
28	0.271913	78	0.307433	128	0.203104	178	0.405111	228	0.338518	278	0.655932	328	0.471709	378	0.471709	428	0.507225
29	0.407317	79	0.504991	129	0.742503	179	0.540515	229	0.473923	279	0.873465	329	0.607114	379	0.607114	429	0.74028
30	0.271913	80	0.307433	130	0.203104	180	0.405111	230	0.338518	280	0.73806	330	0.471709	380	0.471709	430	0.604875
31	0.407317	81	0.504991	131	0.742503	181	0.473923	231	0.473923	281	0.873465	331	0.607114	381	0.607114	431	0.74028
32	0.271913	82	0.307433	132	0.203104	182	0.338518	232	0.338518	282	0.73806	332	0.471709	382	0.471709	432	0.604875
33	0.407317	83	0.504991	133	0.742503	183	0.473923	233	0.473923	283	0.802442	333	0.607114	383	0.607114	433	0.74028
34	0.271913	84	0.307433	134	0.203104	184	0.338518	234	0.338518	284	0.542732	334	0.471709	384	0.471709	434	0.604875
35	0.407317	85	0.504991	135	0.742503	185	0.473923	235	0.473923	285	0.802442	335	0.607114	385	0.607114	435	0.904567
36	0.271913	86	0.307433	136	0.203104	186	0.338518	236	0.338518	286	0.542732	336	0.471709	386	0.471709	436	0.70701
37	0.407317	87	0.504991	137	0.742503	187	0.473923	237	0.473923	287	0.915656	337	0.607114	387	0.673688	437	0.904567
38	0.271913	88	0.307433	138	0.203104	188	0.338518	238	0.338518	288	0.562717	338	0.471709	388	0.538283	438	0.70701
39	0.407317	89	0.653707	139	0.540515	189	0.473923	239	0.473923	289	0.915656	339	0.607114	389	0.673688	439	1
40	0.271913	90	0.425073	140	0.405111	190	0.338518	240	0.338518	290	0.562717	340	0.471709	390	0.538283	440	0.21199
41	0.407317	91	0.653707	141	0.540515	191	0.473923	241	0.473923	291	0.720311	341	0.607114	391	0.673688	441	0.755838
42	0.271913	92	0.425073	142	0.405111	192	0.338518	242	0.338518	292	0.491677	342	0.471709	392	0.538283	442	0.589358
43	0.407317	93	0.653707	143	0.540515	193	0.473923	243	0.473923	293	0.720311	343	0.607114	393	0.673688	443	0.755838
44	0.271913	94	0.425073	144	0.405111	194	0.338518	244	0.338518	294	0.491677	344	0.471709	394	0.538283	444	0.589358
45	0.407317	95	0.758046	145	0.540515	195	0.473923	245	0.473923	295	0.720311	345	0.607114	395	0.673688	445	0.755838
46	0.271913	96	0.187571	146	0.405111	196	0.338518	246	0.338518	296	0.491677	346	0.471709	396	0.538283	446	0.589358
47	0.407317	97	0.758046	147	0.540515	197	0.473923	247	0.473923	297	0.684784	347	0.607114	397	0.673688	447	0.755838
48	0.271913	98	0.187571	148	0.405111	198	0.338518	248	0.338518	298	0.393997	348	0.471709	398	0.538283	448	0.589358
49	0.407317	99	0.591563	149	0.540515	199	0.473923	249	0.473923	299	0.684784	349	0.607114	399	0.673688	449	0.755838
50	0.271913	100	0.487235	150	0.405111	200	0.338518	250	0.338518	300	0.393997	350	0.471709	400	0.538283	450	0.589358
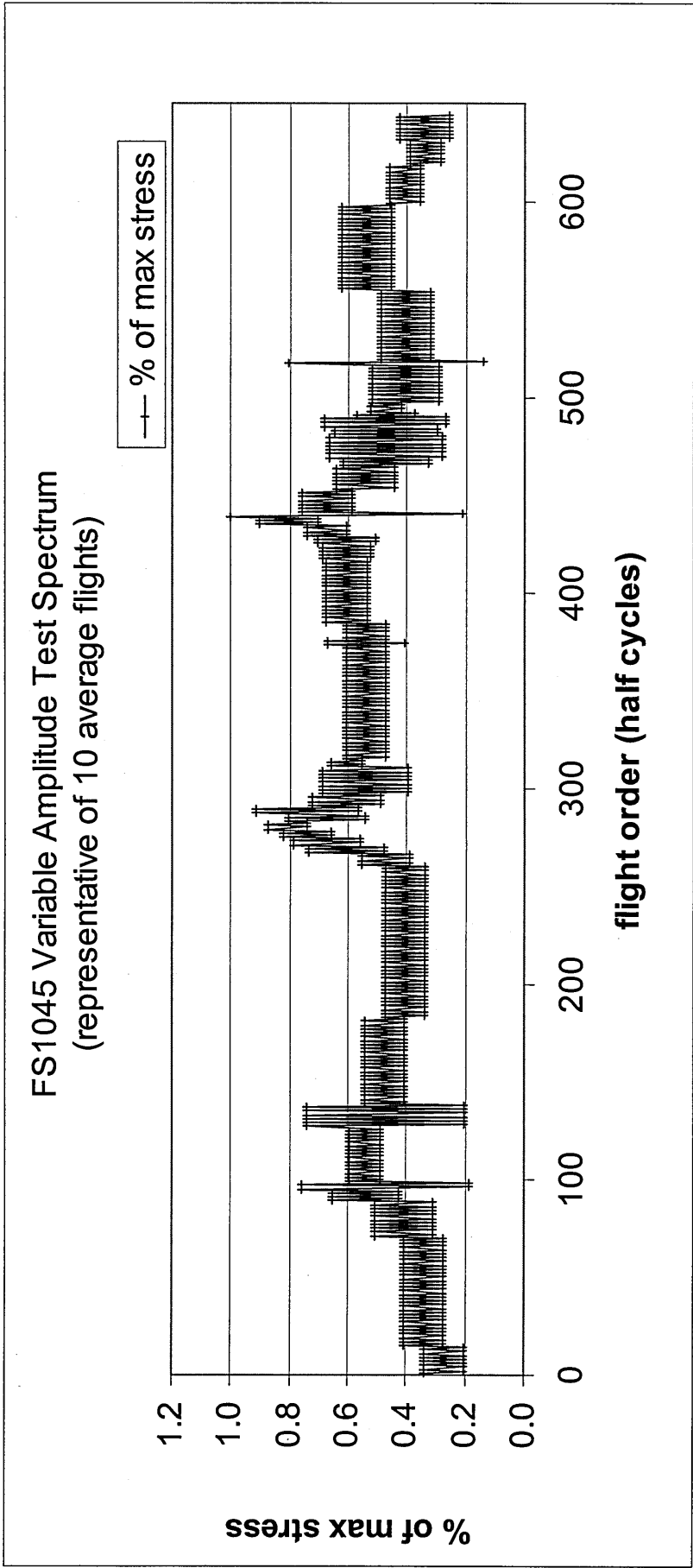
Figure A-2: FS1045 Stress Spectrum

APPENDIX B – Test Specimen Results & Fracture Surface Analysis

B.1 Introduction

This Appendix provides a list of the extended fatigue test results for all of the failed test specimens along with test specimen observations, were applicable. The fracture surfaces of each failed test specimen are then analysed, supported by various different magnitude micrograph images. A total of 6 specimen fracture surfaces were then selected to be analysed further using images from a Scanning Electron Microscope (SEM) as detailed within this Appendix.

B.2 Test Specimen Results

As detailed at Chapter 4, a total of 25 test specimens were produced from an airframe panel removed from the crown of a RAF VC10 fuselage at FS1045 containing a circumferential butt joint. A total of 23 specimens were uniaxially constant amplitude fatigue tested to failure at various different loads. The remaining 2 specimens were supposed to be tested using a variable amplitude load but there was insufficient time in which to complete these tests. The total number of test cycles required to fail each of these specimens at each particular test load is recorded at Table B-1 and Figure B-1. Any variations in the specimens and observations made during and after the test have also been recorded in this table.

B.3 Initial Fracture Surface Analysis

Each of the failed specimen fracture surfaces were initially analysed using a microscope and digital images of the fracture surface at magnifications between 0.5 and 3 microns were recorded and reproduced at Figures B-2 to B-26. All of the specimens tested failed at the outer most rivet of the butt joint apart from Specimen#19 and Speciemen#24, which both failed along the butt strap at the point where the 2 outer skins met. The digital images produced at Figures B-2 to B-26 are all images of the fracture surface belonging to the smaller end of the broken specimen. Images of the fracture surface were taken either side of the countersink hole, which contained the outer most rivet of the joint.

The images all concentrate on the region of crack initiation, which for all of the specimens, apart from Specimen#19 and Speciemen#24, was determined to be the area of highest stress concentration at the tip of the countersink. The majority of the images show a fairly defined region of fatigue fracture leading to regions of fatigue and ductile fracture and ending in ductile fracture. The average length of the fatigue crack was determined to be approximately 3.5mm long.

B.4 Scanning Electron Microscope Analysis

After performing the initial fracture surface analysis detailed above, 6
specimens, that showed possible evidence of corrosion, were selected and
analysed using a Scanning Electron Microscope (SEM). Again, the images all
concentrate on the region of crack initiation at the extreme point of the
countersink. The fracture surfaces of the selected specimens shown a Figures
B-27 to B-32 are the same as those analysed using the microscope, as
explained above. The selected specimens were:

    a.   Specimen#9.

    b.   Specimen#10.

    c.   Specimen#11.

    d.   Specimen#15.

    e.   Specimen#21.

    f.   Specimen#23.

The specimens had to be cut approximately 5mm below the fracture surface to
be able to fit them in the SEM. The SEM has a far greater field of view than the
microscope used in the above analysis and is able to produce high definition
images at higher magnifications. The SEM analysis proves the presence of
fatigue and ductile fractures but also identifies amorphous regions, which are
extremely likely to be caused by the presence of corrosion.

| Specimen #	Rivets	Load Type	Max Load N	Amplitude N	Mean Load N	# test cycles to failure	# segment to failure	Comments
1(50%)	8	CA	4474.35	1762.9163	2711.434	13008	N/A	slightly offset end rivet, little crack growth, rear fuselage break, discoloured countersink, squeeze force slightly
2(50%)	6	CA	4474.35	1762.9163	2711.434	13613	N/A	slightly offset end rivet, little crack growth, rear fuselage break, discoloured countersink, squeeze force slightly
3(25%)	8	CA	3701.297	1458.3297	2242.968	23434	N/A	slightly offset end rivet, small sign of crack growth, rear fuselage break, discoloured countersink, squeeze force
4(25%)	6	CA	3701.297	1458.3297	2242.968	36945	N/A	all rivets approximately central, small sign of crack growth, rear fuselage break, fairly clean looking countersink
5(0%)	8	CA	2961.038	1166.6637	1794.374	83067	N/A	all rivets approximately central, clear crack growth region, front fuselage break, clean looking countersink, squ
6(0%)	8	CA	2961.038	1166.6637	1794.374	113564	N/A	slightly offset end rivet, clear crack growth region, front fuselage break, clean looking countersink, squeeze for
7(-11%)	6	CA	2635.324	1038.3307	1596.993	382080	N/A	slightly offset end rivet (preloaded to 5KN), good crack growth region, front fuselage break, clean looking count
8(-11%)	8	CA	2635.324	1038.3307	1596.993	147549	N/A	all rivets approximately central, good crack growth region, rear fuselage break, fairly clean looking countersink,
9(-11%)	6	CA	2635.324	1038.3307	1596.993	341773	N/A	all rivets approximately central, good crack growth region, front fuselage break, clean looking countersink, squ
10(+11%)	8	CA	3294	1297.8525	1996.148	62768	N/A	slightly offset end rivet, good crack growth region, rear fuselage break, discoloured countersink, squeeze force
11(0%)	8	CA	2961.038	1166.6637	1794.374	88930	N/A	all rivets approximately central, good crack growth region, front fuselage break, clean looking countersink (frett
12(0%)	6	CA	2961.038	1166.6637	1794.374	162973	N/A	slightly offset end rivet, clear crack growth region, front fuselage break, clean looking countersink
13(0%)	8	CA	2961.038	1166.6637	1794.374	47653	N/A	all rivets approximatley central, good crack growth region, front fuselage break, discoloured countersink, sque
14(0%)	6	VA	2961.038	N/A	N/A	NT	NT	all rivets approximatley central - not tested
15(-11%)	8	CA	2635.324	1038.3307	1596.993	494720	N/A	all rivets approximately central, good crack growth region, front fuselage break, slightly discoloured countersink
16(+11%)	8	CA	3294	1297.8525	1996.148	55621	N/A	all rivets approximately central, good crack growth region, front fuselage break, clean looking countersink, squ
17(0%)	6	CA	2961.038	1166.6637	1794.374	223780	N/A	(146000+46000+31780) all rivets approximately central, good crack growth region, front fuselage break, clean
18(0%)	8	VA	2961.038	N/A	N/A	PT	PT	partially tested to 5081 sequences 3270277 segs
19(0%)	6	CA	2961.038	1166.6637	1794.374	167923	N/A	slightly offset end rivet, 2 new replacement rivets, **specimen broke at join**, crack initiated from surface at join
20(0%)	8	CA	2961.038	1166.6637	1794.374	83094	N/A	all rivets approximately central, one replacement rivet, good crack growth region, front fuselage break, discolou
21(0%)	8	CA	2961.038	1166.6637	1794.374	103485	N/A	slightly offset end rivet, good crack growth region, front fuselage break, discoloured countersink, squeeze force
22(0%)	6	CA	2961.038	1166.6637	1794.374	209816	N/A	slightly offset end rivet, good crack growth region, front fuselage break, clean looking countersink
23(0%)	8	CA	2961.038	1166.6637	1794.374	89298	N/A	slightly offset end rivet, good crack growth region, front fuselage break, discoloured countersink, squeeze force
24(0%)	6	CA	2961.038	1166.6637	1794.374	100057	N/A	slightly offset end rivet, **specimen broke at join**, crack initiated from score mark at surface of join, good crack
25(0%)	8	CA	2961.038	1166.6637	1794.374	50168	N/A	slightly offset end rivet, good crack growth region, front fuselage break, discoloured countersink, squeeze force

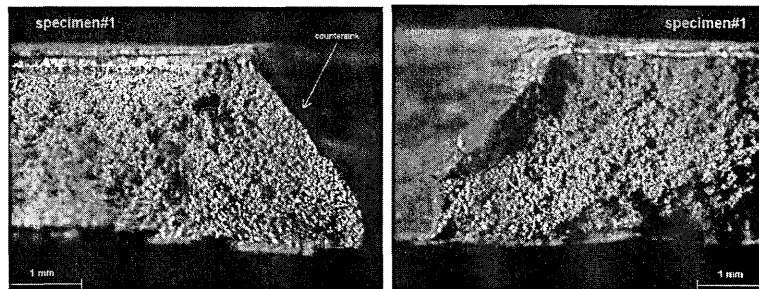**Table B-1: Test Specimen Results**

TEST SPECIMEN S-N CHART
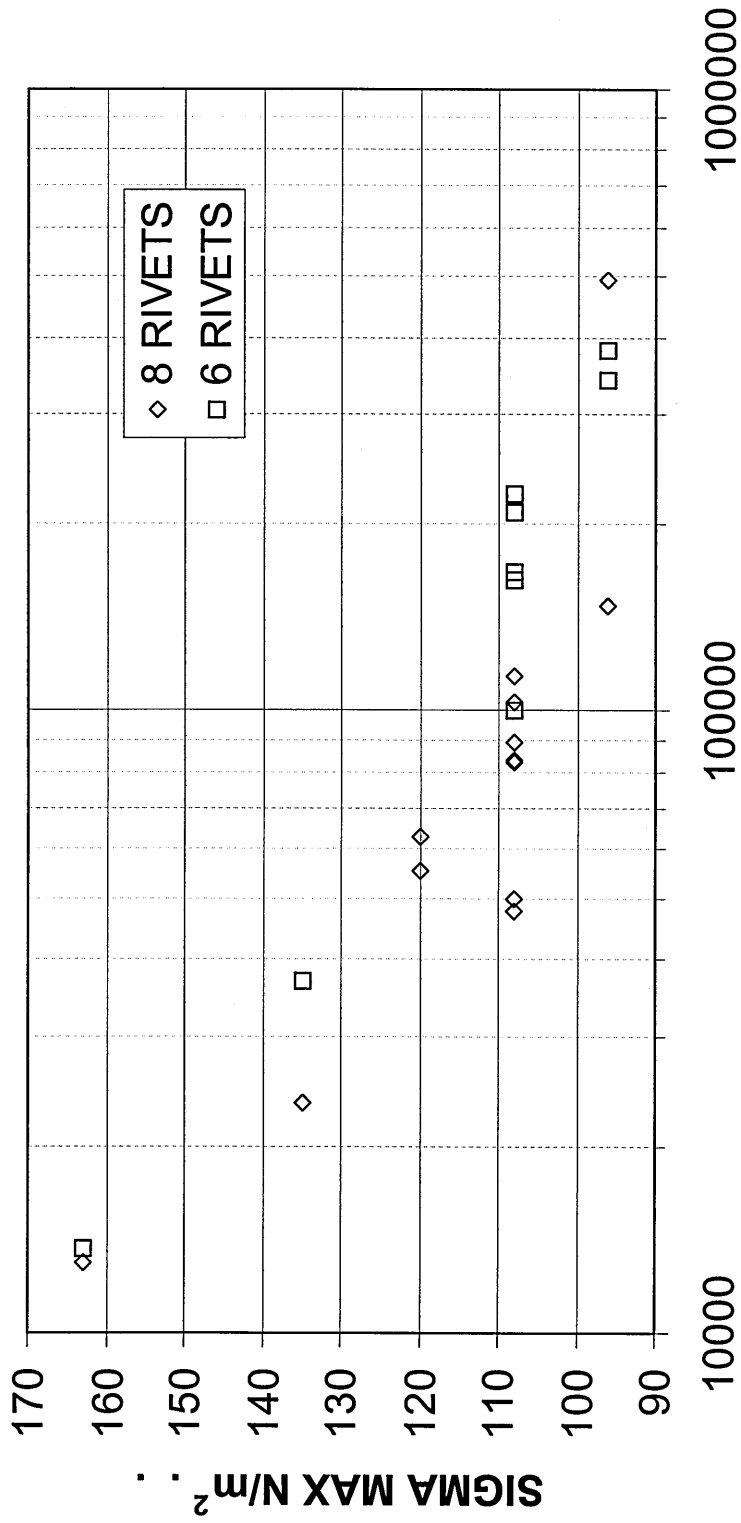
Figure B-1: Test Specimen S-N Chart
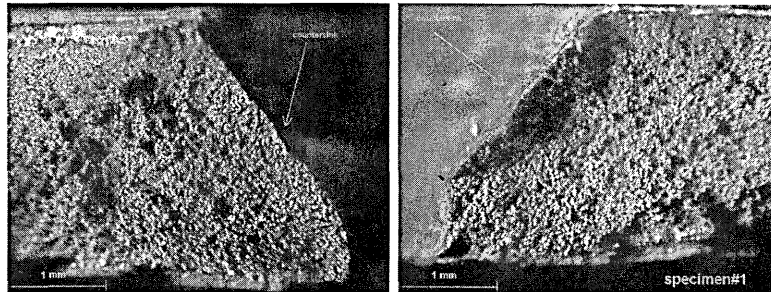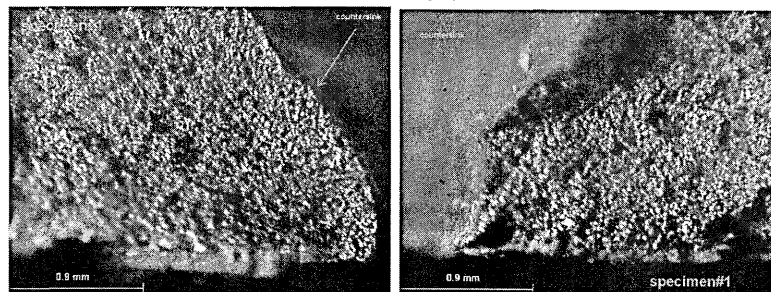
Specimen#1
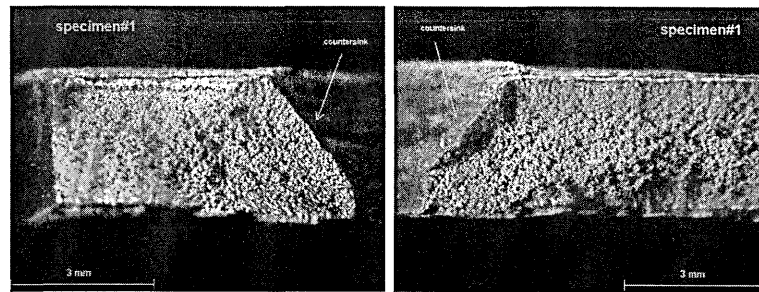
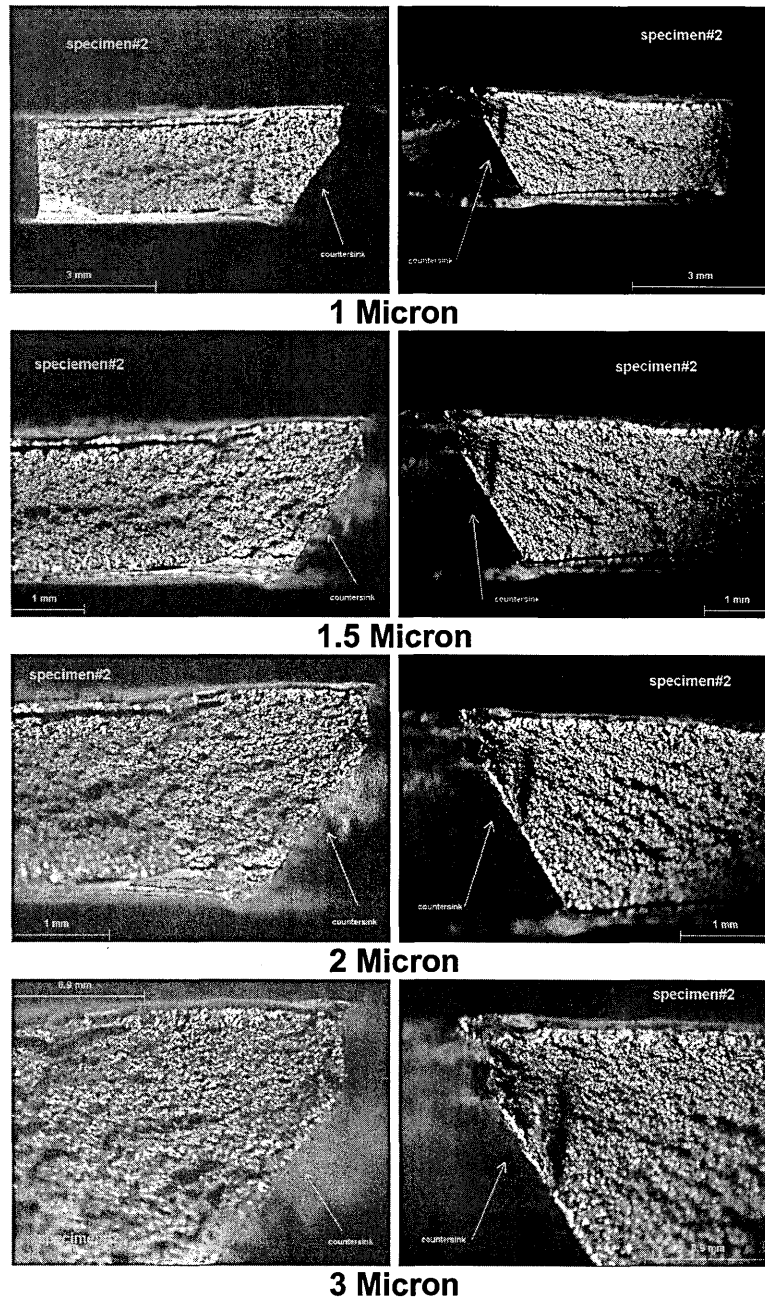**1 Micron**

1.5 Micron

2 Micron

3 Micron
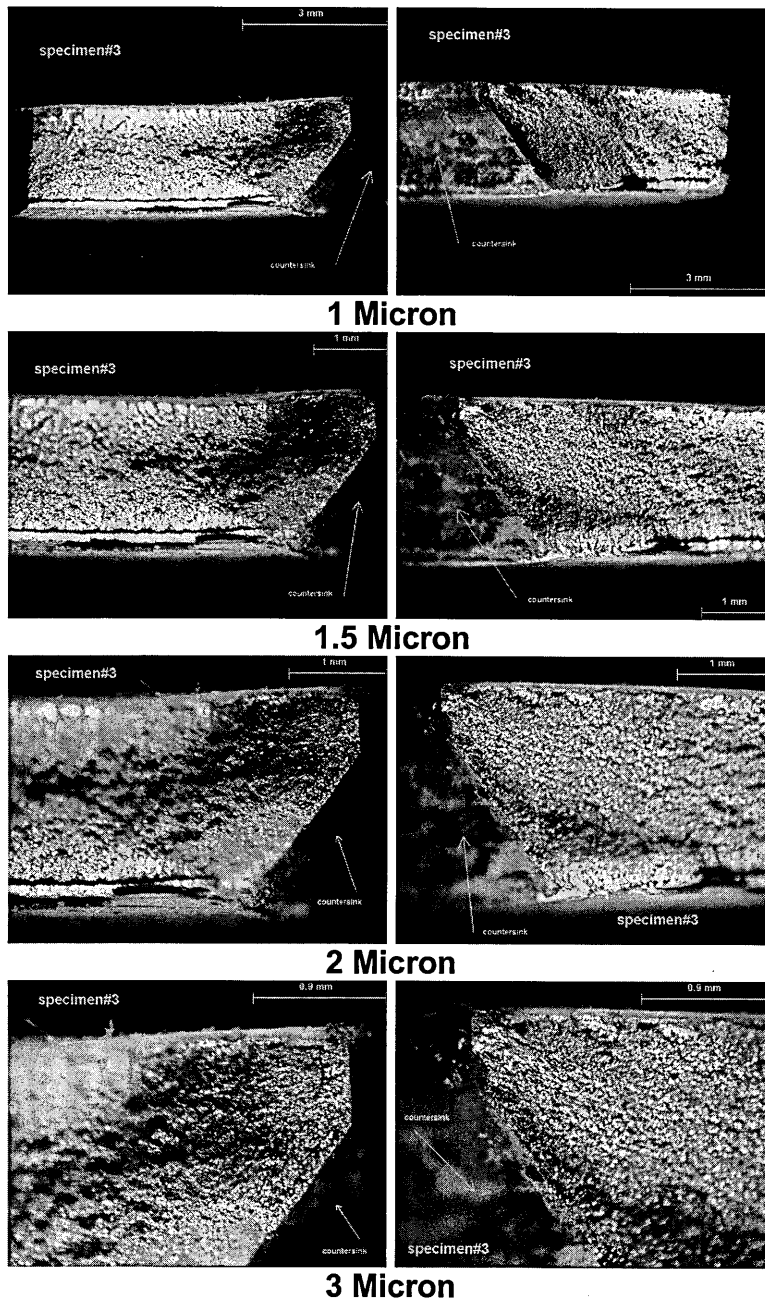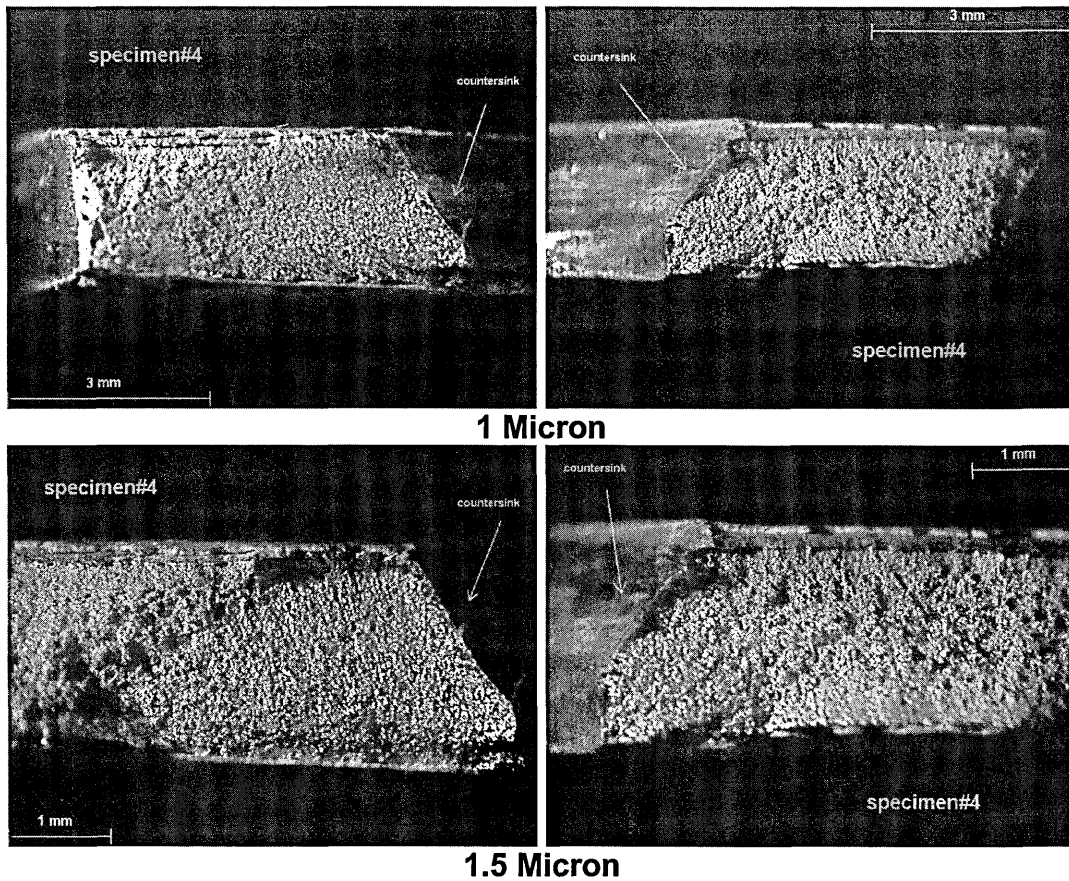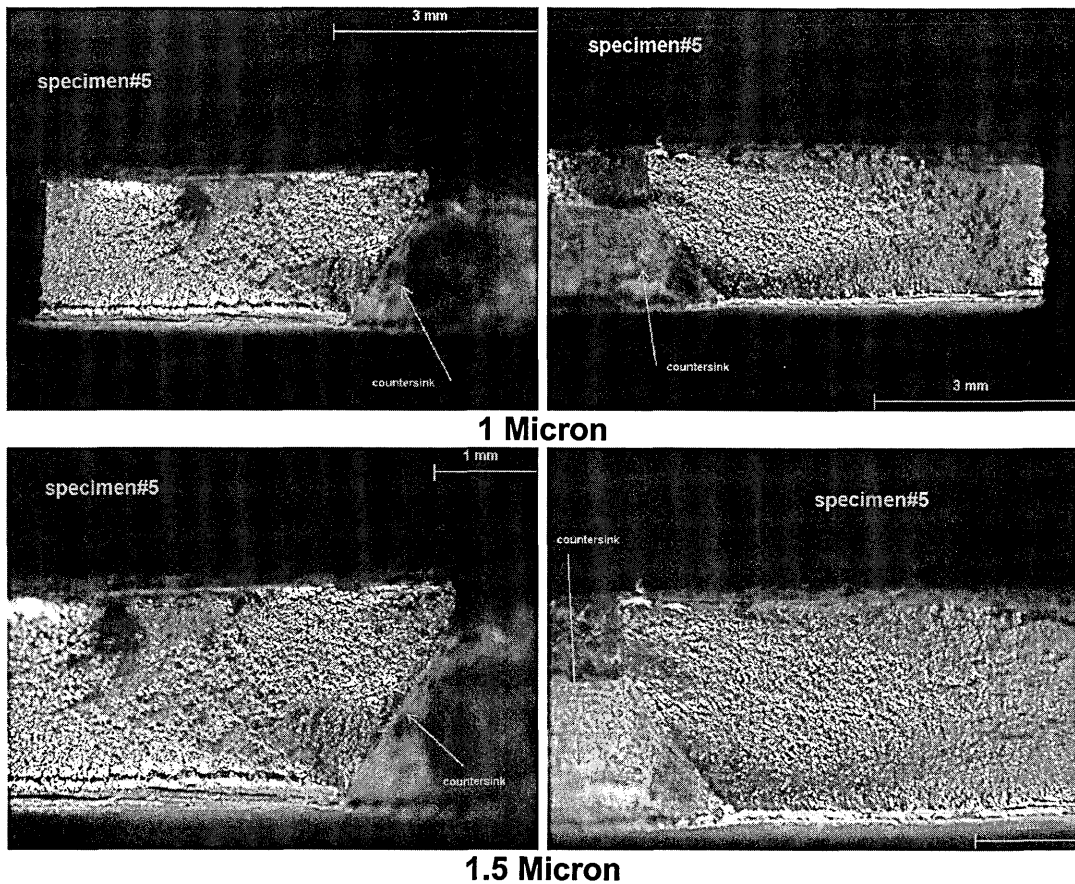
Specimen#1 (8-Rivets) took 13008 constant amplitude test cycles to fail at a maximum load of 4.5KN (R=0.2). The fatigue crack initiated at the tip of the countersink and propagated to approximately 2mm before the specimen fractured. The higher magnification images show small defects at the extreme tip of the countersink.

Figure B-2: Specimen#1-Fracture Surface (1 to 3 microns)

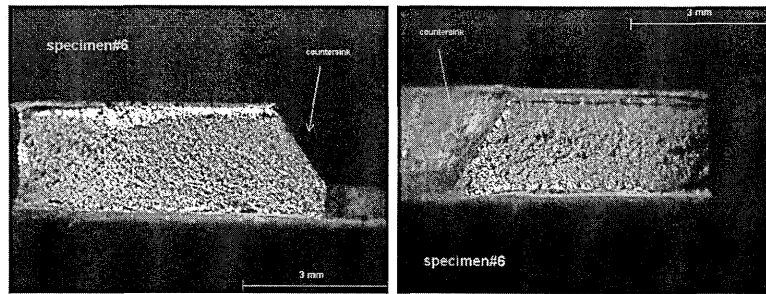# Specimen#2

1 Micron

1.5 Micron

2 Micron

3 Micron

Specimen#2 (6-Rivets) took 13618 constant amplitude test cycles to fail at a maximum load of 4.5KN (R=0.2). The fatigue crack initiated at the tip of the countersink and propagated to approximately 2.5mm before the specimen fractured. There is evidence of a pre-existing fault and the higher magnification images show small defects at the extreme tip of the countersink.

Figure B-3: Specimen#2-Fracture Surface (1 to 3 microns)

Specimen#3

1 Micron
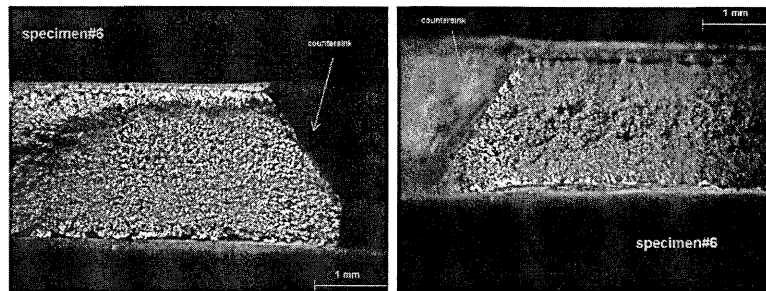

1.5 Micron

2 Micron

3 Micron

Specimen#3 (8-Rivets) took 23434 constant amplitude test cycles to fail at a maximum load of 3.7KN (R=0.2). The fatigue crack initiated at the tip of the countersink and propagated to approximately 3mm before the specimen fractured. There is evidence of a pre-existing fault along the edge of the countersink.

Figure B-4: Specimen#3-Fracture Surface (1 to 3 microns)

Specimen#4

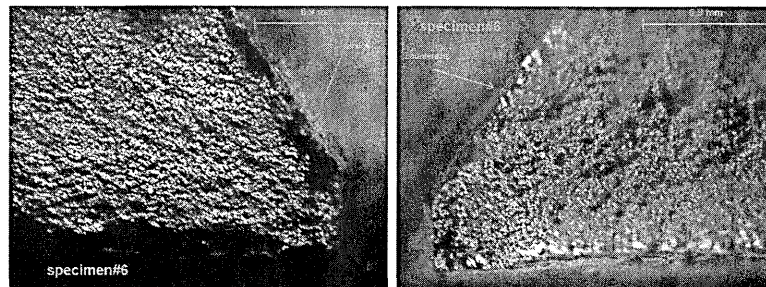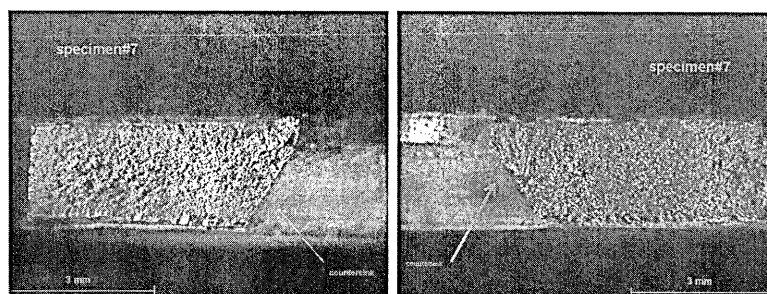**1 Micron**

1.5 Micron

Specimen#4 (6-Rivets) took 36945 constant amplitude test cycles to fail at a maximum load of 3.7KN (R=0.2). The fatigue crack initiated at the tip of the countersink and propagated to approximately 3mm before the specimen fractured. There is evidence of a pre-existing fault at the extreme tip of the countersink.

Figure B-5: Specimen#4-Fracture Surface (1 to 1.5 microns)
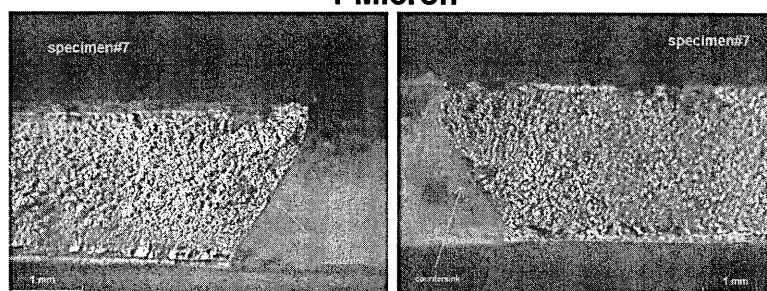
Specimen#5

1 Micron

1.5 Micron

Specimen#5 (8-Rivets) took 83067 constant amplitude test cycles to fail at a maximum load of 3.0KN (R=0.2). The fatigue crack initiated at the tip of the countersink and propagated to approximately 3mm before the specimen fractured. There is evidence of small defects at the extreme tip of the countersink.

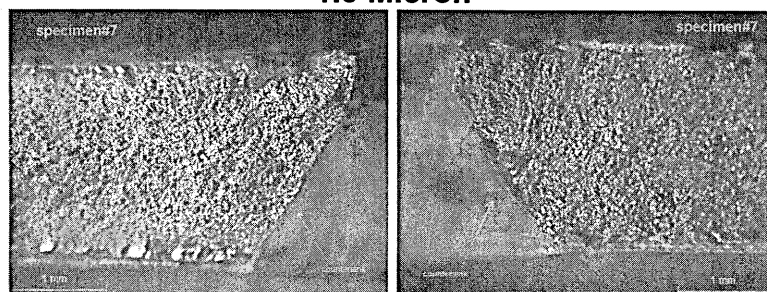**Figure B-6: Specimen#5-Fracture Surface (1 to 1.5 microns)**

Specimen#6

1 Micron

1.5 micron
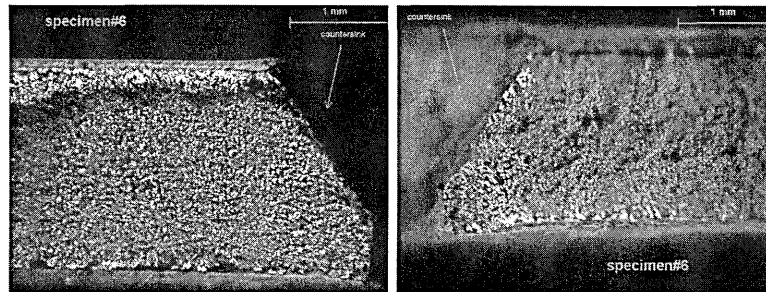
2 Micron

3 Micron

Specimen#6 (8-Rivets) took 113564 constant amplitude test cycles to fail at a maximum load of 3.0KN (R=0.2). The fatigue crack initiated at the tip of the countersink and propagated to approximately 3.5mm before the specimen fractured. At high magnification there is evidence of small defects at the extreme tip of the countersink.

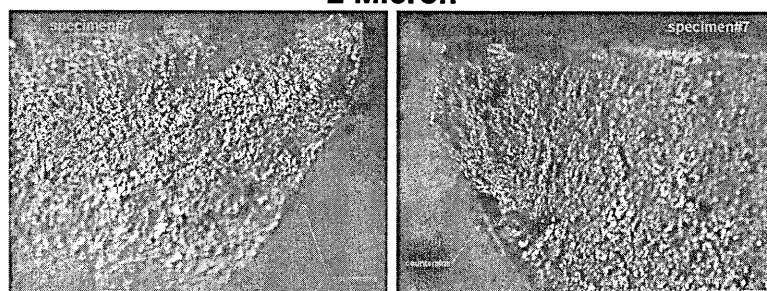**Figure B-7: Specimen#6-Fracture Surface (1 to 3 microns)**

Specimen#7

1 Micron
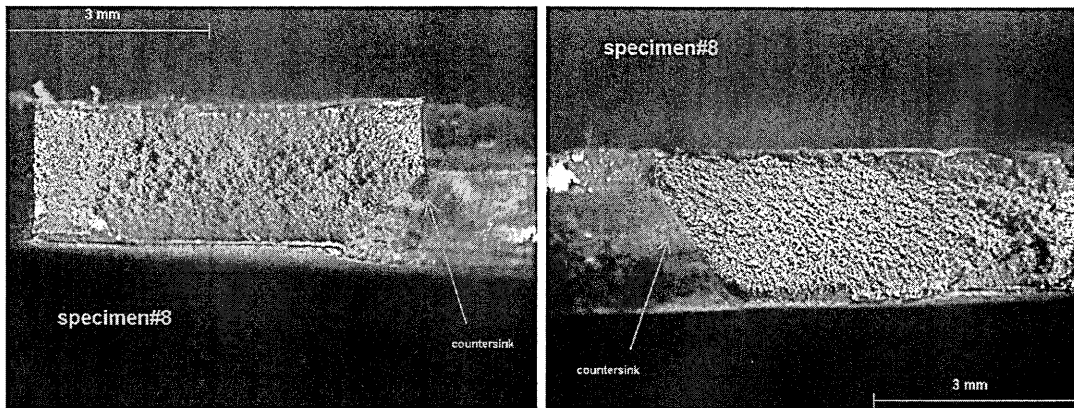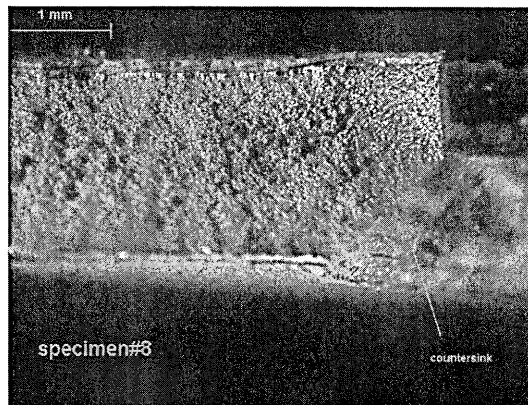
1.5 Micron

2 Micron

3 Micron

Specimen#7 (6-Rivets) took 382080 constant amplitude test cycles to fail at a maximum load of 2.6KN (R=0.2). The fatigue crack initiated at the tip of the countersink and propagated to approximately 4.5mm before the specimen fractured. At high magnification there is evidence of small defects at the extreme tip of the countersink.

Figure B-8: Specimen#7-Fracture Surface (1 to 3 microns)

Specimen#8

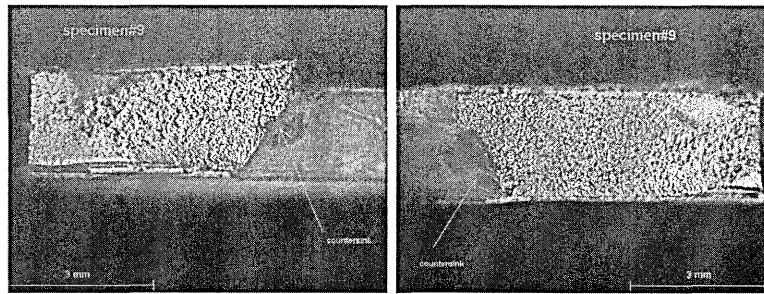**1 Micron**

1.5 Micron

2 Micron

Specimen#8 (8-Rivets) took 147549 constant amplitude test cycles to fail at a maximum load of 2.6KN (R=0.2). The fatigue crack initiated at the tip of the countersink and propagated to approximately 4.5mm before the specimen fractured.

Figure B-9: Specimen#8-Fracture Surface (1 to 2 microns)

Specimen#9

1 Micron

1.5 Micron

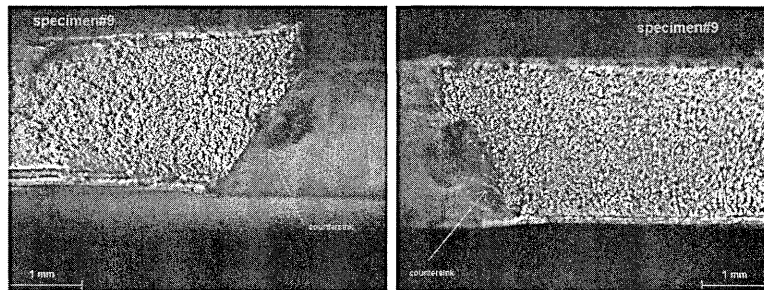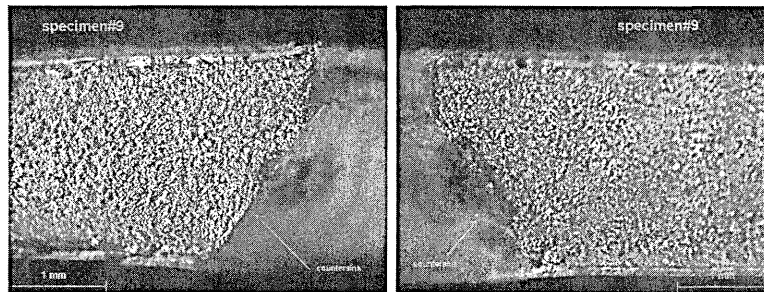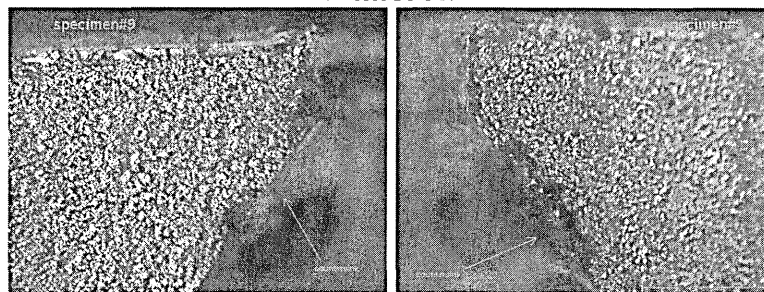

2 Micron

3 Micron

Specimen#9 (6-Rivets) took 341773 constant amplitude test cycles to fail at a maximum load of 2.6KN (R=0.2). The fatigue crack initiated at the tip of the countersink and propagated to approximately 4.5mm before the specimen fractured. At high magnification there is evidence of small defects at the extreme tip and edge of the countersink. This specimen was selected for further examination using a SEM

Figure B-10: Specimen#9-Fracture Surface (1 to 3 microns)

Specimen#10

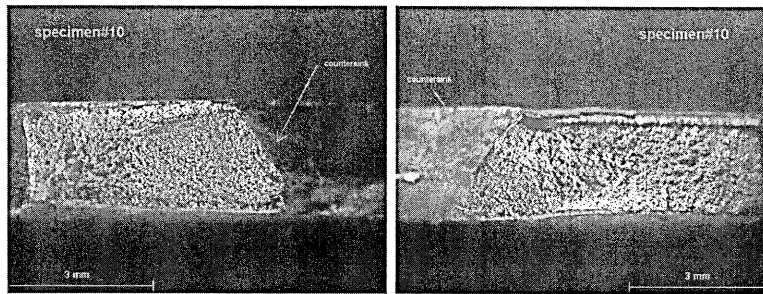**1 Micron**

1.5 Micron

2 Micron

3 Micron

Specimen#10 (8-Rivets) took 62768 constant amplitude test cycles to fail at a maximum load of 3.3KN (R=0.2). The fatigue crack initiated at the tip of the countersink and propagated to approximately 3mm before the specimen fractured. At high magnification there is evidence of small defects at the extreme tip and edge of the countersink. This specimen was selected for further examination using a SEM

Figure B-11: Specimen#10-Fracture Surface (1 to 3 microns)

Specimen#11

1 Micron

1.5 Micron
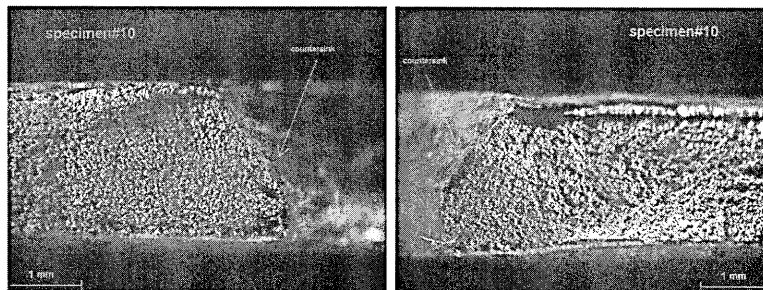
2 Micron

3 Micron

Specimen#11 (8-Rivets) took 88930 constant amplitude test cycles to fail at a maximum load of 3.0KN (R=0.2). The fatigue crack initiated at the tip of the countersink and propagated to approximately 3.5mm before the specimen fractured. At high magnification there is evidence of small defects at the extreme tip of the countersink. This specimen was selected for further examination using a SEM

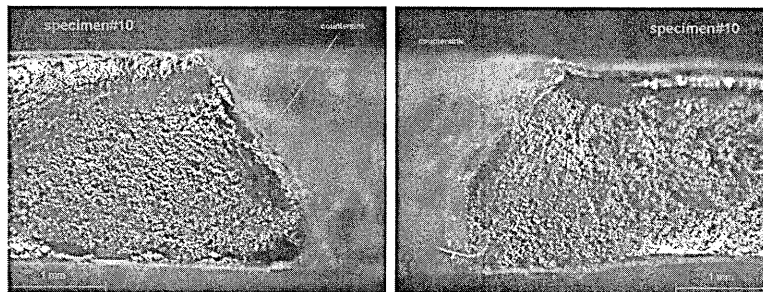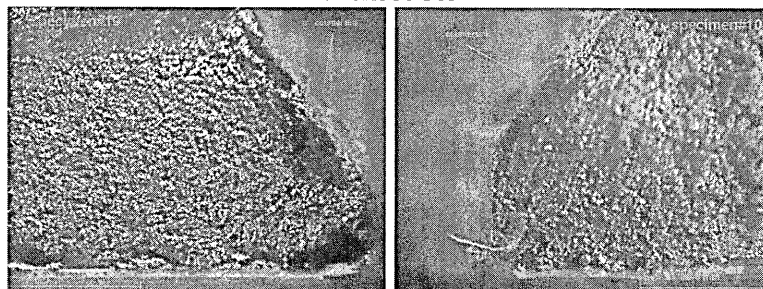**Figure B-12: Specimen#11-Fracture Surface (1 to 3 microns)**

Specimen#12

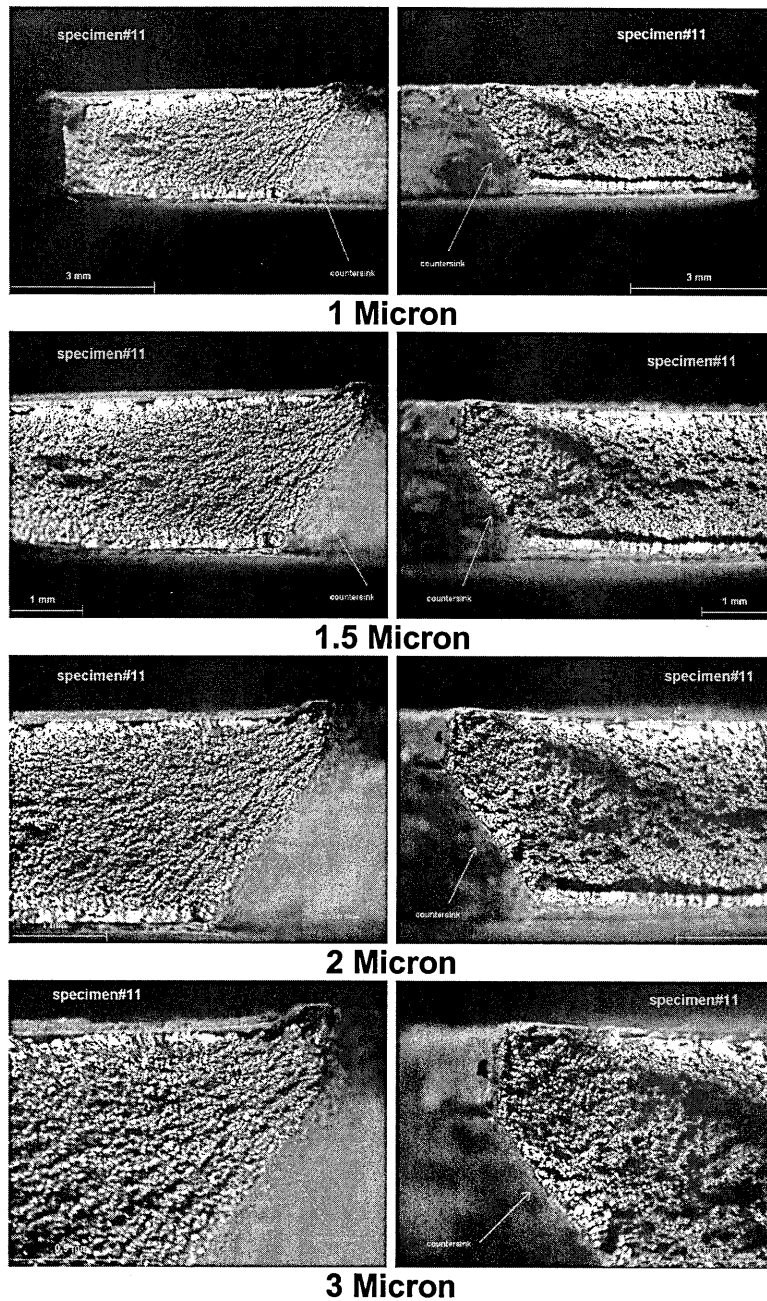**1 Micron**

1.5 Micron

2 Micron

3 Micron

Specimen#12 (6-Rivets) took 162973 constant amplitude test cycles to fail at a maximum load of 3.0KN (R=0.2). The fatigue crack initiated at the tip of the countersink and propagated to approximately 3.5mm before the specimen fractured. At high magnification there is evidence of small defects at the extreme tip and edge of the countersink.

Figure B-13: Specimen#12-Fracture Surface (1 to 3 microns)

Specimen#13

1 Micron

1.5 Micron

2 Micron

3 Micron
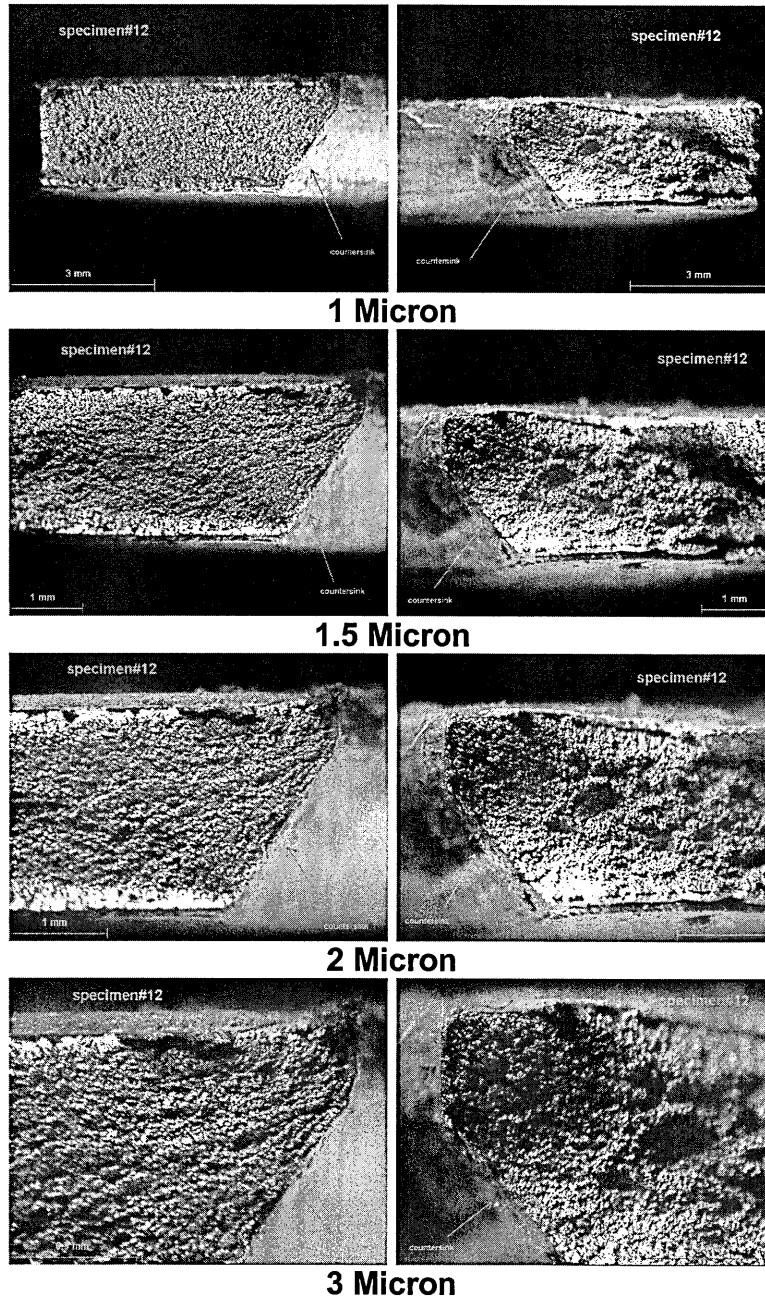
Specimen#13 (8-Rivets) took 47653 constant amplitude test cycles to fail at a maximum load of 3.0KN (R=0.2). The fatigue crack initiated at the tip of the countersink and propagated to approximately 3mm before the specimen fractured. At high magnification there is evidence of small defects at the extreme tip of the countersink.

Figure B-14: Specimen#13-Fracture Surface (1 to 3 microns)

Specimen#14

Not Tested

Figure B-15: Specimen#14-Not Tested

Specimen#15
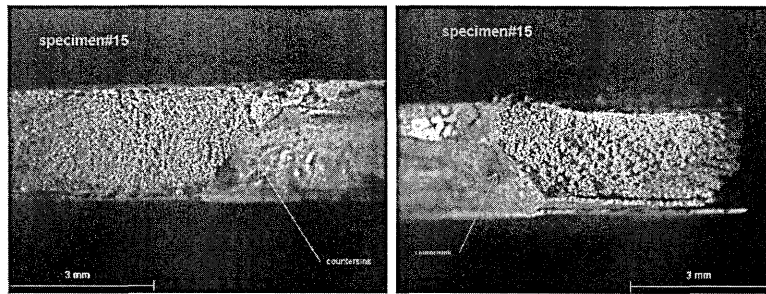
1 Micron
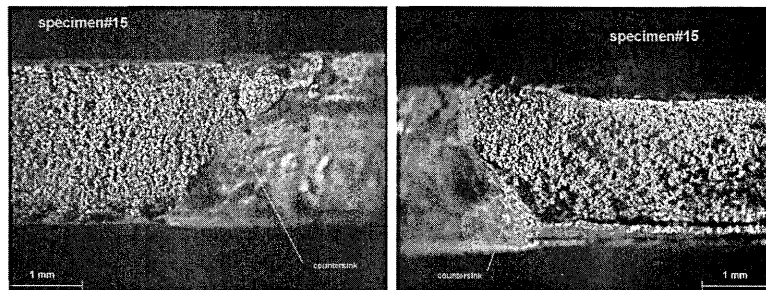
1.5 Micron
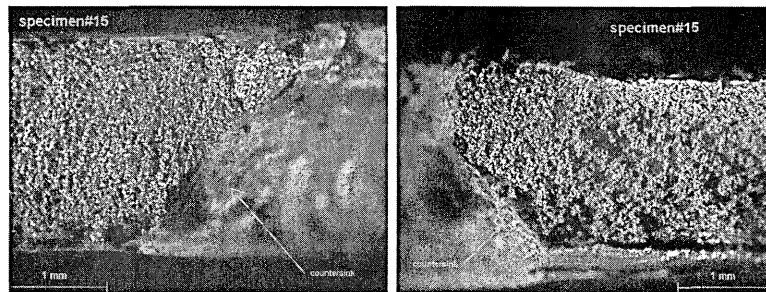
2 Micron

3 Micron

Specimen#15 (8-Rivets) took 494720 constant amplitude test cycles to fail at a maximum load of 2.6KN (R=0.2). The fatigue crack initiated at the tip of the countersink and propagated to approximately 4.5mm before the specimen fractured. At high magnification there is evidence of a pre-existing defect at the extreme tip of the countersink. This specimen was selected for further examination using a SEM

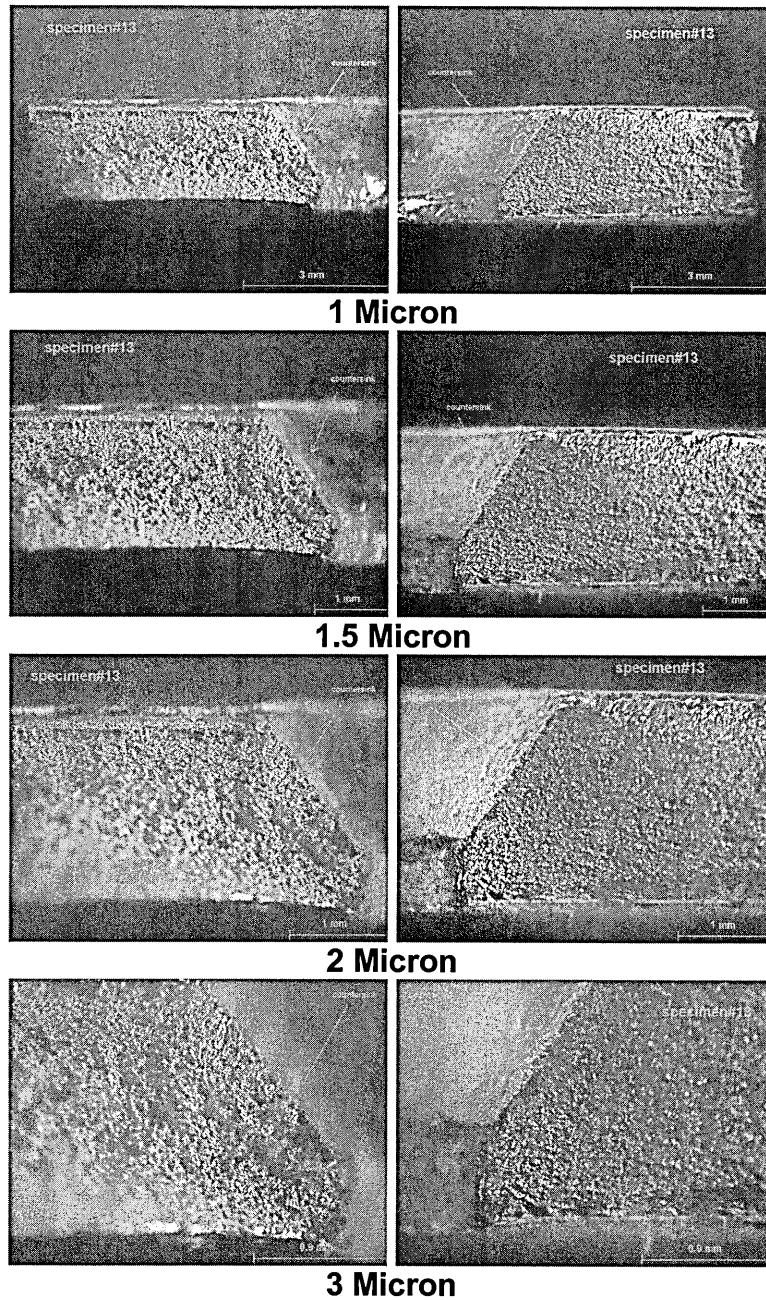**Figure B-16: Specimen#15-Fracture Surface (1 to 3 microns)**

Specimen#16

1 Micron

1.5 Micron

2 Micron

3 Micron

Specimen#16 (8-Rivets) took 55621 constant amplitude test cycles to fail at a maximum load of 3.3KN (R=0.2). The fatigue crack initiated at the tip of the countersink and propagated to approximately 3.5mm before the specimen fractured. At high magnification there is evidence of small defects at the extreme tip and edge of the countersink.

Figure B-17: Specimen#16-Fracture Surface (1 to 3 microns)

Specimen#17

1 Micron

1.5 micron

2 Micron

3 Micron

Specimen#17 (6-Rivets) took 223780 constant amplitude test cycles to fail at a maximum load of 3.0KN (R=0.2). The fatigue crack initiated at the tip of the countersink and propagated to approximately 3.5mm before the specimen fractured. At high magnification there is evidence of small defects at the extreme tip and edge of the countersink.

**Figure B-18: Specimen#17-Fracture Surface (1 to 3 microns)**

Specimen#18

Test not completed

Figure B-19: Specimen#18-Test Not Completed
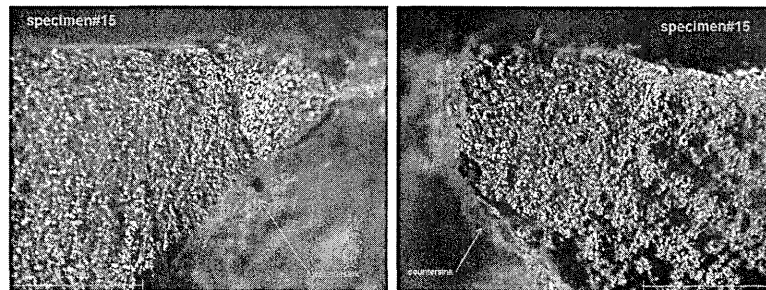
Specimen#19
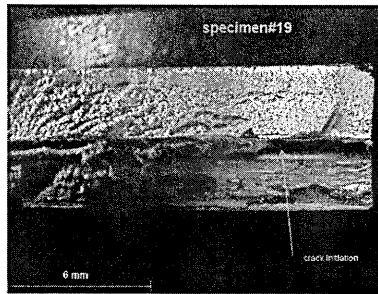
0.5 Micron
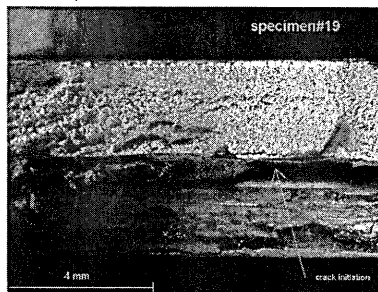
0.75 micron

1 Micron

1.5 Micron

Specimen#19 (6-Rivets) took 167923 constant amplitude test cycles to fail at a maximum load of 3.0KN (R=0.2). This specimen failed along the butt strap at the centre of the butt joint where the 2 skins meet. The fatigue crack initiated at the edge of the surface where at high magnification there is evidence of a small defect on the surface of the butt strap.

Figure B-20: Specimen#19-Fracture Surface (0.5 to 1.5 microns)

Specimen#20

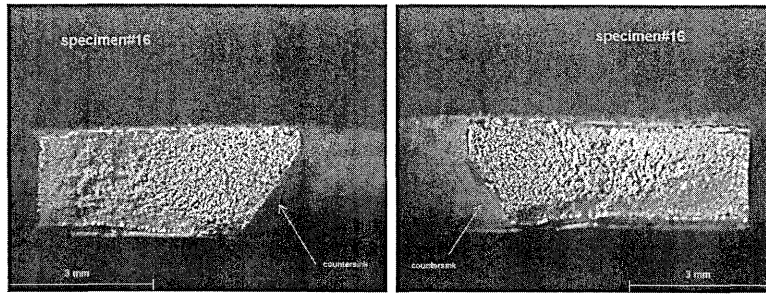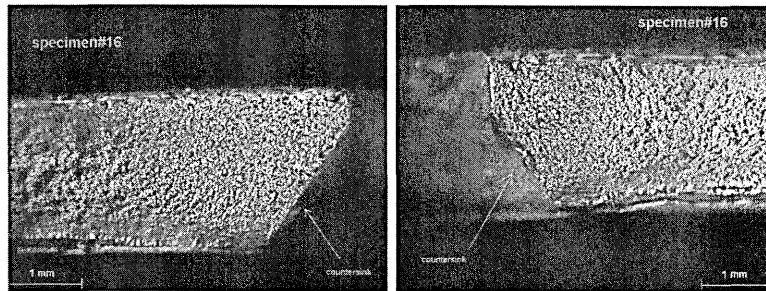

1 Micron

1.5 Micron

2 Micron

3 Micron

Specimen#20 (8-Rivets) took 83094 constant amplitude test cycles to fail at a maximum load of 3.0KN (R=0.2). The fatigue crack initiated at the tip of the countersink and propagated to approximately 3.5mm before the specimen fractured. At high magnification there is evidence of small defects at the extreme tip and edge of the countersink.

Figure B-21: Specimen#20-Fracture Surface (1 to 3 microns)
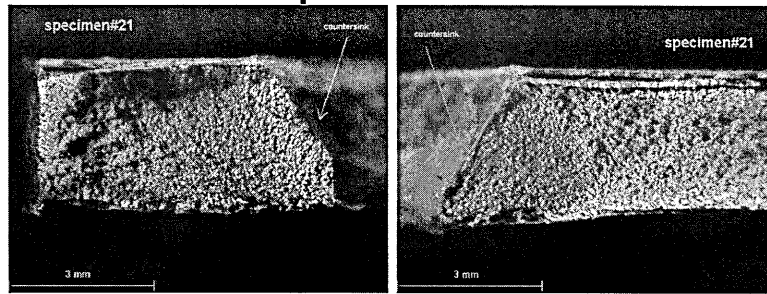
Specimen#21

1 Micron
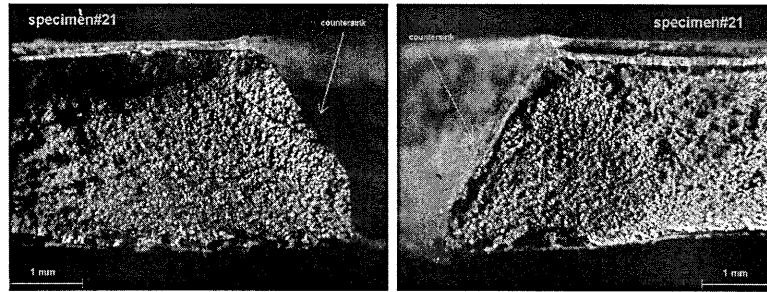
1.5 Micron
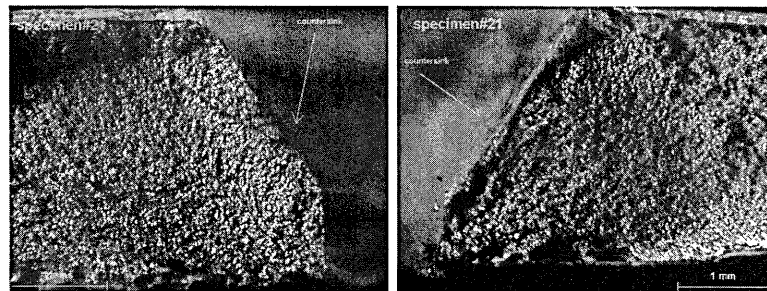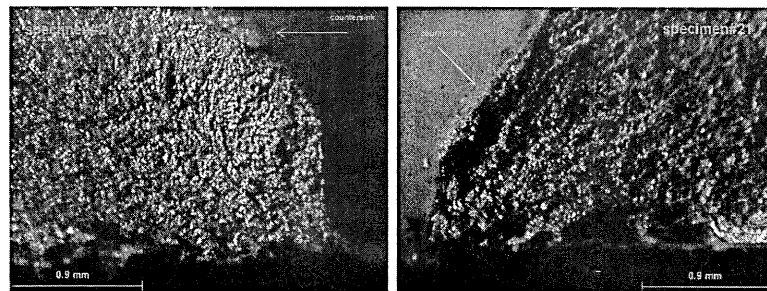
2 Micron

3 Micron

Specimen#21 (8-Rivets) took 103485 constant amplitude test cycles to fail at a maximum load of 3.0KN (R=0.2). The fatigue crack initiated at the tip of the countersink and propagated to approximately 3.5mm before the specimen fractured. At high magnification there is evidence of small defects at the extreme tip and edge of the countersink. This specimen was selected for further examination using a SEM

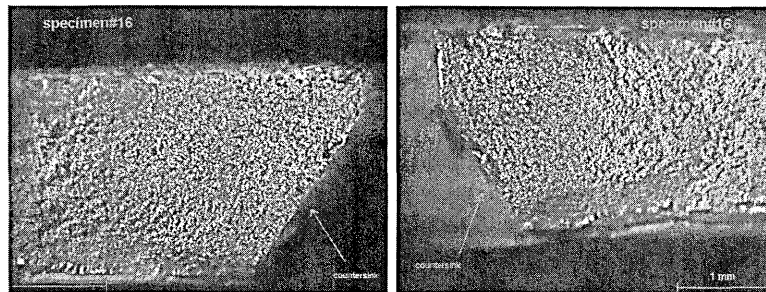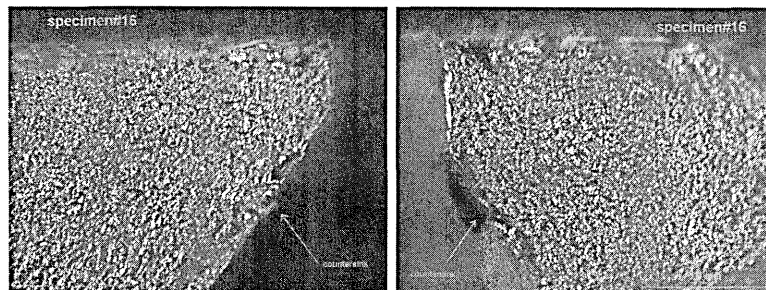**Figure B-22: Specimen#21-Fracture Surface (1 to 3 microns)**

Specimen#22

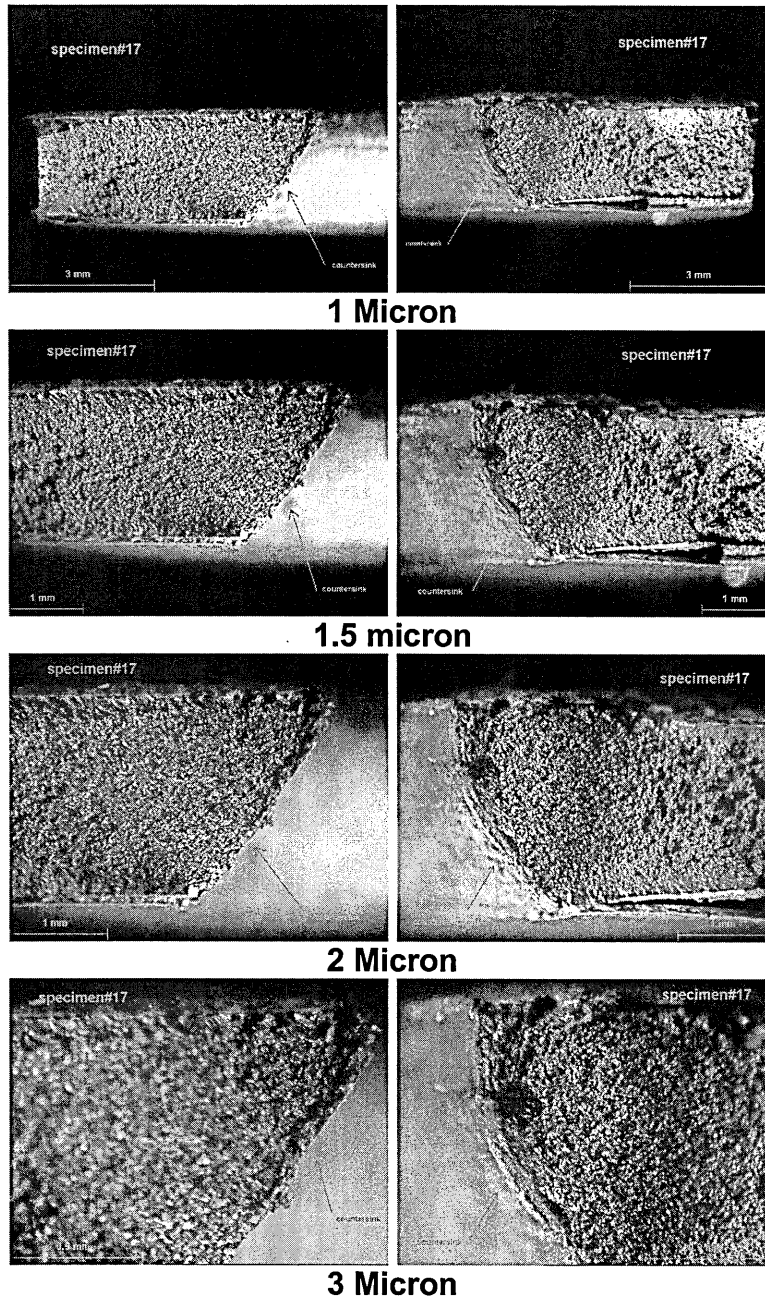
1 Micron

1.5 Micron

2 Micron

3 Micron
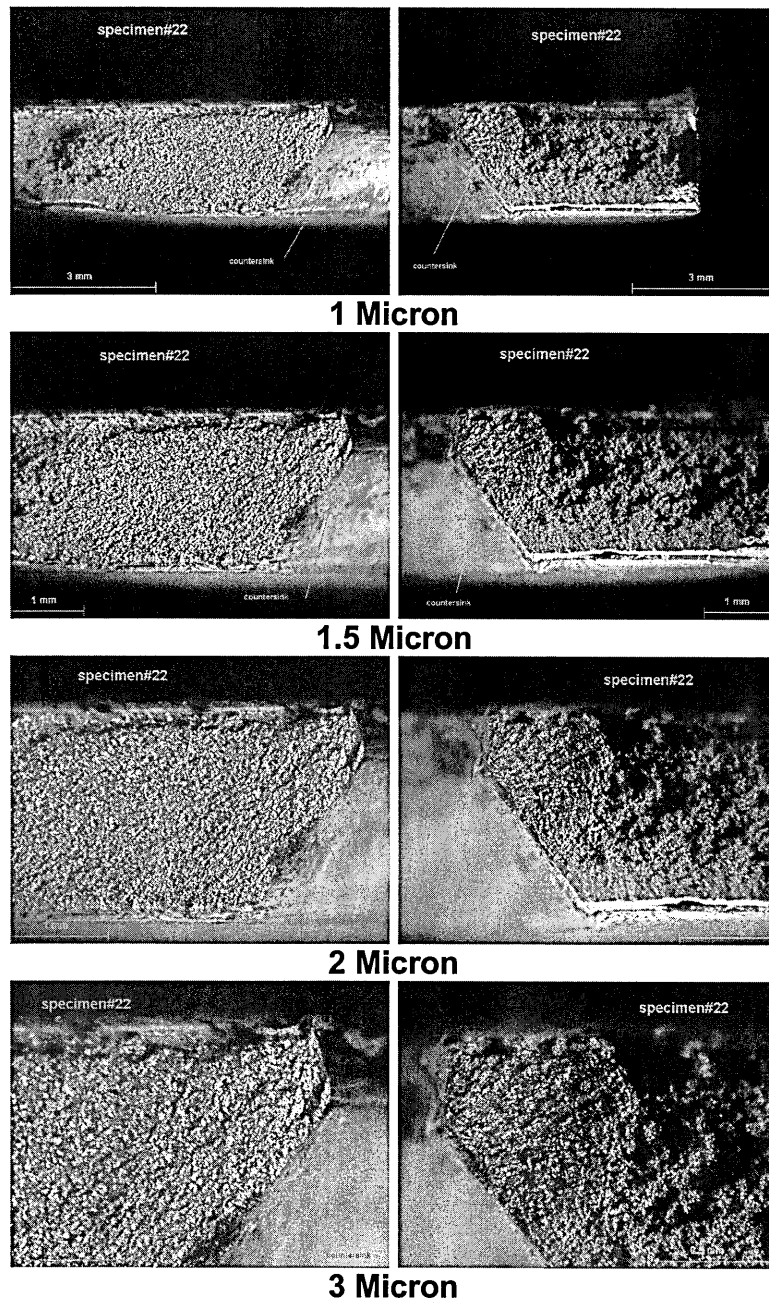
Specimen#22 (6-Rivets) took 209816 constant amplitude test cycles to fail at a maximum load of 3.0KN (R=0.2). The fatigue crack initiated at the tip of the countersink and propagated to approximately 4mm before the specimen fractured. At high magnification there is evidence of small defects at the extreme tip and edge of the countersink.

Figure B-23: Specimen#22-Fracture Surface (1 to 3 microns)

Specimen#23

1 Micron

1.5 Micron

2 Micron

3 Micron
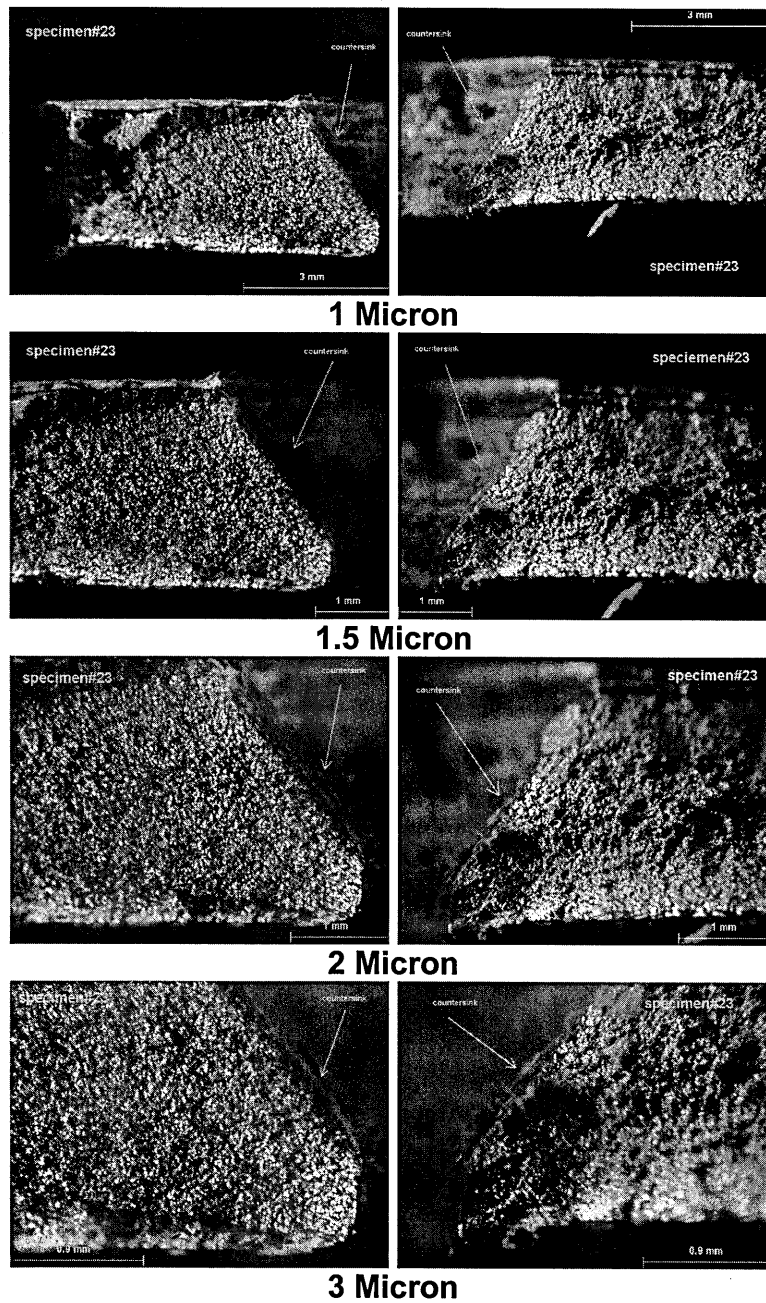
Specimen#23 (8-Rivets) took 89298 constant amplitude test cycles to fail at a maximum load of 3.0KN (R=0.2). The fatigue crack initiated at the tip of the countersink and propagated to approximately 3.5mm before the specimen fractured. At high magnification there is evidence of small defects at the extreme tip of the countersink and a pre-existing defect along the edge of the countersink. This specimen was selected for further examination using a SEM

Figure B-24: Specimen#23-Fracture Surface (1 to 3 microns)
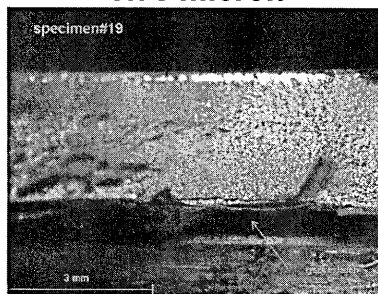
Specimen#24
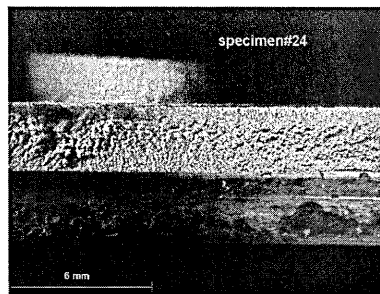
0.5 Micron
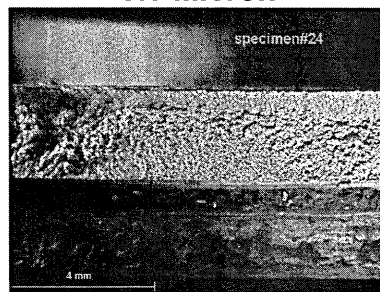
0.75 Micron
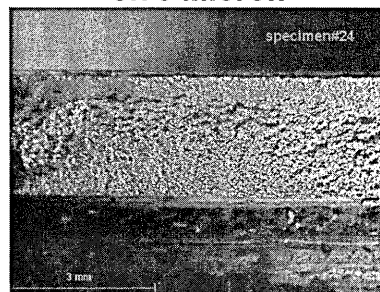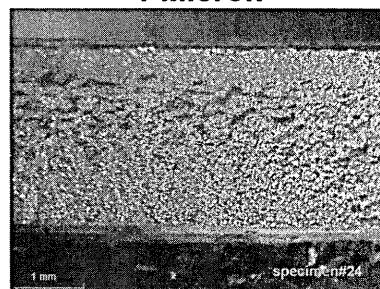
1 Micron

1.5 Micron

Specimen#24 (6-Rivets) took 100057 constant amplitude test cycles to fail at a maximum load of 3.0KN (R=0.2). This specimen failed along the butt strap at the centre of the butt joint where the 2 skins meet. The fatigue crack initiated along the edge of the surface where at high magnification there is evidence of a small cut along the surface of the butt strap.

Figure B-25: Specimen#24-Fracture Surface (0.5 to 1.5 microns)
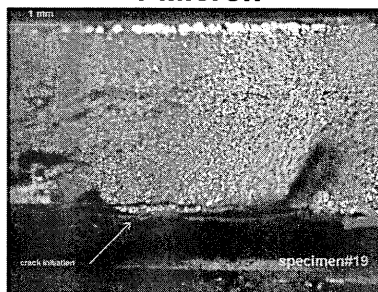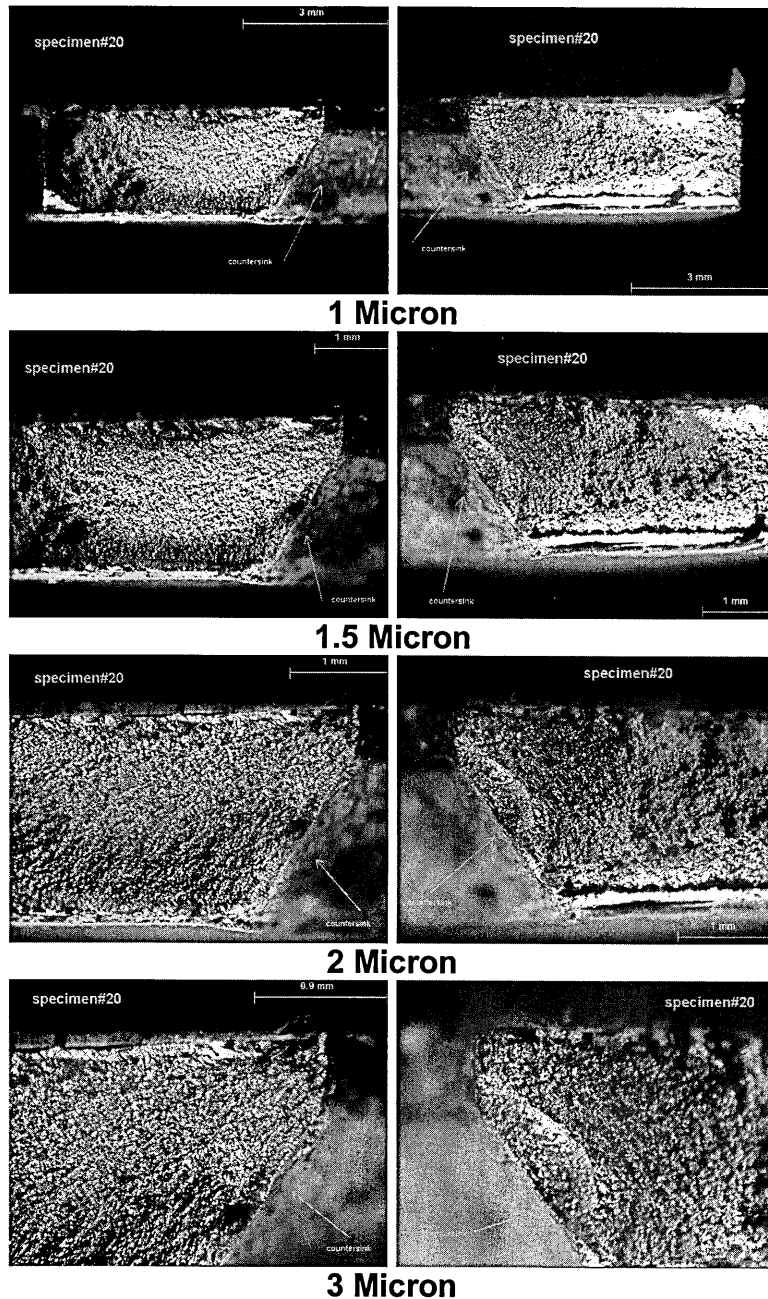
Specimen#25

1 Micron

1.5 Micron

2 Micron

3 Micron
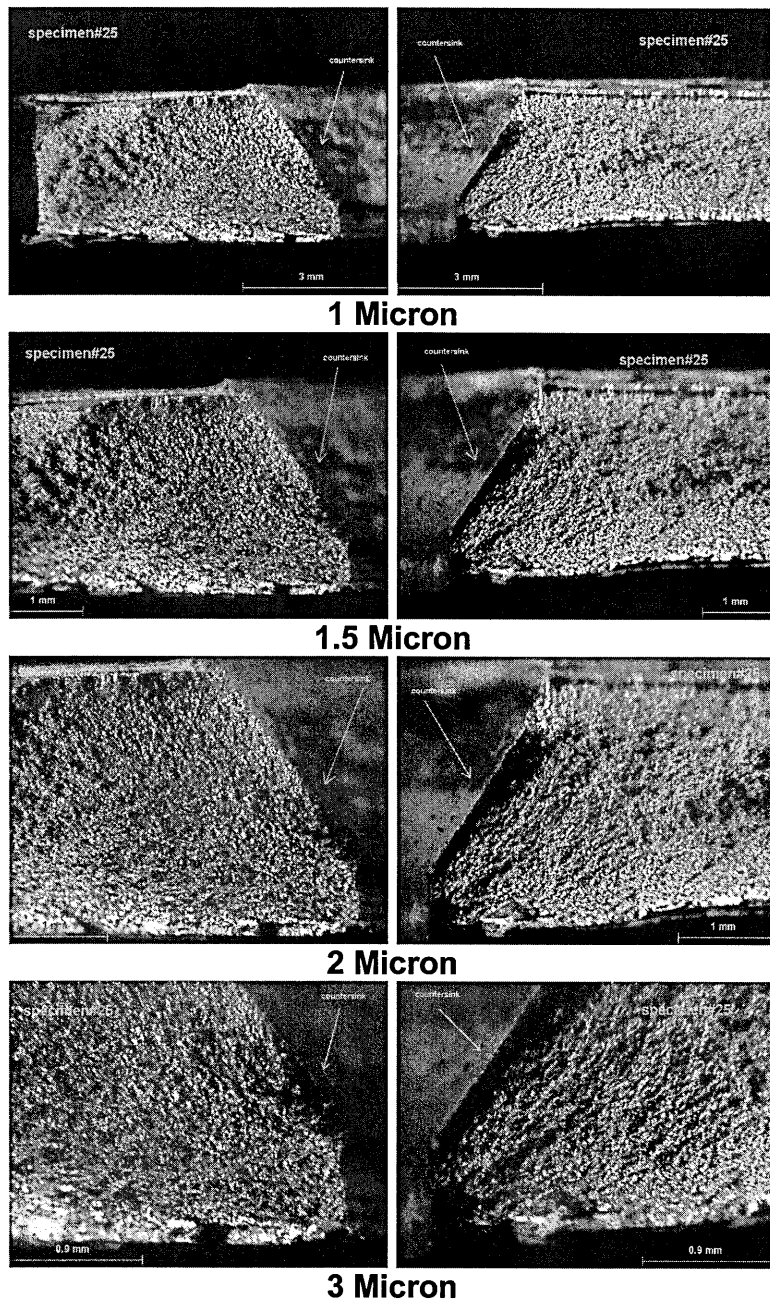
Specimen#25 (8-Rivets) took 50168 constant amplitude test cycles to fail at a maximum load of 3.0KN (R=0.2). The fatigue crack initiated at the tip of the countersink and propagated to approximately 4mm before the specimen fractured. At high magnification there is evidence of small defects at the extreme tip and edge of the countersink

Figure B-26: Specimen#25-Fracture Surface (1 to 3 microns)

Scanning Electron Microscope Analysis

Specimen#9
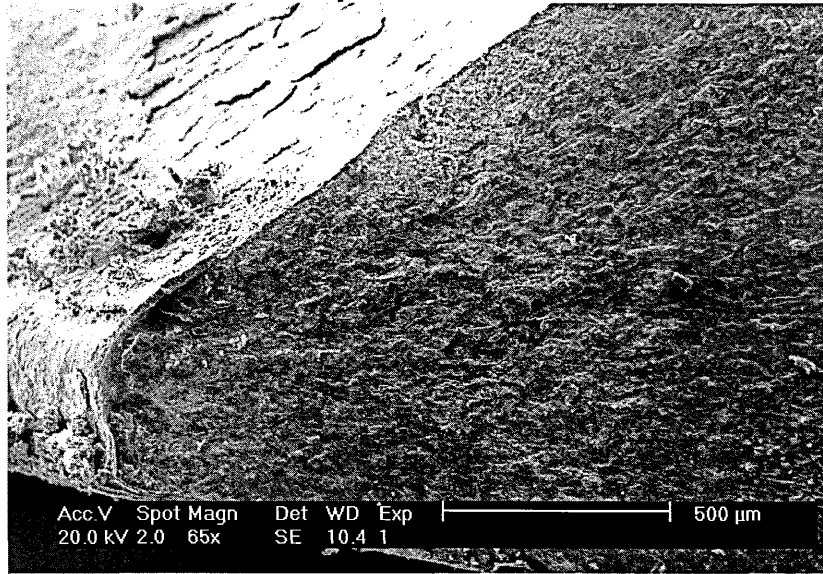
(a)
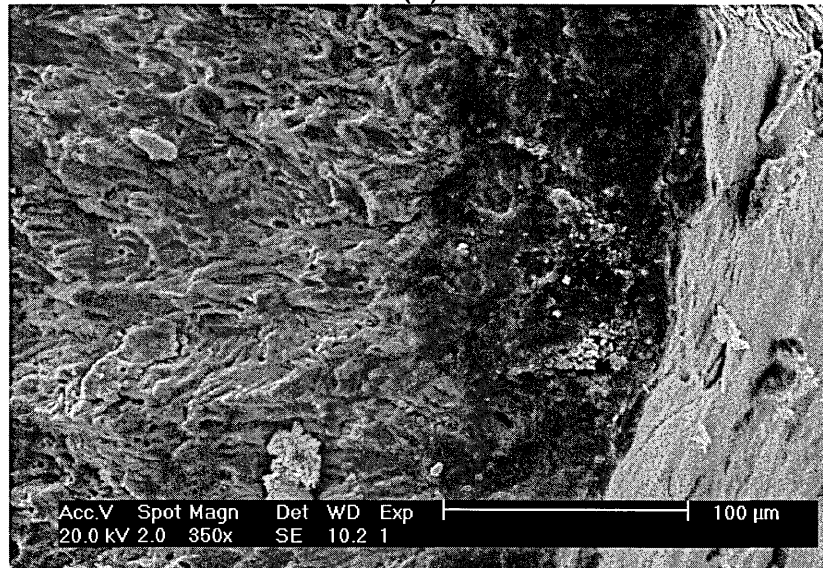
(c)

(a) Small defect on the edge of the countersink, possibly a corrosion pit, with evidence of fatigue cracking around the defect. Possible simultaneous initiation of fatigue crack from the tip of countersink and the defect. Corrosion pitting was evident on the surface of the countersink.

(b) The other side of the countersink had clear evidence of corrosion pitting and fatigue cracking at these sites. Possible simultaneous initiation of fatigue crack from tip of countersink and sites of corrosion pitting.

Figure B-27: Specimen#9-SEM Fracture Surfaces

Specimen#10
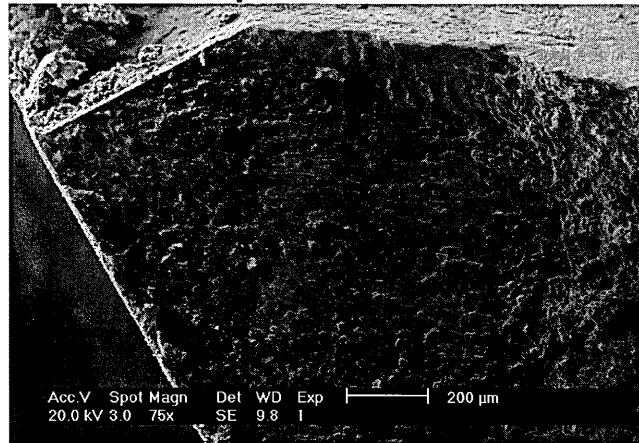
(a)
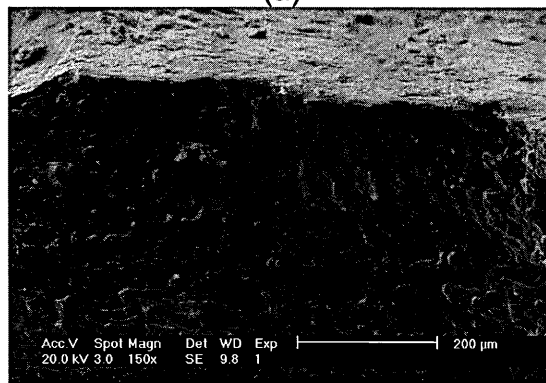
(b)
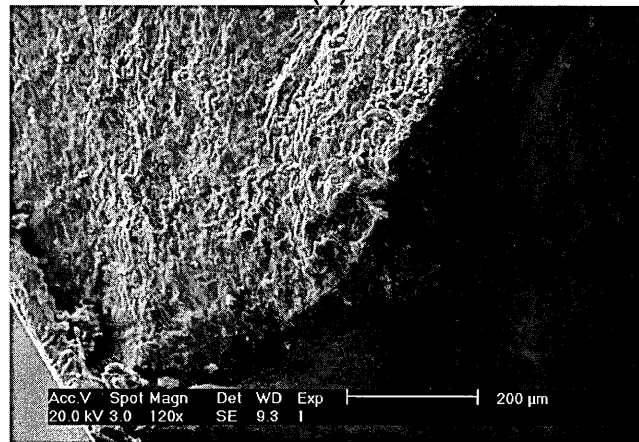
(c)

(a) Evidence of corrosion pitting along the edge of the countersink and a pre-existing fatigue crack. Possible simultaneous initiation of fatigue crack from site of corrosion pits and the tip of the countersink. (b) A closer look at the site of corrosion pitting. (c) The other side of the countersink showed evidence of further corrosion pitting at the extreme tip of the countersink

Figure B-28: Specimen#10-SEM Fracture Surfaces

Specimen#11
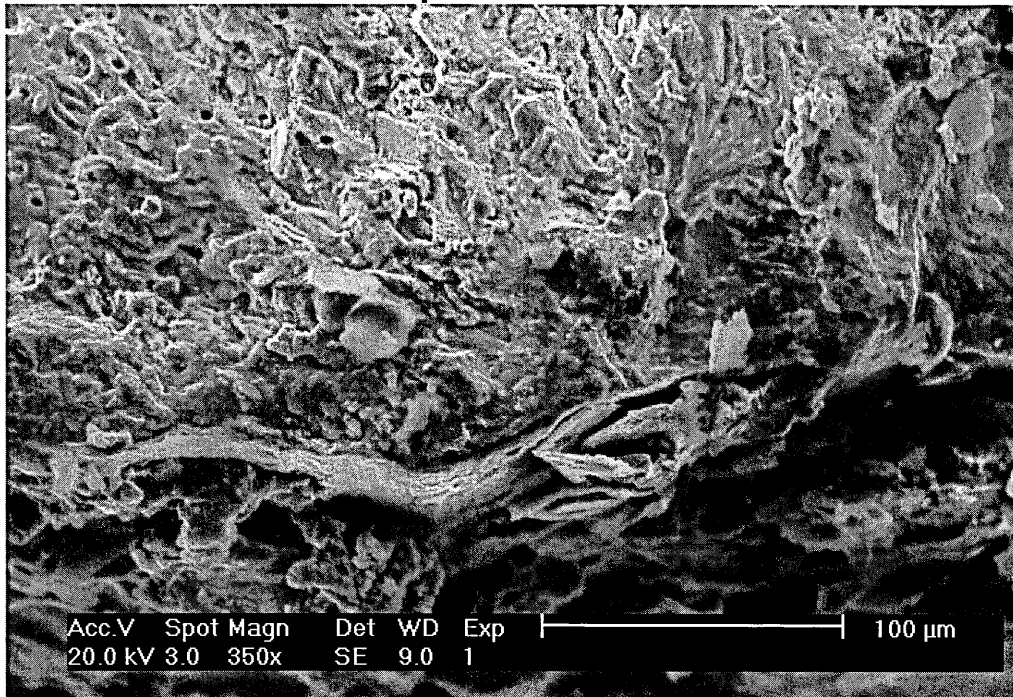
(a)
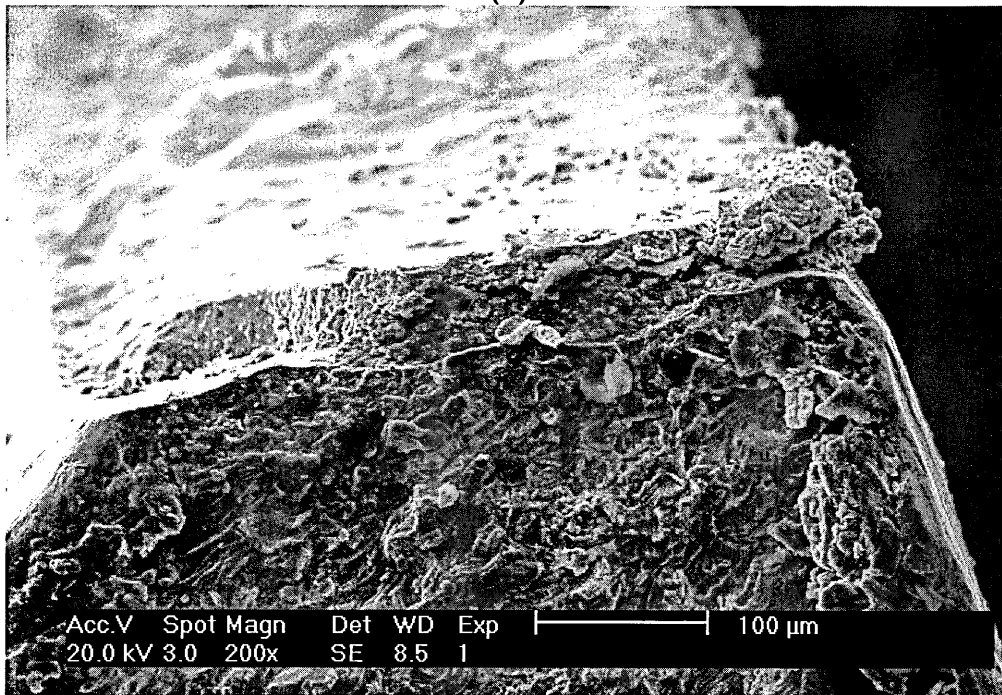
(b)

(a) A close up of the tip of the countersink where there is evidence of a pre-existing defect. (b) The other side of the countersink had evidence of corrosion pitting on the countersink and another pre-existing fatigue crack along the tip of the countersink

Figure B-29: Specimen#11-SEM Fracture Surfaces

Specimen#15

Acc.V Spot Magn Det WD Exp 200 µm
20.0 kV 3.0 120x SE 11.9 1

(a)

Acc.V Spot Magn Det WD Exp 200 µm
20.0 kV 3.0 100x SE 9.9 1
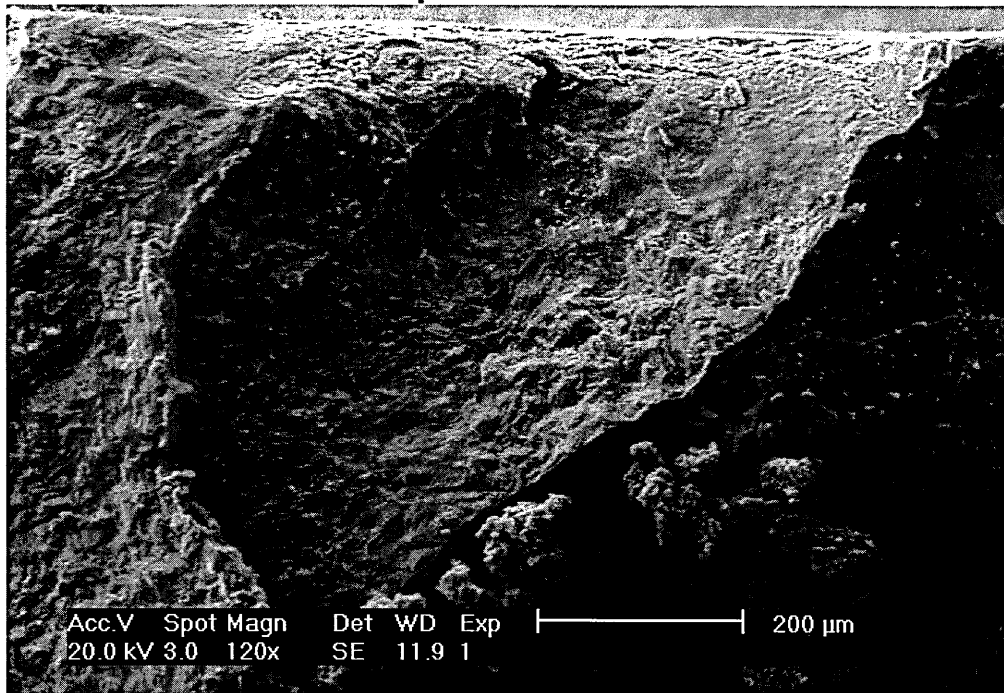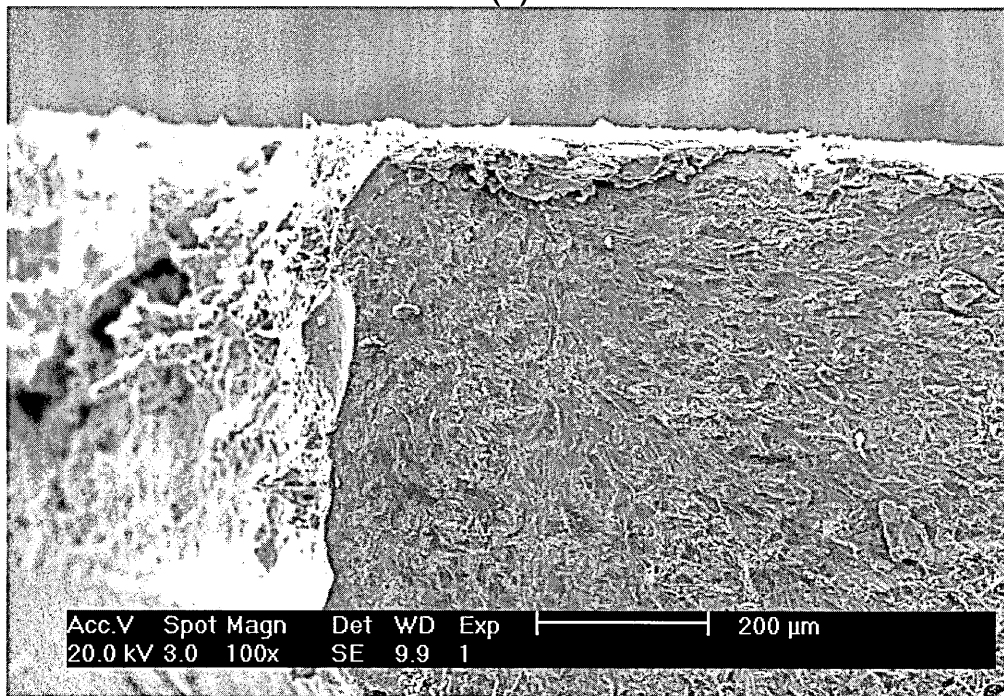
(b)

(a) Pre-existing defect at the extreme tip of the countersink and evidence of corrosion pitting. (b) The other side of the countersink had a small defect at the tip of the countersink but no signs of a pre-existing fatigue crack.

Figure B-30: Specimen#15-SEM Fracture Surfaces
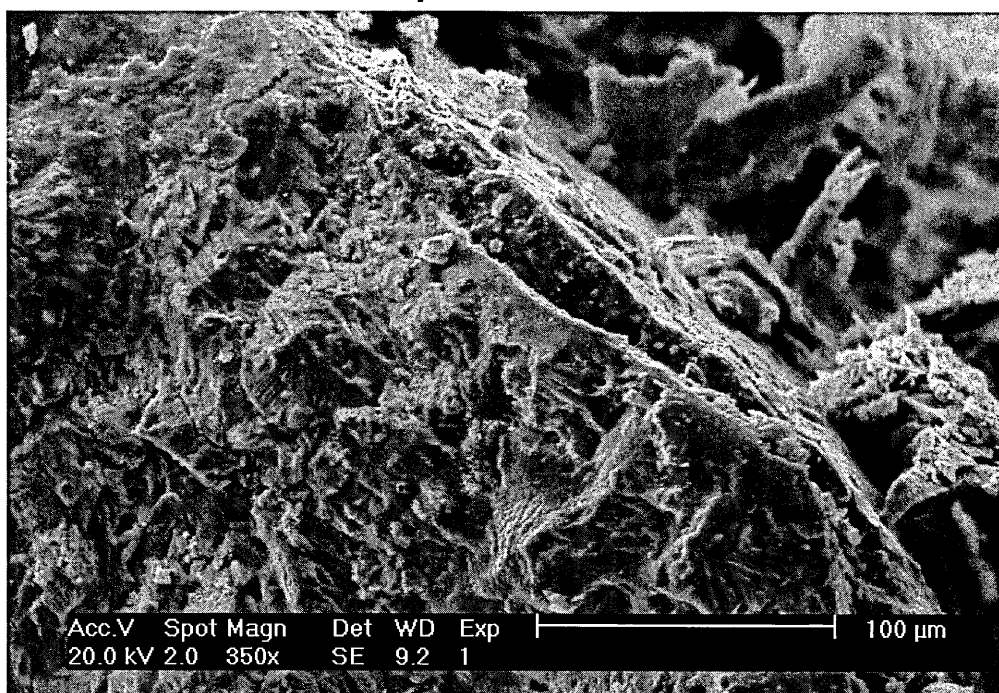
(a)
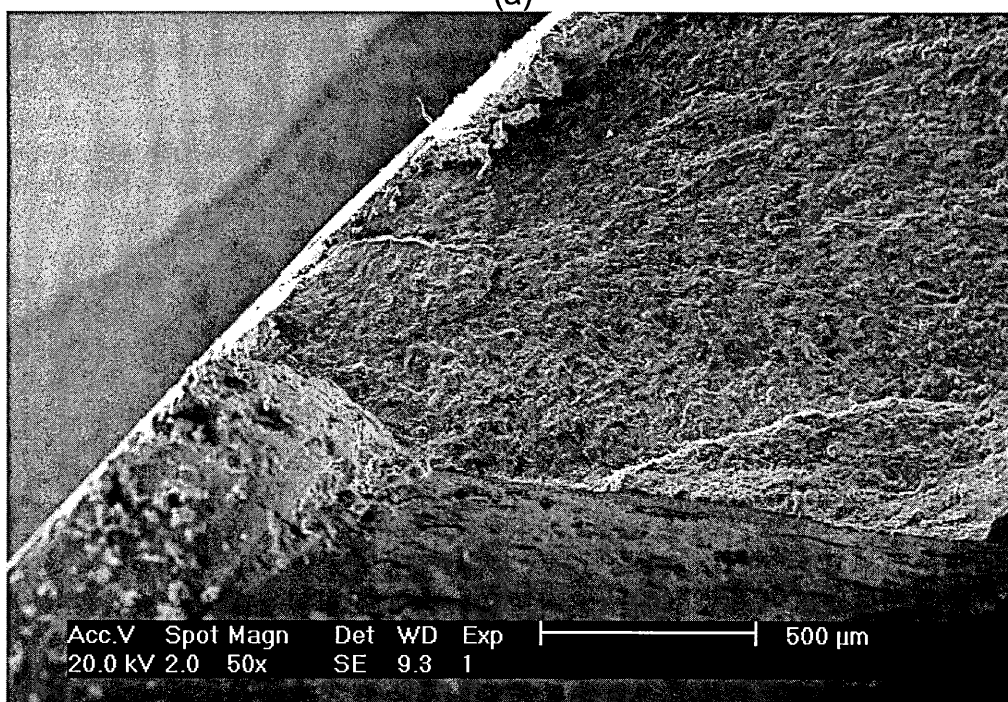
(b)

(a) Signs of corrosion pitting and a pre-existing crack at the tip of the countersink. Possible simultaneous initiation of crack growth at pre-existing defect and the tip of countersink. (b) The other side of the countersink had evidence of crack growth along 3 different planes. No evidence of corrosion pitting was found on the countersink.

Figure B-31: Specimen#21-SEM Fracture Surfaces
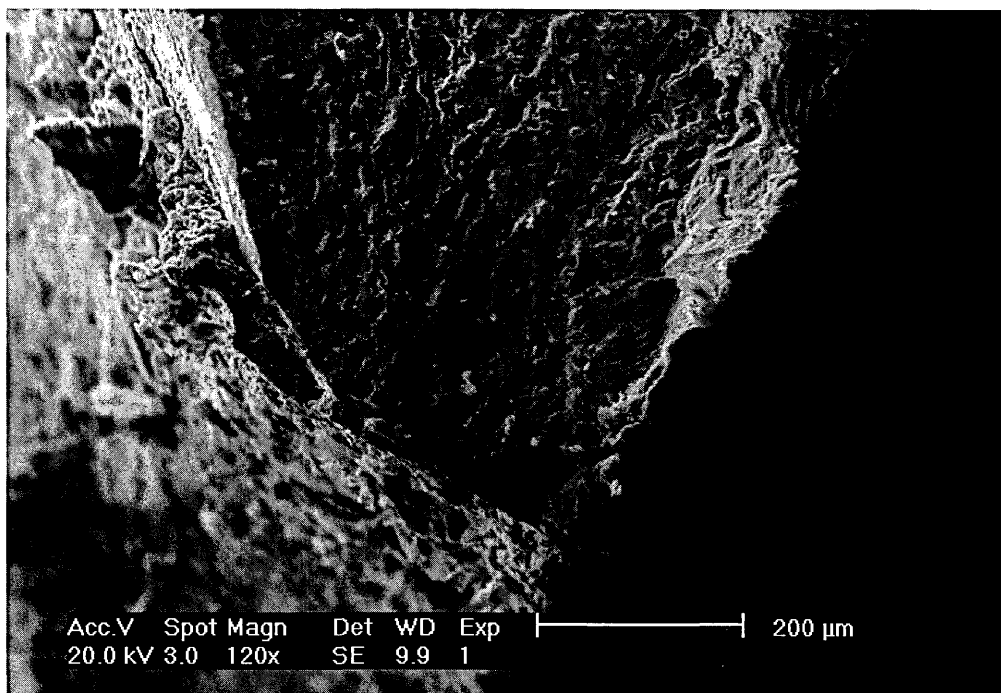
(a)
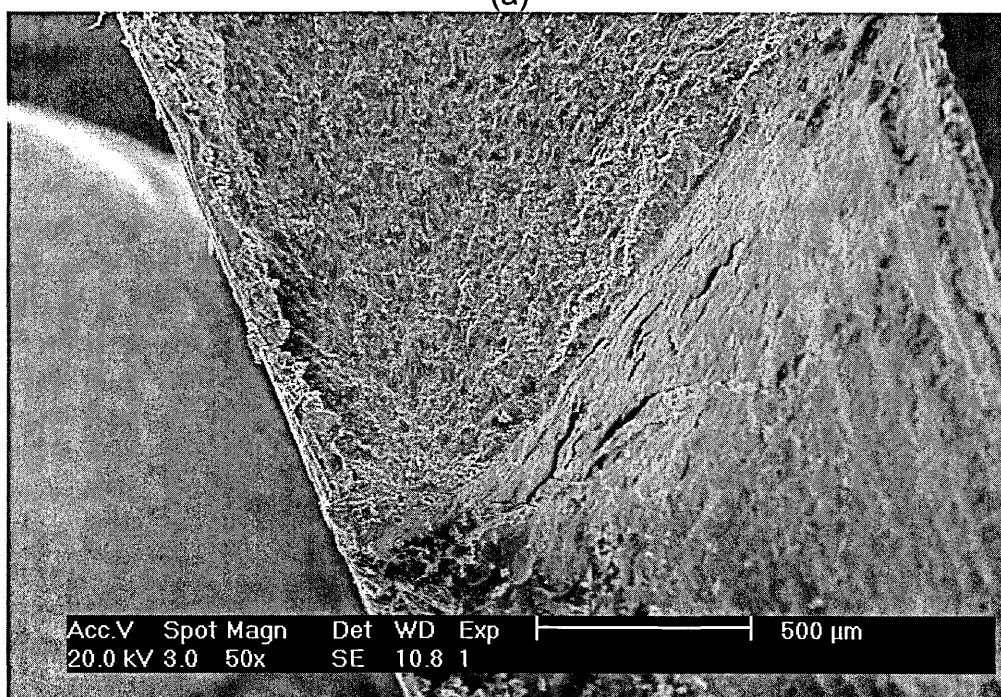
(b)

(a) Defect at extreme tip of the countersink.
(b) The other side of the countersink had little evidence of corrosion pitting but there was evidence of a pre-existing defect along the edge of the countersink.

Figure B-32: Specimen#23-SEM Fracture Surfaces

APPENDIX C – Biaxial Fatigue Calculations

C-1 Cyclic Material Constants

Cyclic material constants for aluminium alloy 2024 –T3 with a crack initiation of 0.5mm were obtained from Reference 33 as follows:

$$R'_{p0.2} = 456MN/m^2$$

$$\sigma_g = 185MN/m^2$$

$$\varepsilon_g = 0.248\%$$

$$N_T = 1614cylces$$

$$T_\sigma = 1.331$$

$$T_{\varepsilon p} = 2.646$$

$$K' = 590MN/m^2$$

$$n' = 0.040$$

$$\sigma'_f = 1044MN/m^2$$

$$\varepsilon'_f = 1.765$$

$$b = -0.114$$

$$c = -0.927$$

C-2 Applied, Shear & Normal Strain Calculations

strain calculations

	gross	bearing			9.71	66948.12
longitudinal max	1.08E+08	1.998E+08			74	1.8796
longitudinal min	2.29E+07	4.237E+07	2.34E-03	1.83E-03	4.17E-03
hoop	6.88E+07	3.018E+07			

minimum biaxial case (using bearing principal stresses)

sigma 1 4.24E+07 **sigma 2** 3.02E+07

epsilon 1 4.38E-04

epsilon 2 2.19E-04

epsilon 3 -3.23E-04

max shear strain (min case)/2 3.807E-04

epsilon normal (min case)/2 2.861E-05

maximum biaxial case (using bearing principal stresses)

sigma 1 1.998E+08 **sigma 2** 3.018E+07

epsilon 1 2.57E-03

epsilon 2 -4.83E-04

epsilon 3 -1.026E-03

max shear strain (max case)/2 1.796E-03

epsilon normal (max case)/2 3.850E-04

deltas

delta max shear starin/2 1.415E-03

delta epsilon normal/2 3.564E-04

1.771E-03

uniaxial case - normal

sigma 1 max	1.998E+08
sigma 1 min	4.237E+07
epsilon 1 max	2.700E-03
epsilon 1 min	5.725E-04

delts epsilon/2   1.064E-03

uniaxial case - shear strain version

shear strain (max case)/2   1.796E-03

shear strain (min case)/2   3.807E-04

delta max shear strain/2   1.415E-03

C-3   Uniaxial Applied Strain Life Equation Solution

UNIAXIAL (conventional)

		Nf	2Nf	C	D	C+D
A'	0.001946	1000	2000	0.000818	0.001537	0.002355
		1100	2200	0.000809	0.001407	0.002216
B'	1.765	1200	2400	0.000801	0.001298	0.002099
		1300	2600	0.000794	0.001205	0.001999
		1400	2800	0.000787	0.001125	0.001913
		1500	3000	0.000781	0.001055	0.001837
		1600	3200	0.000775	0.000994	0.00177
		1700	3400	0.00077	0.00094	0.00171
		1800	3600	0.000765	0.000891	0.001656
		1900	3800	0.00076	0.000848	0.001608
		2000	4000	0.000756	0.000808	0.001564
		2100	4200	0.000752	0.000773	0.001524
		2200	4400	0.000748	0.00074	0.001488
		2300	4600	0.000744	0.00071	0.001454
		2400	4800	0.00074	0.000683	0.001423
		2500	5000	0.000737	0.000657	0.001394
		2600	5200	0.000734	0.000634	0.001368
		2700	5400	0.000731	0.000612	0.001343
		2800	5600	0.000728	0.000592	0.001319
		2900	5800	0.000725	0.000573	0.001297
		3000	6000	0.000722	0.000555	0.001277
		3100	6200	0.000719	0.000539	0.001258
		3200	6400	0.000717	0.000523	0.001239
		3300	6600	0.000714	0.000508	0.001222
		3400	6800	0.000712	0.000494	0.001206
		3500	7000	0.000709	0.000481	0.00119
		3600	7200	0.000707	0.000469	0.001176
		3700	7400	0.000705	0.000457	0.001162
		3800	7600	0.000703	0.000446	0.001149
		3900	7800	0.000701	0.000435	0.001136
		4000	8000	0.000699	0.000425	0.001124
		4100	8200	0.000697	0.000416	0.001112
		4200	8400	0.000695	0.000406	0.001101
		4300	8600	0.000693	0.000398	0.00109
		4400	8800	0.000691	0.000389	0.00108
		4500	9000	0.000689	0.000381	0.00107
		4600	9200	0.000687	0.000374	0.001061
		4700	9400	0.000686	0.000366	0.001052
		4800	9600	0.000684	0.000359	0.001043
		4900	9800	0.000683	0.000352	0.001035
		5000	10000	0.000681	0.000346	0.001027

C-4 Uniaxial Maximum Shear Strain Life Equation Solution

UNIAXIAL (shear strain max)

		Nf	2Nf	C	D	C+D
A'	0.00253	1000	2000	0.001064	0.002306	0.003369
		1100	2200	0.001052	0.002111	0.003163
B'	2.6475	1200	2400	0.001042	0.001947	0.002989
		1300	2600	0.001032	0.001808	0.00284
		1400	2800	0.001024	0.001688	0.002711
		1500	3000	0.001016	0.001583	0.002599
		1600	3200	0.001008	0.001491	0.002499
		1700	3400	0.001001	0.00141	0.002411
		1800	3600	0.000995	0.001337	0.002332
		1900	3800	0.000989	0.001272	0.00226
		2000	4000	0.000983	0.001213	0.002195
		2100	4200	0.000977	0.001159	0.002136
		2200	4400	0.000972	0.00111	0.002082
		2300	4600	0.000967	0.001065	0.002032
		2400	4800	0.000963	0.001024	0.001987
		2500	5000	0.000958	0.000986	0.001944
		2600	5200	0.000954	0.000951	0.001905
		2700	5400	0.00095	0.000918	0.001868
		2800	5600	0.000946	0.000888	0.001833
		2900	5800	0.000942	0.000859	0.001801
		3000	6000	0.000938	0.000833	0.001771
		3100	6200	0.000935	0.000808	0.001743
		3200	6400	0.000931	0.000784	0.001716
		3300	6600	0.000928	0.000762	0.00169
		3400	6800	0.000925	0.000741	0.001667
		3500	7000	0.000922	0.000722	0.001644
		3600	7200	0.000919	0.000703	0.001622
		3700	7400	0.000916	0.000686	0.001602
		3800	7600	0.000913	0.000669	0.001582
		3900	7800	0.000911	0.000653	0.001564
		4000	8000	0.000908	0.000638	0.001546
		4100	8200	0.000906	0.000623	0.001529
		4200	8400	0.000903	0.00061	0.001513
		4300	8600	0.000901	0.000596	0.001497
		4400	8800	0.000898	0.000584	0.001482
		4500	9000	0.000896	0.000572	0.001468
		4600	9200	0.000894	0.00056	0.001454
		4700	9400	0.000892	0.000549	0.001441
		4800	9600	0.000889	0.000539	0.001428
		4900	**9800**	**0.000887**	**0.000528**	**0.001416**
		5000	10000	0.000885	0.000519	0.001404

C-5 Biaxial Kandil-Miller-Brown Strain Life Equation Solution

BIAXIAL

		Nf	2Nf	C	D	C+D
A	0.003211	1000	2000	0.00135	0.00269	0.00404
		1100	2200	0.001335	0.002462	0.003798
B	3.08875	1200	2400	0.001322	0.002272	0.003594
		1300	2600	0.00131	0.002109	0.003419
		1400	2800	0.001299	0.001969	0.003268
		1500	3000	0.001289	0.001847	0.003136
		1600	3200	0.001279	0.00174	0.003019
		1700	3400	0.001271	0.001645	0.002915
		1800	3600	0.001262	0.00156	0.002822
		1900	3800	0.001255	0.001484	0.002738
		2000	4000	0.001247	0.001415	0.002662
		2100	4200	0.00124	0.001352	0.002593
		2200	4400	0.001234	0.001295	0.002529
		2300	4600	0.001228	0.001243	0.00247
		2400	4800	0.001222	0.001195	0.002416
		2500	5000	0.001216	0.00115	0.002366
		2600	5200	0.001211	0.001109	0.00232
		2700	5400	0.001205	0.001071	0.002277
		2800	5600	0.0012	0.001036	0.002236
		2900	5800	0.001196	0.001003	0.002198
		3000	6000	0.001191	0.000971	0.002162
		3100	6200	0.001187	0.000942	0.002129
		3200	6400	0.001182	0.000915	0.002097
		3300	6600	0.001178	0.000889	0.002067
		3400	6800	0.001174	0.000865	0.002039
		3500	7000	0.00117	0.000842	0.002012
		3600	7200	0.001166	0.00082	0.001987
		3700	7400	0.001163	0.0008	0.001963
		3800	7600	0.001159	0.00078	0.00194
		3900	7800	0.001156	0.000762	0.001918
		4000	8000	0.001153	0.000744	0.001897
		4100	8200	0.001149	0.000727	0.001877
		4200	8400	0.001146	0.000711	0.001857
		4300	8600	0.001143	0.000696	0.001839
		4400	8800	0.00114	0.000681	0.001821
		4500	9000	0.001137	0.000667	0.001804
		4600	9200	0.001134	0.000654	0.001788
		4700	**9400**	**0.001132**	**0.000641**	**0.001772**
		4800	9600	0.001129	0.000628	0.001757
		4900	9800	0.001126	0.000616	0.001743
		5000	10000	0.001124	0.000605	0.001729

APPENDIX D - MSD Analysis

D.1 Specimen Data

8 rivet specimens

	specimen number	aircraft cycles	specimen cycles	total cycles	mean (cycles)	std dev (cycles)	total cycles (log cycles)	mean (log cycles)	std dev (log cycles)
1	5	19127	83067	102194	101534.4	23155.31	5.0094254	4.995559	0.107863
2	6	19127	113564	132691			5.12284147		
3	11	19127	88930	108057			5.03365291		
4	13	19127	47653	66780			4.82464641		
5	20	19127	83094	102221			5.00954013		
6	21	19127	103485	122612			5.08853298		
7	23	19127	89298	108425			5.03512943		
8	25	19127	50168	69295			4.8407019		

6 rivet specimens

	specimen number	aircraft cycles	specimen cycles	total cycles	mean (cycles)	std dev (cycles)	total cycles (log cycles)	mean (log cycles)	std dev (log cycles)
1	12	19127	162973	182100	192036.8	48427.74	5.26030995	5.270731	0.121474
2	17	19127	223780	242907			5.38544003		
3	19	19127	167923	187050			5.27195771		
4	22	19127	209816	228943			5.35972737		
5	24	19127	100057	119184			5.07621796		

D.2 MSD Initiation – 6FCLs (1st 5 Scenarios)

Scenario #	FCL	mean (log cycles)	std dev (log cycles)	Alpha Gaussian random numbers N[0,1]	Log Nij	Nij (cycles)
1	1	4.995559	0.107863	-0.88163	4.900464	78516.6992
	2	4.995559	0.107863	0.687416	5.069706	115881.481
	3	4.995559	0.107863	-1.19793	4.866347	72591.082
	4	4.995559	0.107863	1.928998	5.203627	157682.844
	5	4.995559	0.107863	-0.433795	4.948769	87743.0302
	6	4.995559	0.107863	-1.252875	4.86042	71608.3045
2	1	4.995559	0.107863	-0.921702	4.896141	77740.0114
	2	4.995559	0.107863	0.002158	4.995792	97764.9167
	3	4.995559	0.107863	0.74037	5.075418	117413.869
	4	4.995559	0.107863	-2.946835	4.677705	47038.4407
	5	4.995559	0.107863	0.810876	5.083023	119485.678
	6	4.995559	0.107863	-2.05218576	4.774204	58727.8536
3	1	4.995559	0.107863	0.310665	5.029068	105541.234
	2	4.995559	0.107863	0.475208	5.046816	109938.635
	3	4.995559	0.107863	-0.191423	4.974912	93180.7602
	4	4.995559	0.107863	1.252564	5.130664	133322.717
	5	4.995559	0.107863	0.364153	5.034838	106951.053
	6	4.995559	0.107863	0.421354	5.041008	108479.584
4	1	4.995559	0.107863	-0.61408	4.929322	83905.104
	2	4.995559	0.107863	0.299423	5.027856	105247.292
	3	4.995559	0.107863	2.03384	5.214935	161837.932
	4	4.995559	0.107863	0.587057	5.058881	113031.936
	5	4.995559	0.107863	-0.472942	4.944546	86895.0138
	6	4.995559	0.107863	1.998401	5.211113	160421.309
5	1	4.995559	0.107863	-0.761615	4.913409	80889.5982
	2	4.995559	0.107863	1.131904	5.11765	129390.985
	3	4.995559	0.107863	0.688868	5.069862	115923.231
	4	4.995559	0.107863	0.934566	5.096364	123209.004
	5	4.995559	0.107863	-0.452209	4.946782	87343.1136
	6	4.995559	0.107863	-0.684407	4.921737	82453.9024

D.3 MSD initiation – 14FCLs (1st 2 Scenarios)

| Scenario #	FCL	mean (log cycles)	std dev (log cycles)	Alpha Gaussian random numbers N[0,1]	Log Nij	Nij (cycles)
1	1	5.270731	0.121474	-0.88163	5.163636	143826.432
	2	5.270731	0.121474	0.687416	5.354234	222957.978
	3	5.270731	0.121474	-1.19793	5.125214	131661.748
	4	5.270731	0.121474	1.928998	5.505054	315408.668
	5	5.270731	0.121474	-0.433795	5.218036	162996.373
	6	5.270731	0.121474	-1.252875	5.118539	129656.03
	7	5.270731	0.121474	-0.921702	5.158768	142225.171
	8	5.270731	0.121474	0.002158	5.270993	184109.179
	9	5.270731	0.121474	0.74037	5.360667	226281.125
	10	5.270731	0.121474	-2.946835	4.912767	80770.2901
	11	5.270731	0.121474	0.810876	5.369231	230782.759
	12	5.270731	0.121474	-2.05218576	5.021444	103706.566
	13	5.270731	0.121474	0.310665	5.308469	200682.243
	14	5.270731	0.121474	0.475208	5.328456	210123.295
2	1	5.270731	0.121474	-0.191423	5.247478	174416.185
	2	5.270731	0.121474	1.252564	5.422885	261093.904
	3	5.270731	0.121474	0.364153	5.314966	203703.764
	4	5.270731	0.121474	0.421354	5.321915	206985.388
	5	5.270731	0.121474	-0.61408	5.196136	154989.611
	6	5.270731	0.121474	0.299423	5.307103	200052.908
	7	5.270731	0.121474	2.03384	5.51779	324784.208
	8	5.270731	0.121474	0.587057	5.342043	216793.219
	9	5.270731	0.121474	-0.472942	5.213281	161223.348
	10	5.270731	0.121474	1.998401	5.513485	321584.287
	11	5.270731	0.121474	-0.761615	5.178215	148730.844
	12	5.270731	0.121474	1.131904	5.408228	252438.816
	13	5.270731	0.121474	0.688868	5.354411	223048.445
	14	5.270731	0.121474	0.934566	5.384256	238897.503

D.4 AFGROW PREDICTIONS

D.4.1 Single Corner Crack

Title: single corner crack at hole
Spectrum title: Constant amplitude loading (200MPa, R=0.2)
1030 <--- crack geometry code: Single Corner Crack at Hole

Cycles	C Length	A Length	Beta C	Beta A	Sb. Spectrum	Pass	Life
0	0.138	0.07	0.965	1.914	1	1	0
0	0.138	0.072	1.178	1.914	1	1	0
400	0.150733	0.072	1.153	1.914	5	5	400
700	0.160825	0.072	1.13	1.914	8	8	700
1000	0.171392	0.072	1.108	1.914	11	11	1000
1300	0.182483	0.072	1.089	1.914	14	14	1300
1600	0.19415	0.072	1.07	1.914	17	17	1600
1900	0.206507	0.072	1.053	1.914	20	20	1900
2200	0.219704	0.072	1.037	1.914	23	23	2200
2500	0.233857	0.072	1.022	1.914	26	26	2500
2700	0.244052	0.072	1.008	1.914	28	28	2700
2900	0.254486	0.072	1.008	1.914	30	30	2900
3100	0.265614	0.072	0.995	1.914	32	32	3100
3300	0.277596	0.072	0.984	1.914	34	34	3300
3500	0.289996	0.072	0.984	1.914	36	36	3500
3700	0.303431	0.072	0.973	1.914	38	38	3700
3900	0.3179	0.072	0.963	1.914	40	40	3900
4100	0.333211	0.072	0.963	1.914	42	42	4100
4300	0.34985	0.072	0.954	1.914	44	44	4300
4500	0.367781	0.072	0.949	1.914	46	46	4500
4700	0.38736	0.072	0.944	1.914	48	48	4700
4800	0.398285	0.072	0.941	1.914	49	49	4800
4900	0.410043	0.072	0.941	1.914	50	50	4900
5000	0.423105	0.072	0.938	1.914	51	51	5000
5100	0.43745	0.072	0.938	1.914	52	52	5100
5200	0.453634	0.072	0.937	1.914	53	53	5200
5300	0.471973	0.072	0.937	1.914	54	54	5300
5400	0.493468	0.072	0.94	1.914	55	55	5400
5492	0.518368	0.072	0.944	1.914	55	55	5492
5573	0.547532	0.072	0.95	1.914	56	56	5573
5600	0.561304	0.072	0.95	1.914	57	57	5600
5648	0.589715	0.072	0.964	1.914	57	57	5648

single corner crack at hole (Crack C Length vs. Cycles)
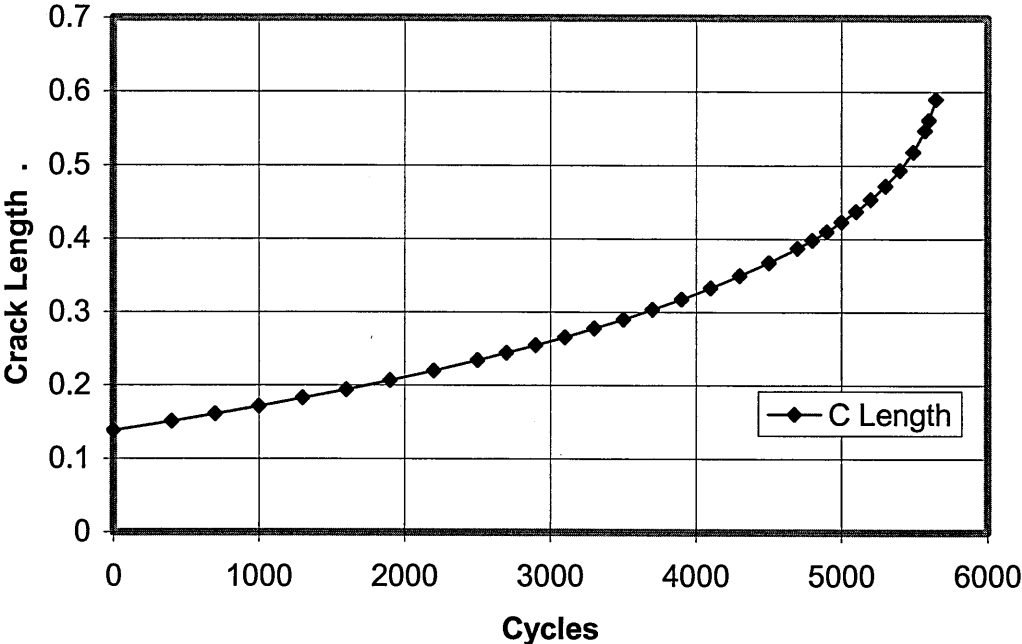
D.4.2 Double Corner Crack

Title: single corner crack at hole
Spectrum title: Constant amplitude loading (200MPa, R=0.2)
1050 <--- crack geometry code: Double Corner Crack at Hole

Cycles	C Length	A Length	Beta C	Beta A	Sb. Spectrum	Pass	Life
0	0.138	0.07	1.133	2.248	1	1	0
0	0.138	0.072	1.365	2.248	1	1	0
200	0.149634	0.072	1.342	2.248	3	3	200
400	0.162505	0.072	1.317	2.248	5	5	400
600	0.176717	0.072	1.298	2.248	7	7	600
800	0.192715	0.072	1.287	2.248	9	9	800
1000	0.211431	0.072	1.278	2.248	11	11	1000
1098	0.222106	0.072	1.271	2.248	11	11	1098
1189	**0.233583**	**0.072**	**1.265**	**2.248**	**12**	**12**	**1189**
1280	0.247085	0.072	1.258	2.248	13	13	1280
1370	0.263121	0.072	1.253	2.248	14	14	1370

double corner crack at hole (Crack C Length vs. Cycles)